DISSERTATION

EXPERIMENTAL AND COMPUTATIONAL COMPARISON OF A LOW HEAT REJECTION ENGINE WITH A CONVENTIONALLY COOLED ENGINE

Submitted by

Joseph G. Beard

Department of Mechanical Engineering

In partial fulfillment of the requirements

for the Degree of Doctor of Philosophy

Colorado State University

Fort Collins, Colorado

Summer 2006

COLORADO STATE UNIVERSITY

June 22, 2006

WE HEREBY RECOMMEND THAT THE DISSERTATION PREPARED UNDER OUR SUPERVISION BY JOSEPH G BEARD ENTITLED EXPERIMENTAL AND COMPUTATIONAL COMPARISON OF A LOW HEAT REJECTION ENGINE WITH A CONVENTIOANLLY COOLED ENGINE, BE ACCEPTED AS FULFILLING IN PART REQUIREMENTS FOR THE DEGREE OF DOCTOR OF PHILOSOPHY.

Committee on Graduate Work

Joseph Beebe

Dwaine Klarstrom

Bryan D. Willson

Advisor – Walajabad S. Sampath

Department Head – Allan T. Kirkpatrick

ABSTRACT OF DISSERTATION

EXPERIMENTAL AND COMPUTATIONAL COMPARISON OF A LOW HEAT REJECTION ENGINE WITH A CONVENTIONALLY COOLED ENGINE

The objective of this dissertation is to determine if, in practice, there are performance gains to be realized from insulating the combustion chamber of a diesel engine and, if so, what degree of insulation is desirable. The effect of partially insulating the combustion chamber of a single cylinder diesel engine is examined. The experimental data collected from running an un-insulated and partially-insulated test engine at various speeds and loads are used to calibrate computer simulations of the test engine. The computer simulation programs, namely Kiva Lite, Wave, and JLAnalyzer, collectively comprise the computational model which was then altered to extend analyses to modifications not attempted experimentally. From the computational model, the optimal exhaust turbine and intake compressor combination for several cylinder insulation levels was determined. The models revealed that there is some performance enhancement to be gained by optimizing engine insulation levels, but that intra-cycle heat transfer limits the efficiency gains to 1% for the Lister-Petter test engine that was modeled. An exact solution to the simplified cylinder heat transfer problem is coupled to an idealized diesel cycle and used to examine the heat transfer mechanisms that limit the efficiency gains as engine insulation is increased.

Joseph Grady Beard
Mechanical Engineering Department
Colorado State University
Fort Collins, CO 80523
Summer 2006

ACKNOWLEDGEMENTS

To my advisor, Walajabad Sampath, I give my sincere thanks for his patience, support, and encouragement.

Special thanks to Dwaine Klarstrom and HAYNES International for providing the HAYNES 230 superalloy used in the Low Heat Rejection Engine modifications. Thanks is also due to Ben Johnson and Federal Mogul Corporation for allowing the use of a picture of their articulated piston, Heather Noel Bean for proofreading, and my wife Tonia for her support and for all those things that spouses of graduate students endure.

DEDICATION

This work is dedicated to Leila Margaret Kantz Beard (October 1940 – August 2001).

TABLE OF CONTENTS

LIST OF FIGURES

NOMENCLATUIRE

Symbols

ABDC	After Bottom Dead Center
ATDC	After Top Dead Center
BBDC	Before Bottom Dead Center
BMEP	Brake Mean Effective Pressure
BTDC	Before Top Dead Center
CO	carbon monoxide
C_P	specific heat at constant pressure
C_V	specific heat at constant volume
EVO	Exhaust Valve Opening
FEA	Finite Element Analysis
FEM	Finite Element Method
FMEP	Friction Mean Effective Pressure
HC	Hydrocarbons
h	enthalpy, kJ/kg; convection coefficient W/m^2 K
ICE	Internal Combustion Engine
IMEP	Indicated Mean Effective Pressure
k	thermal conductivity, W/m K

LHRE	Low Heat Rejection Engine
MEP	Mean Effective Pressure
MW	Molecular weight
$\dot{m}$	mass flow rate, kg/hr or g/s
NO_x	collective term for both nitric oxide (NO) and nitrogen dioxide (NO_2)
Nu	Nusselt number
P	Pressure
Pdv	Pressure times volume change work, J or kJ
Pr	Prandtl number
Q	thermal energy, J
q	specific thermal energy, kJ/kg or J/g
q''	heat flux, W/m^2
R	specific gas constant equals Ru/MW
Re	Reynolds number
Ru	universal gas constant, 8315 J/kmol K
r	compression ratio
r_c	cutoff ration
T	Temperature
TEG	ThermoElectric Generator
u	internal energy, kJ/kg
V	Volume, m^3 or cm^3
v	specific volume, m^3/kg

W	Work, kJ or J; humidity ratio
w	specific work, kJ/kg or J/g
γ	isentropic expansion coefficient, for ideal gases $\gamma = C_P/C_V$
ε	error
η	efficiency
η_{TH}	thermal efficiency
η_V	volumetric efficiency
ν	kinematic viscosity, m^2/s
ρ	density (kg/m^3)
σ	standard deviation of the mean
ϕ	ratio of enthalpy after heat addition to enthalpy before; equivalence ratio
ω	angular velocity, rad/s; uncertainty
$\bar{x}$	overbar indicates mean value; molar based property

Subscripts

a	air
amb	ambient
CI	Compression Ignition
cw	cylinder wall
Diesel	denotes the ideal Diesel cycle
fb	fin base

ft	fin tip
H	High, *e.g.* T_H = high temperature
L	Low; characteristic length
mix	mixture
Otto	denotes the ideal Otto cycle
rev	reversible
TH	Thermal, *e.g.* η_{TH} = thermal efficiency
v	water vapor
1, 2, 3, *etc.*	state 1, state 2, state 3, *et cetra*

CHAPTER 1

INTRODUCTION

1.1 Why a Low Heat Rejection Engine?

Those who work with engines, and many of those who do not, know that increasing the compression ratio, r, of an internal combustion engine increases the engine's performance. The performance increase may manifest as more of the brake horsepower hyped by hot-rod magazines, more of the pulling torque touted in the tractor-pull monthlies, or perhaps more megawatt-hours per ton of coal. But whatever the performance metrics used, and however a particular heat engine is designed and tuned, there is a hard and immutable limit on the amount of fuel energy available for conversion to work.

The fraction of fuel energy converted to work is known as the thermal efficiency and is, for a real heat engine, always less than that of an ideal engine. An ideal engine has neither heat loss nor gain through engine components, nor friction in the moving parts and flowing fluids. A compression ignition engine's thermal efficiency, $\eta_{TH,\,CI}$, is always less than the thermal efficiency of the ideal Diesel cycle, $\eta_{TH,\,Diesel}$. An engine person's expression for this is $\eta_{TH,\,CI} < \eta_{TH,\,Diesel}$ and

$$\eta_{TH,\,Diesel} = 1 - \left(\frac{1}{r}\right)^{\gamma-1}\left[\frac{r_c^{\gamma} - 1}{\gamma(r_c - 1)}\right] \tag{1.1}$$

While the thermodynamicist would say, "$\eta_{TH,\,CI} < \eta_{TH,\,Diesel} \leq \eta_{TH,\,rev}$,

$$\eta_{TH,\,rev} = 1 - \frac{T_L}{T_H}, \tag{1.2}$$

and

$$\eta_{TH,\,Diesel} = 1 - \frac{T_L}{T_H}\cdot\phi\left[\frac{\phi^{\gamma} - 1}{\gamma(\phi - 1)}\right]," \tag{1.3}$$

where ϕ is the ratio of the enthalpy after heat addition to the enthalpy before, r_c is the cutoff ratio, $\eta_{TH,\,rev}$ is the reversible or Carnot efficiency, and γ is the isentropic expansion coefficient which, for an ideal gas, is the ratio of specific heat at constant pressure to the specific heat at constant volume (*id est*, $\gamma = C_P/C_V$)[1].

Equation 1.3 allows for direct evaluation of the effect of raising T_H, the temperature of the heat source in the ideal gas cycle. For example, fixing the heat sink temperature, T_L, at a typical ambient value of 300 K, holding ϕ and γ at 1.4, and raising T_H by 20%, say from 800 K to 960 K, has the effect of raising the Carnot efficiency by 10% (from 0.625 to 0.688) and $\eta_{TH,\,Diesel}$ by 22% (from 0.436 to 0.530) (see figure 1). In other words, raising the highest temperature in a cycle similarly raises the upper limit on efficiency. In practice, however, T_H is kept significantly below obtainable levels. The reason for this was stated well by thermodynamicist Yunus Çengel:

[1] Derivations of equations 1.1 and 1.3 are to be found in Appendix A: Thermal Efficiency of the Diesel Cycle.

"The source and sink temperatures that can be used in practice are not without limits. The highest temperature in the cycle is limited by the maximum temperature that the components of the heat engine, such as the piston or the turbine blades, can withstand. The lowest temperature is limited by the temperature of the cooling medium utilized in the cycle such as a lake, a river, or the atmospheric air." [Çengel and Boles, 1989]

In a practical engine, the degree to which an increase in the efficiency limit due to raising T_H can be exploited depends on the artfulness of the engine's designer and skill of its builder.

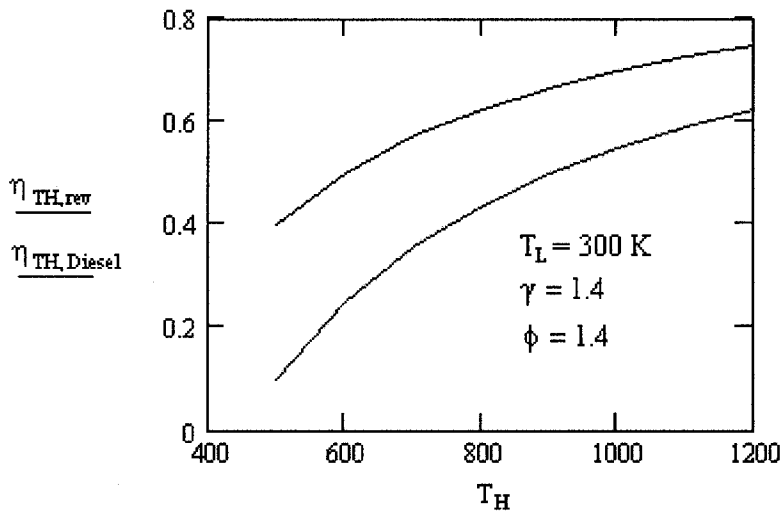

Figure 1.1 – Thermal Efficiency vs. T_H

Since the invention of ICEs (internal combustion engines), there has been much effort to improve their performance. An amount of this effort has gone toward increasing operating temperatures as, ultimately, the efficiency of any heat engine is limited by the maximum temperature achieved. Materials which can withstand the stress and environment of reciprocating internal combustion engines at elevated temperatures may

allow designers to reduce or eliminate the cooling system. The energy not deliberately removed and discarded from the working fluid, or combustion gasses, remains available for work production. Engines that are insulated or use advanced materials to reduce the heat rejected through their cooling system are called LHREs (Low Heat Rejection Engines).

In an LHRE, the energy not lost through the cooling system typically manifests as higher exhaust gas enthalpy. Use of an exhaust energy recovery system, such as a turbocompounder, to exploit the greater exhaust enthalpy can increase engine efficiency beyond the range of conventionally cooled engines. In addition to enhanced efficiency, higher combustion temperatures can reduce emissions of soot, hydrocarbons, and carbon monoxide. Reduction or elimination of the cooling system can reduce an engine's size, weight, and expense. Engine reliability can be enhanced as cooling systems contribute significantly to maintenance costs and downtime.

Low heat rejection engines are not currently in widespread use because of problems with lubrication, emissions, and materials. However, at Colorado State University, isolation of the high temperature zone has shown promise. As combustion temperatures increase, so does formation of nitric oxide and nitrogen dioxide – collectively called NO_x. Some applications of LHREs may require catalysts to reduce NO_x emissions. Ceramics are an attractive materials choice for LHREs because of their very high working temperature together with low conductivity and low density. Unfortunately, ceramic coatings fatigue and spall while monolithic ceramic components fare little better under the cyclic thermal stress of reciprocating IC engines.

An alternative to ceramics is the use of superalloys. Superalloys withstand greater temperatures than conventional engine materials, have lower conductivities than conventional engine materials, have much greater fracture toughness than ceramics, and are significantly more tolerant to flaws than ceramics. On the down side, superalloys are dense, have higher conductivities than ceramics, and can not withstand the extreme temperatures afforded by some ceramics. Colorado State University has developed a piston with a superalloy top fastened to an aluminum base. The piston has internal ceramic insulation. This composite piston has been tested in a single cylinder engine.

1.2 Motivation

There are several reasons to develop LHREs. Cooling systems can account for up to 15% of fuel consumption [Buckley, 1986]. Reducing the cooling requirements reduces the parasitic work loss. Reduction or elimination of the cooling system can reduce size, weight, and maintenance requirements as an engine's cooling system accounts for up to 40% of engine weight and volume and is responsible for up to half of all engine failures [Bryzik, 1983]. LHREs can use, and may require, low cetane fuels in diesel applications [Sun, 1993]. About a third of the fuel's chemical energy is converted to work with the balance being rejected to the exhaust and cooling system in approximately equal amounts [Amann, 1990]. The effects on emissions of raised combustion temperatures are lower hydrocarbon, lower soot, lower CO, and higher NO_x [Kobori, 1992].

While surveying the literature for this research, two promising areas for applying LHREs were identified: distributed electrical power generation and military vehicle power.

1.2.1 Distributed Power Generation

The DOE (Department of Energy) maintains that a balanced and deregulated power industry requires efficient, high performance, cost effective, and clean burning natural gas engines to capture the emerging distributed generation market. To that end, the DOE's Office of Power Technologies recently accepted applications for funding in the area of advanced natural gas reciprocating engines. This funding was made possible under the DER program (Distributed Energy Resources) established to develop distributed power use in industrial, commercial, institutional, and residential applications. The goal of the DER program is to meet 20% of new electrical capacity additions with distributed energy technologies. The DOE has identified five features of advanced natural gas engines: fuel to electric energy conversion efficiency of 50% based on the lower heating value of natural gas, emissions of 0.1g/hp-hr or less, multi-fuel capacity, installed energy generation costs 10% less than current state-of-the-art engine systems, and reliability and maintainability equivalent to state-of-the-art engine systems [DOE solicitation DE-SC02-00CH11029].

Low heat rejection engines can satisfy all five of the DOE's criteria. The efficiency gains afforded by extraction of energy which is conventionally discarded to protect lower operating temperature components can help achieve the efficiency goal. As some sort of

exhaust energy recovery scheme, *e. g.* turbocompounding, will most likely be required to meet the efficiency goal on any engine, the necessary inclusion of such on an LHRE does not detract from an LHRE's advantages. The higher combustion temperatures afforded by today's superalloys can reduce emissions of hydrocarbons and CO. The elimination or reduction of the cooling system can have a significant effect on initial cost, as well as maintenance costs and durability.

1.2.2 Military Vehicle Power

The United States Army TACOM (Tank and Automobile Command) has been pursuing LHRE applications for some time [Badgley *et. al.*, 1990; Bryzik and Kamo 1983; Freese, *et al.* 1993; Kamo and Bryzik, 1982; Kamo and Bryzik 1985] . Elimination of the cooling system can make vehicles more compact, enhancing maneuverability. Battlefield survivability due to elimination of vulnerable cooling systems, readiness due to reduced maintenance, and an easing of logistical constraints due to multi-fuel capability combine to give the LHRE powered units a formidable tactical advantage.

1.3 Scope of Work

The LHRE question contains three parts. Is there benefit, performance or otherwise, to be gained by implementing a low heat rejection strategy? If so, then does the benefit of insulating the combustion chamber outweigh the cost of overcoming the attendant obstacles? Lastly, what degree of insulation is desirable, or where is the point of diminishing returns? The first and third parts of this question are explored in this

work. The second part of the question, "When does the benefit outweigh the cost," is a matter of application. For example, turbocharging a diesel engine has some benefits, yet not all diesel engines are turbocharged. The tasks completed to explore the LHRE question are:

1) Collect data from a naturally aspirated test engine in both conventionally cooled and partially insulated configurations.
2) Compare the performance of the two configurations of the test engine with various metrics.
3) Use the data from the test engine to calibrate computer simulations of the test engine
4) Use the calibrated simulations to investigate the effects of exhaust energy scavenging and of different insulation levels.

1.4 Structure and Organization of Dissertation

Of course, the fundamental structure of this work may be gleaned from the table of contents. This section is included to signpost the way to specific tasks *vis á vis* section 1.3: Scope of Work.

An introduction to LHRE's and motivation for this work are presented in the first chapter. In chapter 2, the literature review, the range of previous work that has had a direct impact on this work is discussed. The main body of this work is contained in chapters 3, 4, 5, and 6 which are dedicated to tasks 1, 2, 3, and 4, respectively, as outlined in the Scope of Work.

Chapter 3 describes the nature of the test engine and the instrumentation used in the experimental portion of this work. Since an engine dynamometer was assembled *in situ*, some verbiage is expended explaining its idiosyncrasies. Also presented is the mass flow meter calibration curve.

Chapter 4, Experimental Results, follows naturally from Chapter 3. For the test engine in the two configurations (conventionally cooled and partially insulated) the torque, η_V, power, exhaust enthalpy, and other properties of interest are presented. Some discussion of the experimental results is also given, for example: piston mass effect on friction torque.

Chapter 5 starts with an introduction to the computer models/simulations used. Much emphasis is given to the treatment of raw temperature data from the experiment. With the calibration complete, the models were run for various insulation levels and the optimal turbine/compressor combination was determined for each. These results are presented in Chapter 6.

In chapter 7 an exact solution to the simplified engine heat transfer problem is coupled to an idealized diesel cycle. This model is then used to explore the heat transfer consequences of insulating an engine. The effects of different material choices are exposed, as is the nature of the in-cylinder heat transfer.

Lastly, Chapter 8 summarizes the results and suggests the course required to bring the promise of LHRE's to fruition.

CHAPTER 2

LITERATURE REVIEW

A review of pertinent literature is presented in this chapter. The first two sections address the available materials for LHREs along with some of the attendant pros and cons. Next is a discussion of lubrication and the problems associated with providing it on or near components with elevated temperatures. Last is a review of LHREs. The review of the various engines is presented mostly without comment as the results tend to speak for themselves. The common themes that emerge are modest success with insulating the engine and a need for exhaust energy recovery.

2.1 Materials, Ceramics

The use of advanced materials with high working temperature and low conductivity in ICEs began in the 1940's with the application of ceramic barrier coatings on engine exhaust valves. By 1960, barrier coatings found use in X-15 rocket nozzles & turbine combustors [Stearns, 1987]. Current methods to raise the operating temperature of reciprocating engines include ceramic coatings, ceramic inserts, monolithic structural ceramic, and superalloy components.

Ceramic coatings are usually applied with plasma spray. The coating thickness must be carefully maintained (< +/- 0.04mm) to avoid spalling due to uneven heating

[Winkler, 1992]. Zirconium oxide (ZO_2) is attractive due to its high melting point of 2400 °C coupled with a low conductivity of 1.3 W/mK. Y_2O_3 (yttrium oxide), CaO (calcium oxide), or MgO (magnesium oxide) are often used to stabilize ZrO_2, the mixture being called PSZ (partially stabilized zirconia). Zirconia coatings allow oxidation of the base metal so that an iron, nickel, or cobalt alloy bond must be used [Kvernes, 1986]. The bond layer must overcome the differential expansion between ceramic and substrate as well as inertial and mechanical stresses. Cyclic thermal stresses can cause separation in ceramic coatings [Heinrich, 1986].

The use of ceramic inserts and wholly ceramic components obviates the separation failures experienced with coatings, and while the inserts must be securely fixed in place, the metal ceramic bond is under somewhat relaxed performance requirements. British Leyland explored silicon nitride, LAS (lithium aluminum silicate), cordierite, and PSZ for suitability as a monolithic piston crown. The ceramic was attached with an interference fit on the aluminum piston base with an air gap beneath the ceramic for added insulation. Temperatures exceeded 800 °C [Parker, 1990].

Comparing results from other researchers, Rakopoulos and Mavropoulos found that a bulky ceramic cap (instead of a ceramic coating) increases heat transfer through the upper piston skirt due to heat capacitance of ceramic, though overall heat flux reduction is still realized. In accord with other published results, reduction of heat rejection is accomplished with greater effectiveness at part load. A 0.15 mm air gap in the perimeter of the piston base reduces heat flux by greater than 30%. The elevated combustion

surface temperatures cause higher heat flux to the cylinder walls over some of the cycle, but the mean flux is always reduced [Rakopoulos and Mavropoulos, 1998].

Ceramics are flaw intolerant and even small flaws (10 μm) can drastically reduce strength. The stabilizers in PSZ react with combustion products and the zirconia reverts from tetragonal and cubic to monoclinic structure [Kvernes, 1986]. While initially more wear resistant than iron, zirconia coated cam lobes and followers showed accelerated wear after only 500 hours of service [Heinrich, *et al.*, 1986].

Intermetallic compounds are metals with ordered atomic structure. Nickel aluminide (NiAl) in near equi-atomic beta form has a melting temperature of 2980 °F (1638 °C), but lacks ductility and strength. Addition of tantalum increases its creep strength at 2000 °F (1093 °C) to that of superalloys. Room temp brittleness is also a problem [Stephens, 1987].

2.2 Materials, Superalloys

Superalloys have higher conductivities than ceramics, though usually lower than iron, steel, and aluminum, and are usually denser than both ceramics and conventional metals. Though their maximum working temperature is less than ceramics, they are tougher and more easily machined. Fracture toughness for most metals falls between 40 and 100 $MPa(m)^{0.5}$, while for ceramics it is usually less than 10 $MPa(m)^{0.5}$. The fracture toughness for superalloys is typically between 80 and 110 $MPa(m)^{0.5}$. While recent approaches such as incorporation of fibers have increased the toughness and reliability of ceramics, cost of fabrication, cost of machining, and manufacturing yield continue to pose

significant problems for the application of ceramic components in LHREs. The LHRE design developed in our laboratory uses the HAYNES 230 superalloy. HAYNES 230 has excellent fatigue, oxidation resistance, and creep behavior which made it the first candidate to replace older superalloys (*e.g.* N-155) in the manufacture of gas turbine stators [Klova and Subaru, 1993].

2.3 Lubrication

Most of the approaches to LHRE designs necessitate the use of high temperature lubricants. A notable exception is the engine developed at CSU, mentioned above, which allows conventional lubrication through separation of the high temperature combustion zone and the lower temperature lubrication zone [Zhou, 1995]. Since current conventional oils have maximum operating temperatures of 350 °F (177 °C), an LHRE approach which does not isolate the high temperature combustion zone from the lubricating zone requires an exceptional lubricant. Even synthetic oils, at much greater cost, can not withstand operating temperatures much greater than 450 °F (232 °C) [Pool, 1989].

The best synthetic lubricants are diesters and polyol esters. These are limited to prolonged temperatures below 450 °F (232 °C). Fluorocarbon based lubricants may possibly work up to 650 °F (343 °C). Solid lubricants typically either work poorly at low temperatures, or decompose at higher temperatures. Silver films, either fluoride composite fusion bonded or plasma sprayed, are oxidatively stable to 1762 °F (961 °C), but have low load capacity at high temperatures [Sliney, *et al.*, 1987].

Lubricants for ceramics must be chosen with care as different oil and ceramic combinations allow ceramic-on-ceramic seizing at different loads. Without lubrication all ceramic-on-ceramic sliding parts seize at low load [Shimauchi, *et al.*, 1984]. Ceramics are chemically active under friction wear. For example, zirconia suffers tribochemical attack by hydrocarbons and, while HCs reduce the coefficient of friction from 0.7 to as low as 0.1, the wear rate is increased by an order of magnitude [Bartz 1994].

2.4 Engines

There are many studies of LHREs, both in the laboratory and in the field. The breadth of research, from the early 1980's to present, featuring LHREs or LHRE simulations is summarized here. In 1986 Robert Thring electrically heated the cylinder liner of a single cylinder diesel to simulate an insulated engine and found that the efficiency decreased when naturally aspirated, but increased with turbocharging. Emissions of CO and HC were halved while NO_x rose 15% [Thring, 1986].

In 1997 an experimental insulated single cylinder diesel engine using overexpansion was constructed. This application of the Miller Cycle (defined by an expansion ratio greater than the compression ratio) used an expansion volume to compression volume ratio of 1.5. This was achieved by closing the intake valve at 80 degrees after bottom dead center. Over-expansion partially offset the exhaust temperature rise caused by the insulation, and the decrease in intake air volume caused an increase in smoke at full load [Nazar, *et al.*1997]

Under DOE sponsorship of coal fueled diesel research, GE successfully tested CWS (coal water slurry) injection and built 2 locomotives that utilized it. These locomotive designs are economically justified at oil prices greater than $0.81 per gallon. Optimized combustion efficiency reached 99.5%. For emissions to equal that of diesel, SO_2 would need to be reduced by 50% and particulates by 90%, while NO_x was already half that of a conventional diesel locomotive. Copper oxide (CuO) sorbent on alumina particles coupled with ammonia injection downstream of the turbocharger greatly reduced SO_2 and NO_x simultaneously. A filter downstream collected the sorbent for regeneration. This removed 99% of particulates, 90% of SO_2, and 85% of NO_x [GE Transportation Systems, 1994].

TACOM (Tank and Automobile Command) has built several NT series experimental LHREs. The NT-250 features a PSZ coated cylinder head and piston. Compared to the non-ceramic coated engine, fuel consumption was reduced 10% with an increase in thermal efficiency from 42% to 48% [Badgley, *et al.*, 1990; Zucchetto, *et al.*, 1988; Kamo and Bryzik, 1985, 1982; Bryzik and Kamo, 1983]. A naturally aspirated single cylinder diesel with Nimonic alloy air-gapped piston and PSZ coated valves, head, and liner lost 11% thermal efficiency, though it gained 2.5% when only the liner was insulated [Arunachalam, *et al.*, 1990]. A zirconia insulated truck engine exhibited improved fuel consumption [Parker, 1990]. Thermal barrier coatings on the pistons and cylinder heads of buses gave a 20% increase in engine life and a 20% reduction in maintenance costs [Winkler, *et al.*, 1992]. Thomas Morel and Syed Wahiduzzaman coated the pistons, cylinder head, and valves with PSZ and reported no degradation of the

combustion process. A 2mm ceramic coating on a piston reduced heat loss through the piston by 12 to 30% [Prasad, *et al.* 1989].

Jabez Dhinagar investigated a low compression ratio, spark assisted LHRE fueled by ethanol . A single cylinder, water cooled diesel at compression ratios of 16.5, 12.5, and 10.5 with spark assisted ignition in the lower two compression ratios was tested in both an LHRE and a conventional configuration. The LHRE configuration used a ceramic PSZ coated cylinder head and an iron piston with a Nimonic crown over 0.5mm PSZ. The engine was run at 1500 rpm with variable load while the oil and water temperatures were maintained at 60 °C and 70 °C respectively. Smoke under full load decreased from 6 to 4.5 Bosch# when the LHR components were used. Brake thermal efficiency was up 3.5% even though volumetric efficiency was down by 7%. Emissions of HC went down by 150ppm, CO down 0.2% by volume, and exhaust temperature rose from 400 °C to 500 °C [Dhinagar, *et al.*, 1993, 1992].

Volkswagen used Al_2TiO_5 (aluminum titanate) and ZrO_2 to partially insulate a diesel engine. Fuel consumption increased slightly, CO and HC emissions remained unchanged, and NO_x increased [Heinrich, *et al.*, 1986]. Mazda used an all ceramic swirl chamber of Si_3N_4 (silicon nitride) with an air gap to reduce the soluble organic fraction in emissions while maintaining NO_x at the unaltered engine's level through EGR (exhaust gas recirculation) [Nakatani, *et al.*, 1987].

Fused Si_3N_4 valves, piston, cylinder liner, and head liner were used in the experimental diesel engine developed by the Cawamura Corporation. Their engine

exhibits the lower particulate, higher NO_x, and increased exhaust enthalpy that typifies LHRE performance [Kobori, *et al.*, 1992].

A four cylinder diesel with Si_3N_4 piston caps, chamber liners, valves, cylinder liners, rings, rocker arms, port & manifold liner survived a 1000 hour run. Compared to the uninsulated engine, air intake was reduced by about 10% due to heating on intake. NOx and soot increased. Combustion was degraded due to short ignition delay for the fuel at elevated temperatures as well as poor fuel-air mixing due to the viscosity increase of air at the higher temperatures. Reduction of ignition delay prolongs combustion periods and leads to soot formation. At 775K and 5MPa, a fuel spray that ignites 1.7ms after injection progresses smoothly without soot. At 1021K and 5MPa, ignition time was shorter and soot formed. The centrally located precombustion chamber improved smoke emission and NOx production [Kawamura, *et al.*, 1996]. This engine design ultimately proved unreliable as the ceramic parts failed frequently. Hideo Kawamura has recently switched his research efforts from ceramic engines to engines made of heat resistant metals [Kawamura and Mitsuru, 2003].

The combustion characteristics of LHREs were investigated by Sun, *et al.* Two four-stroke, single cylinder, DI, turbocharged B1135 diesels were used. One was left water cooled and the other was insulated with ceramics. The insulated engine used PSZ on the heads, liners, and valves and heat pressed silicon nitride on the piston. The LHRE and the control engine operated with identical injection and valve timing. Intake air quantity was equalized by boosting pressure in the LHRE. Volumetric efficiency dropped from 0.91 in the control to 0.85 in the LHRE. The LHRE also exhibited reduced ignition

delay but with greatly increased combustion duration due to stifling of fuel-air mixing by the increased gas viscosity at higher temperatures. Two approaches were used to address the LHRE's degraded combustion. In one approach, a diesel-gasoline mixture was used to extend the ignition delay, thereby promoting premixed combustion. The other approach was to increase the injection rate so that heat release would over during the same crank angle as in the control engine. A 25% gasoline to 75% #0 diesel was found to be the best mix. Ignition delay was 1.22ms (.89ms for straight #0 diesel, and 1.33ms for the control engine). Increasing injection pressure slightly decreases ignition delay, but also decreases combustion duration. This corroborates Kobori 1992, who stresses the importance of enhancing mixing [Sun, *et al.* 1993].

A five horsepower diesel with head and valves PSZ coated and the cylinder liner air gap insulated was used to test three different piston assemblies. An aluminum crown on an aluminum piston and a superalloy crown on an aluminum piston both gave a decrease in brake thermal efficiency while a superalloy crown on an iron piston provided a 6.5% increase in efficiency. All three variations gave a 50 °C exhaust temperature rise and 20% cooling load reduction. Also, 2mm air gaps were found to be of superior insulatory quality as compared to 1mm PSZ [Krishnamoorthy, 1980].

Adiabatic Incorporated used a titanium alloy piston and ceramic coated valves and gas ports in an LHRE. From the uninsulated, conventionally cooled engine, cooling load was reduced by 52%. A polyester lubricant was required [Woods, *et al.*, 1992].

CSU altered a single cylinder gasoline engine with a piston top constructed of HAYNES 230. The cylinder head was ceramic coated and a ceramic insert was used for

the upper cylinder liner. This engine had lower fuel consumption at low loads, and lower fuel consumption at high loads than the unaltered engine. Emission of hydrocarbons and CO decreased. NO_x measurements were not taken [Zhou, 1995]. The salient feature of this engine was the separation of the high temperature combustion zone from the ring lubrication zone with a tall piston top. CSU similarly altered a single cylinder diesel for endurance testing of a HAYNES 230 piston with internal ceramic insulation. The engine was run at fast idle for 1001 hours. The piston working temperature was determined to be 760 °C by analyzing the secondary carbide precipitates. After the endurance run, there was no severe wear, no change in grain size of the Hayes 230, no micro cracks or erosion, and no significant chemical reaction [Elshindidy, 1996].

At the Tokyo Institute of Technology Katsunori Hanamura and Satoshi Nishio have developed a super-adiabatic engine and claim a thermal efficiency of 57.5%. Their engine is not a diesel, but a Sterling cycle device with internal heat regenerator. They coined the phrase *super-adiabatic* to indicate that the peak flame temperature is greater than the theoretical adiabatic flame temperature [when reactants start at the reference state and the $q_{regenerator}$ is not considered]. Of interest is the very lean flammability limit that they have achieved of 1.58 vol.% methane in air made possible by the high combustion temperatures [Hanamura & Nishio, 2003].

Shuhn-Shyurng Hou of Kun Shan University, Taiwan has reported on the effects of heat transfer on the indicated thermal efficiency of an air standard Dual cycle. The Dual cycle is an idealized model of the compression-ignition (CI) engine wherein a fraction of heat addition occurs at constant volume and the balance at constant pressure.

Compared to the ideal Diesel cycle, the Dual cycle more closely approximates the heat release profile of modern CI engines. Dr. Hou concludes that the maximum work output and the corresponding efficiency decrease as cylinder heat loss increases. That is, higher heat transfer to the combustion chamber walls lowers the peak temperature and pressure, thereby reducing the work per cycle. Also, work and thermal efficiency decrease as the intake temperature increases [Hou, 2004].

C.D. Rakopoulos and E.G. Giakoumis of the National Technical University of Athens used their in-house developed engine simulation software to evaluate the effect that changes in cylinder wall temperature profiles have on engine performance. They found that a low heat rejection engine strategy leads to a significant decrease in the in-cylinder irreversibilities, thus increasing the potential for work recovery from the exhaust stream [Rakopoulos and Giakoumis, 2005].

The group of engine researchers at Madras Institute of Technology have also puzzled over the LHRE question. They developed a combustion simulation based on the Whitehouse-Way model [Whitehouse & Way, 1971]. With this model they determined that the rate of heat release and cumulative heat release are higher in an insulated engine than in a conventionally cooled engine. However, they also found that performance parameters such as cylinder pressure, work done, and thermal efficiency are higher for conventionally cooled engines than for Low Heat Rejection Engines. While the LHRE has higher charge temperature and greater heat release, the increased heat release is not converted to work but manifests as higher exhaust temperature. They recommend using a turbine to convert some of the exhaust energy to work [Tamilporai *et al.* 2003].

Imdat Taymaz experimented with a Ford six cylinder, direct injected, inter-cooled, turbocharged diesel engine [Taymaz, February 2006]. The engine was run both in stock configuration and then with thermal barrier coated parts (the cylinder head and valves were coated with 0.35 mm of $CaZrO_3$, the pistons were coated with 0.35 mm of $MgZrO_3$) at full rated load and at a fifth, a half, and four fifths of the rated load across the engines rated speed range. Taymaz found that reducing heat rejection mostly resulted in an increase in exhaust energy: from a 12% increase at low load to 21% at high load. Further, he found that thermal efficiency is not improved to the same extent that heat rejection is reduced; and that there is decrease in the volumetric efficiency that may be offset by intake pressure boost – recurrent themes all. An observation that Imdat Taymaz makes with regard to engine design echoes the experimental results of the present work. He writes:

> *"The injection system for the standard engine has been optimised for the air charge and the combustion chamber geometry. This optimisation is no longer maintained at the higher operating temperature of the LHRE configuration, especially at high load. As a result, there is a likely to be a loss in the efficiency in converting chemical to thermal energy."*

Adnan Parlak, (January, 2005) insulated a Ricardo E6-MS/128/76 Diesel engine with thermal barrier coatings of $MgO–ZrO_2$ on the cylinder head, valves, and pistons [Parlak, January 2005]. The engine was supercharged with an external compressor such that the ratio of exhaust pressure to intake pressure was held constant. Parlak found that the optimal injection ti+ming in the LHR diesel engine was at 4° CA retardation from the stock engine's optimal injection timing of 38° CA. The thermal efficiency of the LHR Diesel engine was 2% higher than that of the stock diesel.

CHAPTER 3

EXPERIMENTAL SETUP

Earlier work on the Lister-Petter test engine [Elshindidy, 1996] was conducted at the Engineering Research Center (ERC), a 10,220 m^2 (110,000 ft^2) research facility located three and one-quarter miles west north west of the CSU main campus. This is also where the current work was done, though the mugient call of the Lister-Petter AA1 diesel and its sometimes-noxious exhaust relegated it to an outdoor shed to be run only after hours or on weekends and holidays. The diesel engine was put under load by coupling it to an ad hoc dynamometer via a synchronous gear belt. Combustion air flow was measured by an altered Ford automotive air-mass-flow meter. Fuel consumption was measured with a Waukesha gravimetric fuel stand. Temperatures were measured with type k thermocouples read on an Omega HH-21 handheld thermometer with a range of -200 °C to 1372 °C, +/- 0.2 °C (-328 to 2500 °F). The test engine, dynamometer, flow meter, and fuel stand are discussed further in this section.

3.1 The Test Engine

The test engine is a 1968 Lister-Petter AA1 single cylinder diesel engine, serial number 16880. The engine, in original form, with a bore of 6.985 cm (2.75") and a stroke of 5.715 cm (2.25"), has a displacement of 219 cm^3 (13.4 in^3). The compression

ratio is 17:1, which gives a clearance volume of 13.7 cm^3 (0.84 in^3). The connecting rod is 8.6 cm (3.4") long, center to center. The intake valve, 2.81 cm (1.105") in diameter, opens at 16° BTDC and closes at 36° ABDC. The exhaust valve, 3.12 cm (1.230") in diameter, opens at 44° BBDC and closes at 8° ATDC. Both valves have a lift of 0.69 cm (0.270"). Fuel injection begins at 24° BTDC with a pressure of from 162 to 183 bars. The maximum rated firing pressure is 59.6 bars. The rated torque curve is flat at 7.1 Nm (5.2 ft lbf) until 3600 rpm (the maximum rated speed) where it falls to 6.9 Nm (5.1 ft lbf). The engine has an aluminum head, an aluminum piston, and a steel cylinder.

To partially insulate the combustion chamber, a superalloy piston extension with ceramic insulation was designed and fitted by Mohamed Elshindidy in 1995. The piston extension is 1.04 cm (0.410") thick, so a superalloy cylinder extension of equal thickness is placed between the original cylinder and aluminum head. So that the effect of the superalloy components on engine performance could be better ascertained, a geometrically identical piston and cylinder extension were made of aluminum. Figure 3.1 shows three pistons: the piston with superalloy extension, the piston with aluminum extension, and an unaltered stock piston. Figure 3.2 is the FEM model of the superalloy piston section used for thermal analysis. The internal structure of the superalloy piston extension, cut at the centerline and just below the oil control ring groove, and absent the center one inch diameter bolt, is shown.

The 10 cm^3 (0.61 in^3) combustion chamber, shown in figure 3.3, is approximately 2 cm (0.8") in diameter and 2.3 cm (0.9") deep. The combustion chamber has an

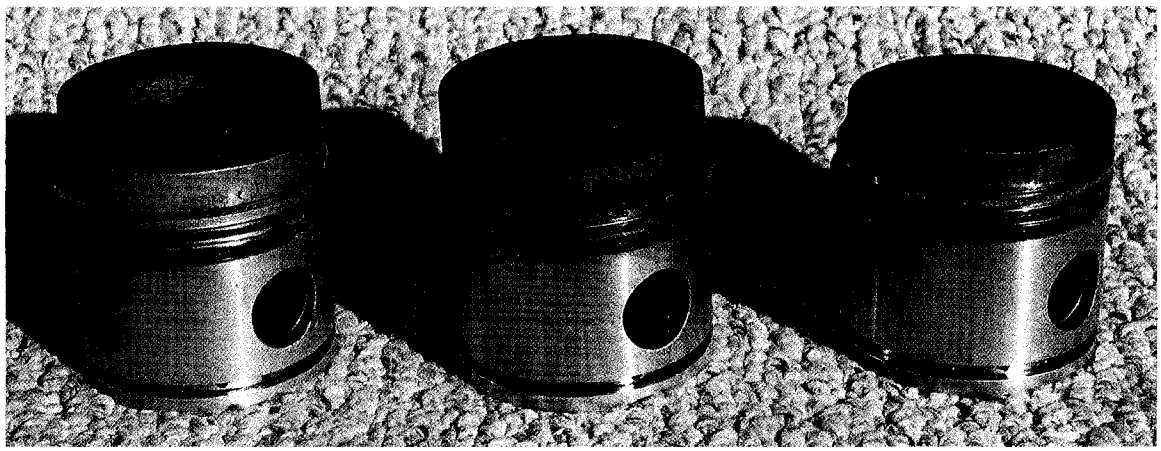

From left to right: pistons w/superalloy extension, w/aluminum extension, stock piston

Figure 3.1 – Pistons for the Lister Petter Engine.

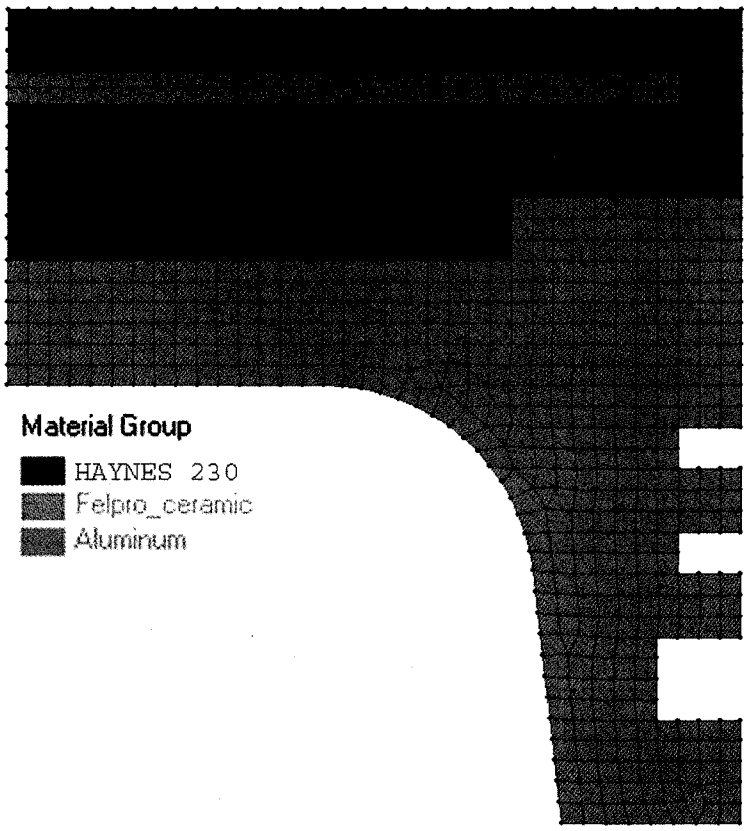

Figure 3.2 – Piston Material Layout for FEM

adjoining 1.5 cm^3 air cell opposite the fuel injector (in figure 3.3 the injector, not visible, is at the top pointing straight down). The balance of the 13.7 cm^3 (0.84 in^3) clearance volume is the bumping clearance space piston top and fire deck

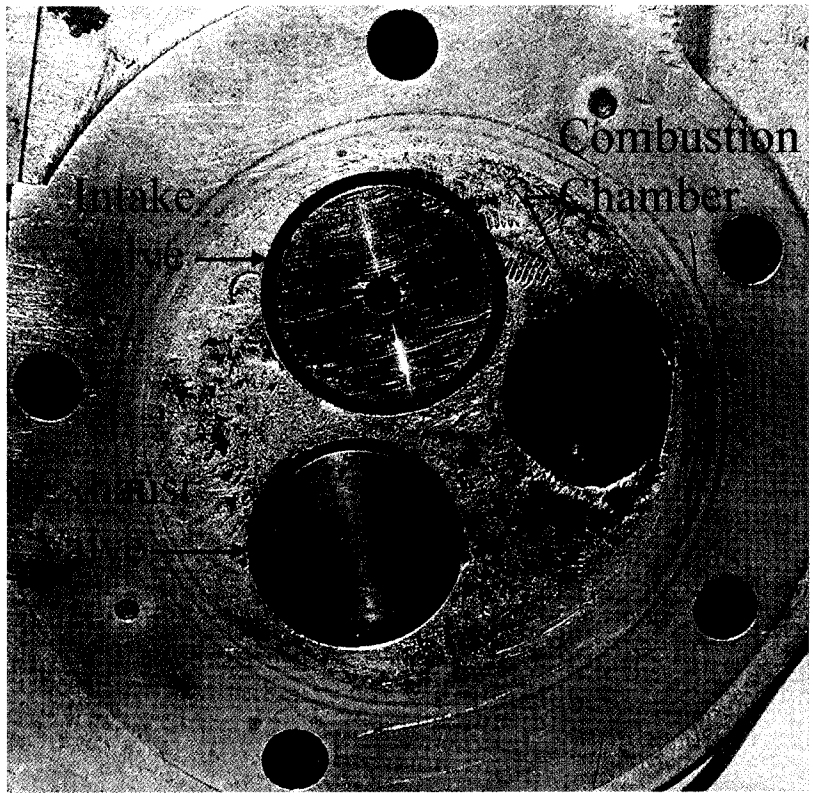

Figure 3.3 – Lister-Petter AA1 Cylinder Head

The previous work on this engine proved the durability of the superalloy piston extension. In that work, the compression ratio was maintained at 17:1 by replacing the air cell with a solid dummy air cell. This compensated for the 0.98 cm^3 (0.06 in^3) volume between the cylinder extension and cylinder wall. In the present work, the air cell was initially left in place resulting in a compression ratio of 15.9:1. However, when the

engine ran poorly, the dummy air cell was returned to service. In theory, the use of a dummy air-cell fundamentally alters the combustion dynamics from the engine's design state of tune. In actuality, under experimental conditions, the air-cell quickly fouls and ceases to perform as intended. The new air-cell's 1.65 mm (0.065") diameter throat became completely occluded by a 5 mm (0.2") long plug of carbon after only a few hours[2] (see figure 3.4). If the air cell had been left in place, then to what extent, or even whether or not, the air-cell participated in combustion would have remained an unanswered question. Since the air-cell no longer functioned reliably as designed, its replacement with the dummy air-cell mitigated variations in combustion dynamics between tests.

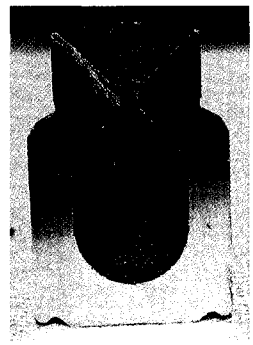

Figure 3.4 Air Cell

3.2 Dynamometer

Budget constraints precluded the purchase of a commercially produced engine test bed, or even a dynamometer. Once it was determined that none of the various laboratories at CSU had a suitable dynamometer for loan, the decision was made to design and assemble one. A three-phase induction motor working against the electric power grid to absorb the torque developed by the diesel engine presents the most tractable dynamometer solution for the budget conscious engineering student.

The windings of a three-phase machine are physically located 120° apart, usually on a stationary armature or stator. As the phases of the delivered power are also 120°

[2] The original air-cell was irretrievably lost. The air-cell, being difficult to remove, is dislodged from the head by backing its securing bolt by several turns and firing the engine. On the first air-cell removal iteration, the bolt was removed instead of being merely loosened. Upon firing, the old air-cell launched into the foothills west of Fort Collins.

apart electrically, when current is delivered to the armature windings in a sinusoidal waveform, the result is a magnetic field (B-field) of constant magnitude rotating at one revolution per full electrical cycle per set of windings. That is, at 60 Hz, a motor with one set of windings has a B-field rotational speed of 60 revolutions per second, or 3600 rpm.

The stator's rotating B-field exerts torque on the rotor via a magnetic field fixed to the rotor. The induction machine's rotor must slip past the stator's B-field to induce current in the rotor as its conductors cut lines of the stator's magnetic flux. The rotor current establishes a rotor B-field with a strength dependent upon the difference in the angular velocities of the stator's B-field and the rotor's conductors, as well as the design of the rotor. The motor selected for the dynamometer is a NEMA (National Electrical Manufacturers Association) class B, 2.2 kW (3 horsepower), 3450 rpm induction motor. Figure 3.5 represents the typical NEMA class B torque-speed curve. The curve is linear, or nearly so, in either direction from the synchronous speed over an interval that includes the rated operating point [Stamper and Koral, 1979].

To measure the torque, the electric motor is held at each end by bearings in a cradle. This allows free rotation of the motor. The rotation is opposed by an Omega model LC101-25 load cell secured to the side of the motor at one end and the motor cradle at the other. The position of the load cell results in a force of 58 N (13 lbf) when the electric motor is at rated power and a force of 87 N (19.5 lbf) at the electric motor's start-up torque. The range and accuracy of the load cell is -111 to $+111$ ± 0.044 N (-25 to $+25 \pm 0.01$ lbf) with safe overload excursions up to ± 169 N (± 38 lbf). The

load cell signal is displayed on an Omega DP25-S-R panel meter. The speed is measured with a Monarch ROS-5W optical transducer read on a Monarch ACT-1B panel meter which as a range of 5 to 100,000 rpm.

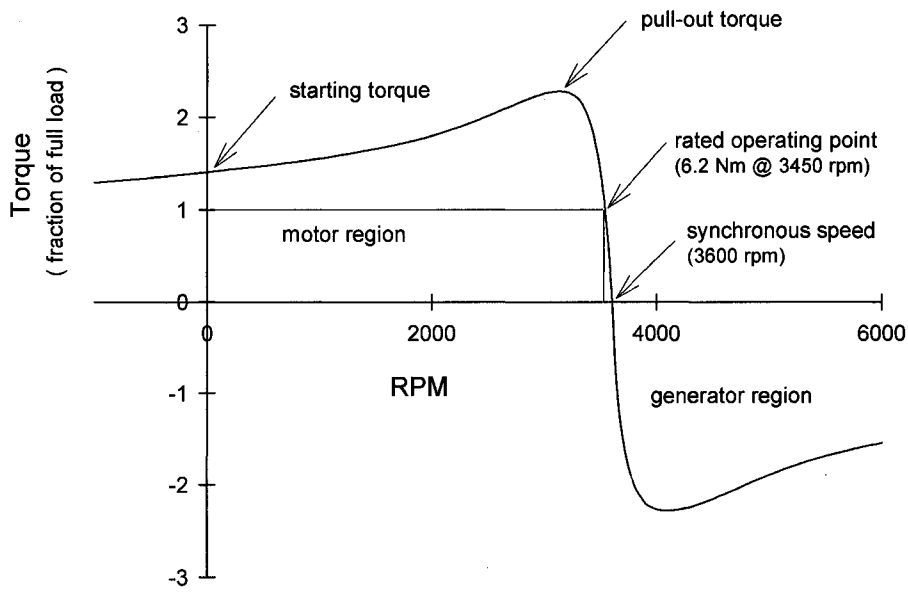

Figure 3.5 -- Induction Motor Torque-Speed Curve

The diesel engine is coupled to the induction motor by a toothed synchronous belt drive. Because of the induction motor's steep torque curve, its speed is confined to a narrow interval about its synchronous speed. Moreover, the diesel's speed equals the induction motor's speed multiplied by the ratio of induction motor pulley size to diesel engine pulley size. That is,

$$\text{rpm}_{\text{diesel}} = \text{rpm}_{\text{induction motor}} \cdot \frac{\text{diameter of pulley on induction motor}}{\text{diameter of pulley on diesel}}.$$

Changing the diesel's speed requires stopping the diesel, changing pulleys, and restarting. Since pulleys are available in fixed sizes, the diesel must be run at fixed speeds –

nominally 1500, 2000, 2500, and 3000 rpm. This is apparent in the banded nature of the data. For examples see figures 4.2, 4.3, or 4.4 in sections 4.1 and 4.2.

3.3 Fuel and Air Flow

Fuel flow was measured with a Waukesha model 819-0007 gravimetric fuel stand. The stand consists of a balance beam scale with a weight on one side and a container of fuel on the other. As fuel is consumed the fuel side becomes lighter and tips up. When the fuel side tips up, a switch is activated that simultaneously starts a timer and lifts the weight off the scale. The fuel side is then, once again, the weightier side and tips down accordingly. When a mass of fuel equivalent to the weight has been consumed, the fuel side once again tips up, this time stopping the timer and releasing the weight. The weight used in this experiment has a mass of 56.7g (⅛ lbm). The time to consume an equivalent mass of fuel was from one to fifteen minutes, depending on the speed setting and load.

Combustion airflow was measured with an altered Ford model AFH38-06 air-mass flowmeter – a Dall tube-style obstruction flowmeter. The meter was taken from a 90's model Ford Taurus found in a local salvage yard. This model was chosen on the advice of CSU's Engines and Energy Conversion Laboratory and CSU's Formula SAE Race Lab, both of which use this model. Before it could be used, the meter needed to be altered, as it was sized for an engine an order of magnitude larger in displacement than the test diesel. Inserts for the inlet, throat, and exit cone were machined to reduce the throat diameter from 3.8 to 1.9 cm (1.5" to 0.75"). This increased the throat velocity by a factor of four and the pressure difference by a factor of thirty-six. Specifically, in the

unaltered flowmeter, the theoretical air flow of a 2-liter engine at 600 and 6000 rpm caused pressure differences of 1.5 and 146.3 Pa, respectively. If the flowmeter were left unaltered, the test engine running at 1500 and 3600 rpm would have caused pressure differences of 0.1 and 0.6 Pa, respectively. In its altered form, the flowmeter pressure differences for the test engine are 3.7 Pa at 1500 rpm and 21.4 Pa at 3600 rpm. While this pressure difference is still well in the lower half of the flowmeter's range, further reduction in throat diameter is contraindicated if the altered meter's dimensions are to fall comfortably within accepted design practices.

The altered flowmeter was calibrated by placing it in line with a borrowed Venturi tube flowmeter with a pressure difference resolution of 3.4 Pa (0.001" Hg) and drawing air through with a Shop-Vac® vacuum cleaner downstream of both flowmeters. Throttling the vacuum's exhaust with duct tape varied the flow rate. The calibration curve is presented below in figure 3.6.

3.4 Data Collection

The speed of the induction motor provides verification of the load cell's readings. The induction motor's unloaded speed was checked on several occasions and found each time to be 3598 rpm. This is consistent with a synchronous speed of 3600 minus slight windage. If the induction motor performs to specifications, then its torque is 6.19 Nm (4.57 ft lbf) at 3450 rpm and -6.19 Nm at 3750 rpm. More generally, about the synchronous speed the induction motor's torque equals, in Newton-meters, $6.192 \cdot (3600 - rpm)/150$, and in foot-pounds, $4.567 \cdot (3600 - rpm)/150$. Figure 3.7

shows torque calculated from the load cell's readings along with torque calculated from the corresponding rpm of the induction motor. Of course, the data could be displayed with the load-cell-based-torque in a straight line through a surrounding cloud of rpm-based torque data points. However, the load cell readings fluctuated much more than the rpm readings with standard deviations of 8.5% and 4.3% of the indicated torque for the load cell and induction motor rpm, respectively. Thus, the rpm is deemed a more precise, though not necessarily more accurate, indicator of the induction motor's torque than load cell readings.

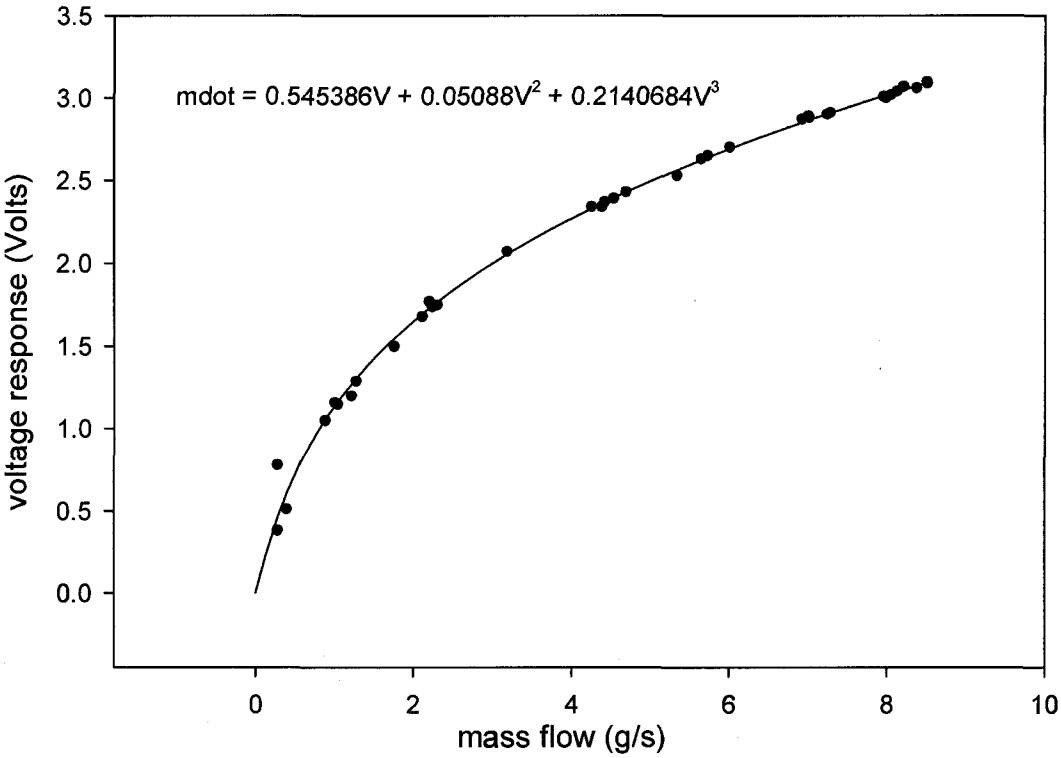

Figure 3.6 -- Flow Meter Voltage *vs.* Mass Flow

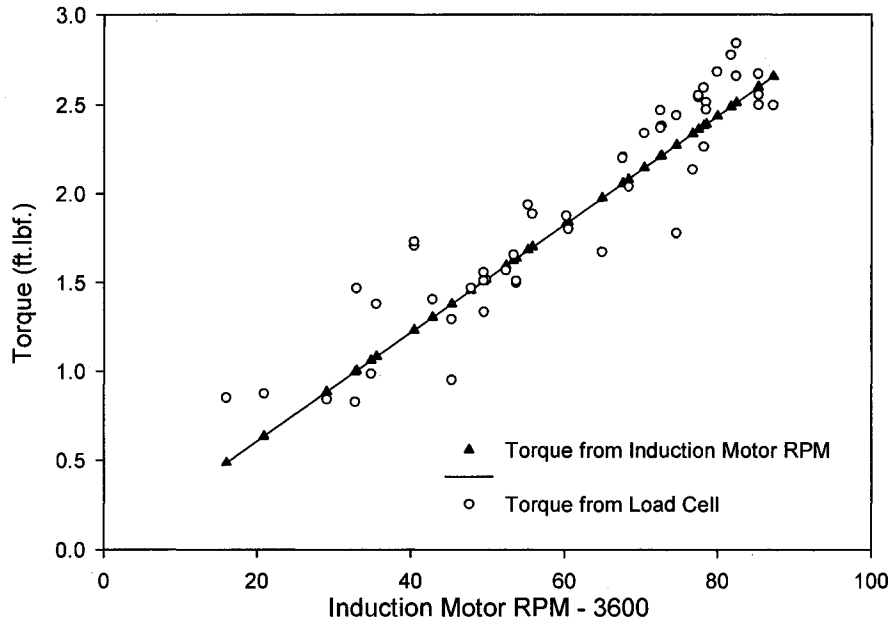

Figure 3.7 -- Torque from Induction motor RPM and Load Cell

During the several minutes required to take a fuel rate measurement, the other values (temperatures, rpm, air-mass flow, time, and load cell) are recorded four or five times and averaged later. This attenuates some of the noise in the measurements. Later, weather data from Christman Field (consisting of temperature, pressure, and relative humidity) for the middle of each fuel-metering period is added to the data set. The humidity ratio, W, or the mass of water vapor per unit mass of dry air, is determined from ASHRAE Psychrometric Chart No. 4 and added to the data set. This is used to determine the ambient air density during the test so that the volumetric efficiency may be determined (see Appendix B: Ambient Air Density).

CHAPTER 4

EXPERIMENTAL RESULTS

Typically, when gathering engine performance data, the load is set and a speed sweep is taken, or the fuel rack is set and the load varied. However, in the present work the dynamometer runs at a fixed speed until the gearing is reconfigured. Therefore, the procedure for gathering performance data is to vary the fuel setting while using a constant gearing. The torque-speed curve of the engine is then gleaned from the collection of torque versus fuel rate curves. The engine was switched from superalloy to aluminum components and back several times during the course of the experiment. In addition, data collected for a particular gearing were spread across the course of the experiment. This avoids comparing results from a newly refurbished engine run in hot weather to results from a worn engine run in cool weather. Figure 4.1, showing the torque versus fuel per cycle at a nominal speed of 2000 rpm, is typical of the fixed speed data collected. In figure 4.1, each datum has been labeled with the date of collection and the ambient temperature.

4.1 Developed Brake Torque

The engine's torque-speed curves are developed by fitting a curve through the maximum torques at each speed for each configuration. Figure 4.2 shows torque versus speed for

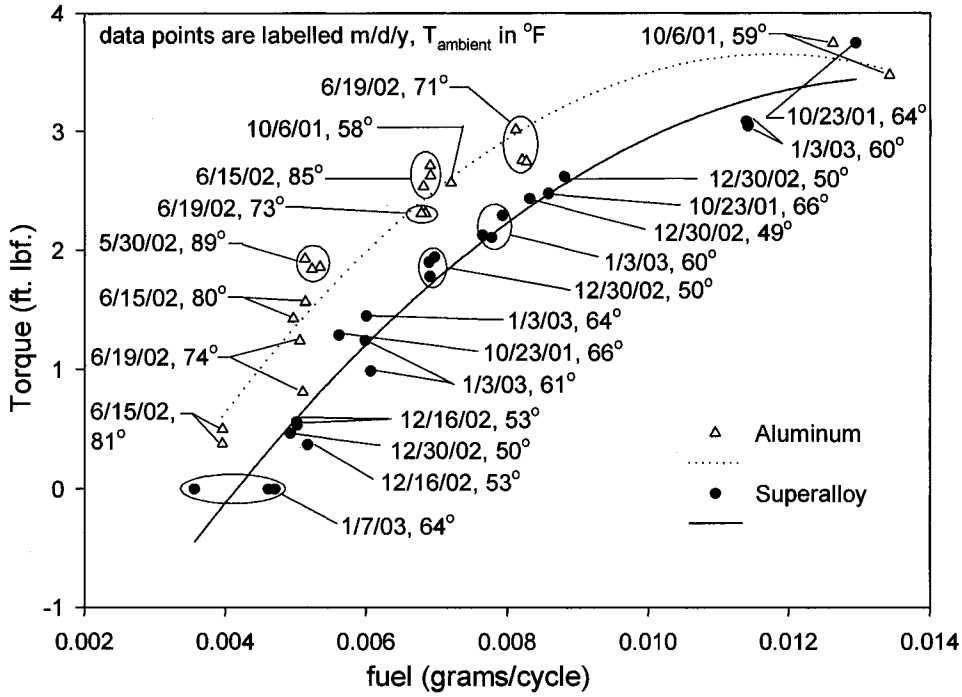

Figure 4.1--Torque vs fuel (g/cycle) at 2000 rpm

the test engine with both aluminum components and superalloy components. The developed brake torque falls short of the stock engine's specified 6.04 Nm (4.45 ft lbf), when derated for altitude, especially at low and high engine speeds. Three reasons for the low work output have been identified: piston geometry, volumetric efficiency, and combustion dynamics.

4.2 Piston Size and Mass

The experimental pistons, being heavier and taller than the original stock piston, are one reason that the measured torque falls below the engine's specifications. While the stock piston weighs in at 357 grams (0.79 lbm), the aluminum piston used in the experiment has a mass of 471 grams (1.04 lbm), an increase of 32%. The superalloy piston is 727

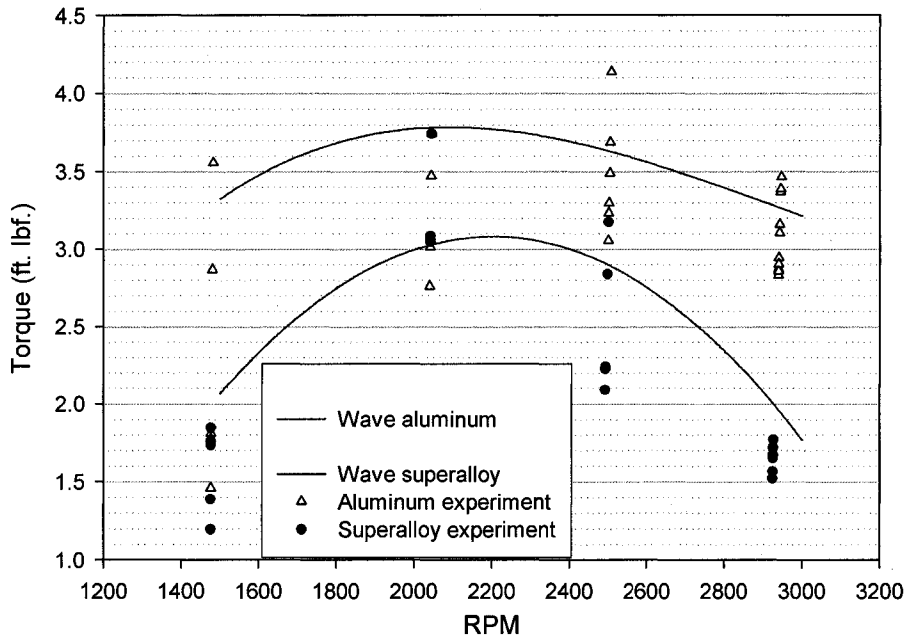

Figure 4.2 -- Brake Torque vs. RPM

grams (1.60 lbm) – fully twice as massive as the stock piston. To make matters worse, this weight is atop a stock piston, extending the height and exacerbating the moment from secondary piston motion as the mass center is moved farther from the wrist pin. To determine the magnitude of the engine friction, the test engine was motored while hot in both the aluminum and superalloy configurations. The torque required to motor the test engine is shown in figure 4.3

The best-fit curves to the motored data (shown above) are used to predict engine friction in the engine simulation program WAVE, which uses the Chen-Flynn friction model. Specifically, the Chen-Flynn relations that match the data are, for the aluminum engine,

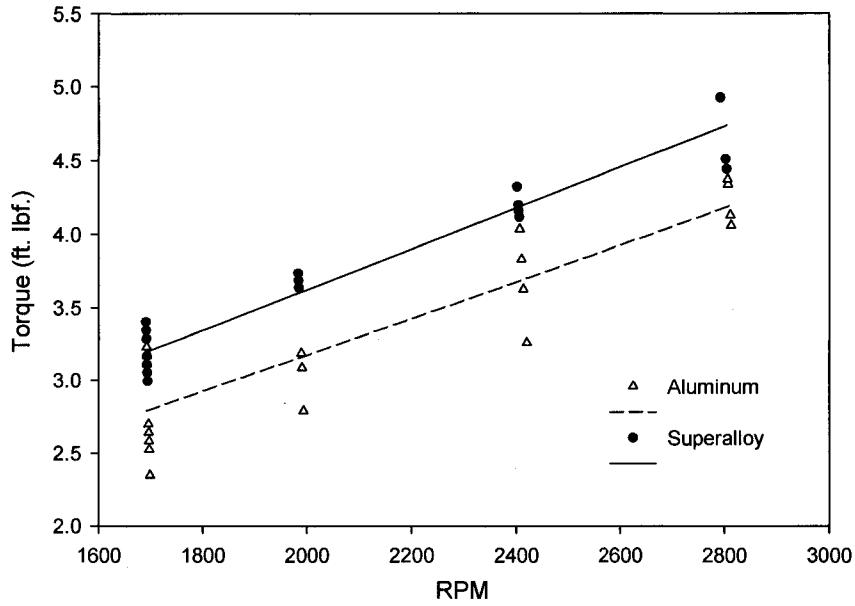

Figure 4.3 -- Motoring Torque

$$FMEP_{AL} = 0.28 + 0.006\left(P_{\max}\right) + \frac{3415}{10^5}\cdot\left(rpm\cdot\frac{stroke}{2}\right) + \frac{0.2}{10^5}\cdot\left(rpm\cdot\frac{stroke}{2}\right)^2,$$

and for the superalloy engine,

$$FMEP_{SA} = 0.4 + 0.0064\left(P_{\max}\right) + \frac{3780}{10^5}\cdot\left(rpm\cdot\frac{stroke}{2}\right) + \frac{0.2}{10^5}\cdot\left(rpm\cdot\frac{stroke}{2}\right)^2,$$

where FMEP is the friction-mean-effective-pressure in bars, the stroke is 0.057 meters, and P_{max} is the maximum cylinder pressure determined from WAVE to be 41 bars when motored (the range in maximum motored cylinder pressure from WAVE simulations ranged from $\cong$ 38 bars at 1500 rpm to $\cong$ 43 bars at 2500 rpm).

There is a significant difference in engine friction due to the difference in mass between the aluminum piston and the superalloy piston. However, the purpose of the

experiment was not to compare the effect of varying piston mass, but rather to compare a partially insulated engine to a geometrically identical un-insulated engine. Therefore, to facilitate comparison, the torque developed with superalloy components is adjusted by adding the difference in motored torque. The torque curves, adjusted for friction, are presented in figure 4.4.

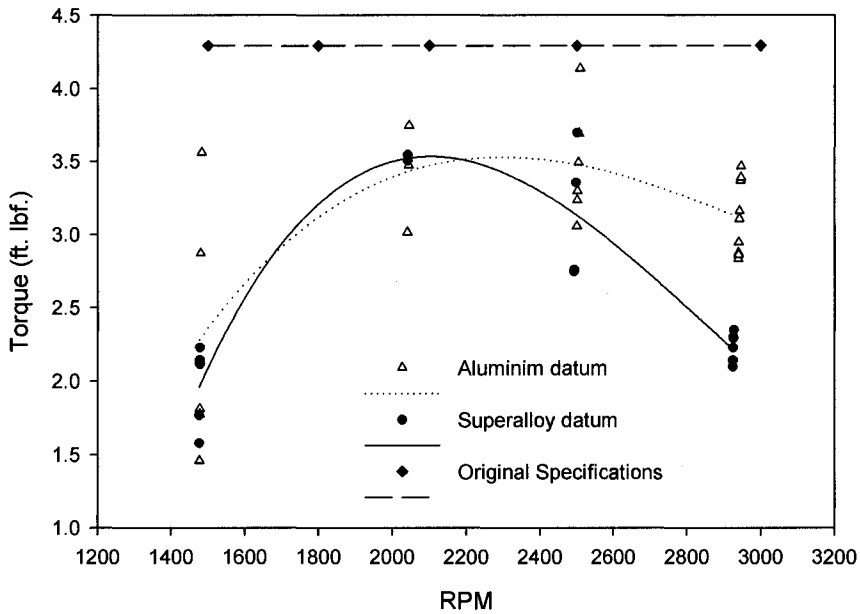

Figure 4.4 -- Friction AdjustedTorque vs. RPM
Superalloy torque corrected by difference in motored torque

There is additional justification for neglecting the friction difference due to the mass of the superalloy piston. Namely, a production LHRE's piston will be much less massive than the test engine's piston. In the test engine, the superalloy piston extension is a self-contained unit that completely encloses a ceramic gasket affixed to the top of a stock piston (see section 3.1, figure 3.2). More than two-thirds of the superalloy material lies beneath the insulating ceramic gasket where temperatures are well within the working

range of aluminum. A production LHRE engine will surely have a more integrated approach to piston design. There is nothing new or revolutionary about the concept of a piston with an aluminum base and a flame surface of more durable material. Steel faced, aluminum skirted pistons have long been a component available to the design engineer. Federal-Mogul's articulated piston shown in figure 4.5 typifies the design in practice.

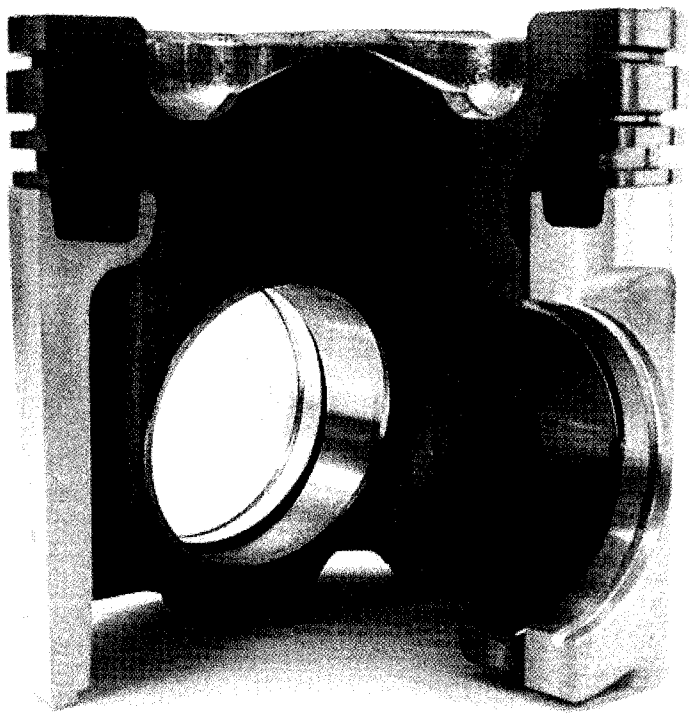

Figure 4.5 – Federal Mogul's Articulated Piston

4.3 Volumetric Efficiency

The ducting to and from the engine cylinder is longer on the test engine than on a stock engine. While the exhaust duct is only slightly longer than stock, the 132 cm length of the intake duct is five times the length of the stock engine's. The long intake duct is necessary to connect the mass airflow meter mounted on the engine stand. All other variables being equal, the long ducting of the test engine increases the intake charge over the range of speeds tested, as illustrated in figure 4.6. However, the breathing advantages gained by the long intake duct are eclipsed by a degradation of the volumetric efficiency due to intake charge heating. Figure 4.7 charts the volumetric efficiency of the test engine at full load with both aluminum and superalloy components.

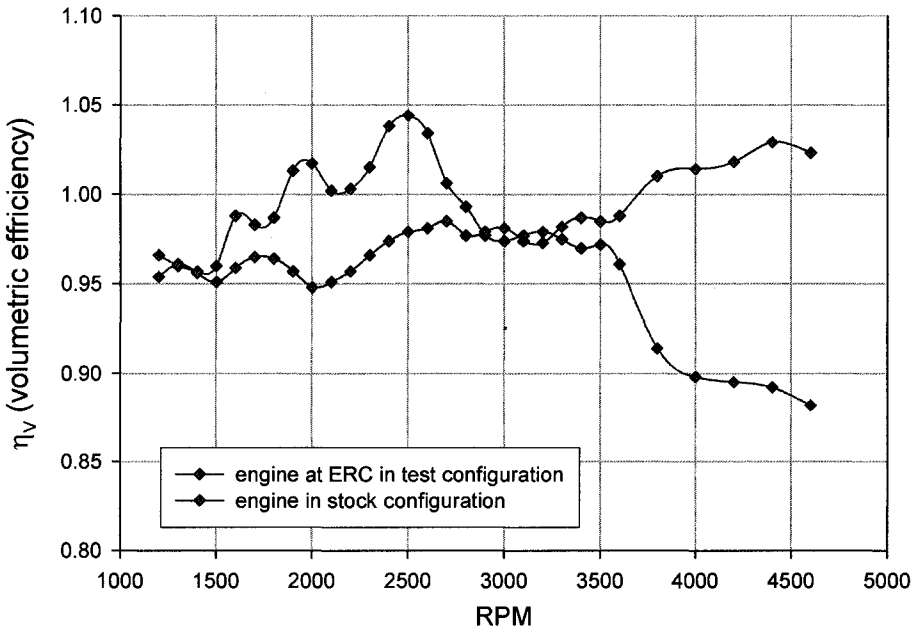

Figure 4.6 -- Volumetric Efficiency When Motored Cold
from WAVE simulations

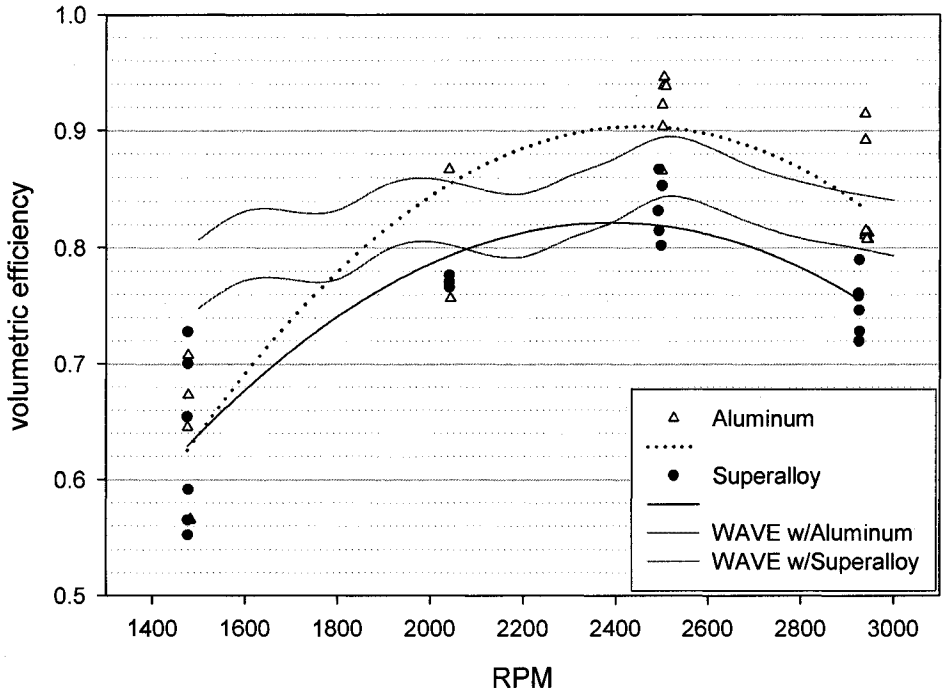

Figure 4.7 -- Volumetric Efficiency vs. RPM

Wave simulations fail to duplicate the experimental low volumetric efficiency at 1500 rpm. The airflow meter is suspected of giving erroneous readings at low engine speeds. While the meter's orifice was sized to bring the pressure differential to within its operating range, no consideration was given to pressure pulse frequencies outside of the meter's design range. The major pressure pulses from the test engine at low engine speed, being a single rather than four cylinder engine, are one-fourth the lowest frequency the meter would experience in automotive service.

4.4 Combustion Dynamics

The combustion in the test engine is, simply, not as good as in the stock engine. Absence of the air cell detailed in section 3.1, shifting the start and duration of

combustion away from the design point, and degradation of injector performance over the course of data collection due to excessive heat all contribute to poor development of firing pressure. The start of fuel injection is held constant throughout the experiment at 24° BTDC. Figure 4.8 gives the ignition delay in milliseconds versus the average cylinder gas temperature over the delay period. Figure 4.9 shows the crank angle where heat release starts versus engine speed.

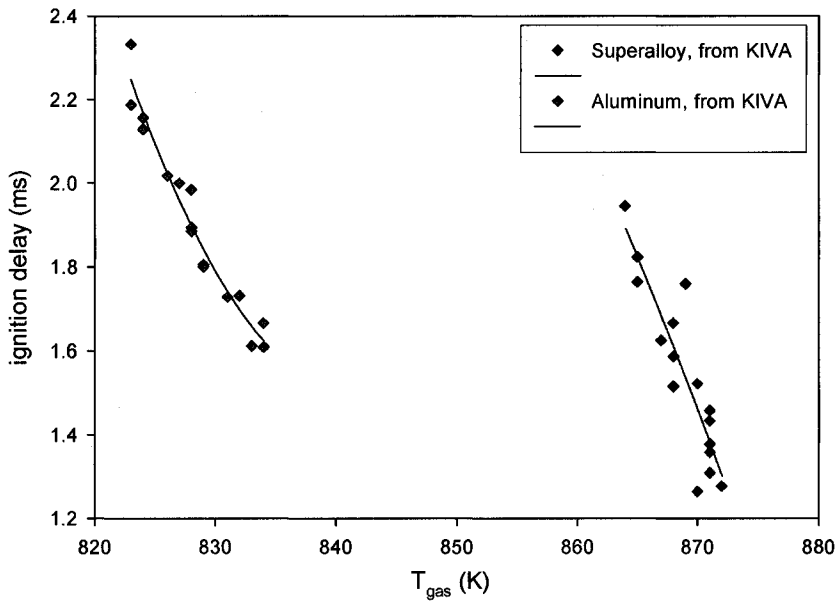

Figure 4.8 -- Ignition delay versus average gas Temperature

During the break-in period after having the engine refurbished, the developed torque was less than expected. The fuel injector was suspected as the cause and, since a new injector was at hand, it was replaced. After the data set was collected, the new fuel injector was removed and found to be sticking. A heat shield that minimizes contact between the face of the injector and the head was found to be missing. The sticking of

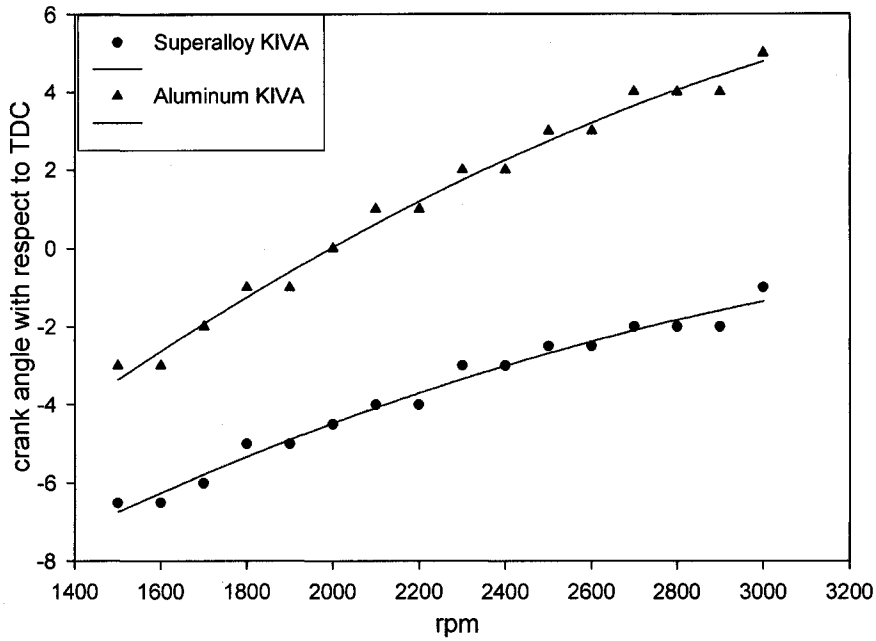

Figure 4.9 -- Start of Heat Release vs RPM

the injector needle in the nozzle body is attributed to the combined effects of higher temperatures during runs with the superalloy and a missing heat shield. These factors led to the partial breakdown of the fuel oil in the injector.

4.5 Other Performance Metrics

Multiplying the torque in figure 4.4 (back in section 4.2) by the speed gives the power in figure 4.10. Figure 4.11, shows the specific fuel consumption for the altered engine along with the stock engine. The high specific fuel consumption is due to poor torque development discussed in section 4.1, rather than over fueling the engine. The total fuel rate, as shown in figure 4.12 is mostly consistent with Lister-Petter specifications.

As energy recovery from the elevated exhaust gas enthalpy is one of the precepts of LHRE design, the exhaust gas temperature versus engine speed is given in figure 4.13 and the relative portions of work and exhaust enthalpy are given in figure 4.14. Finally, NO_x emissions versus exhaust temperature are shown in figure 4.15.

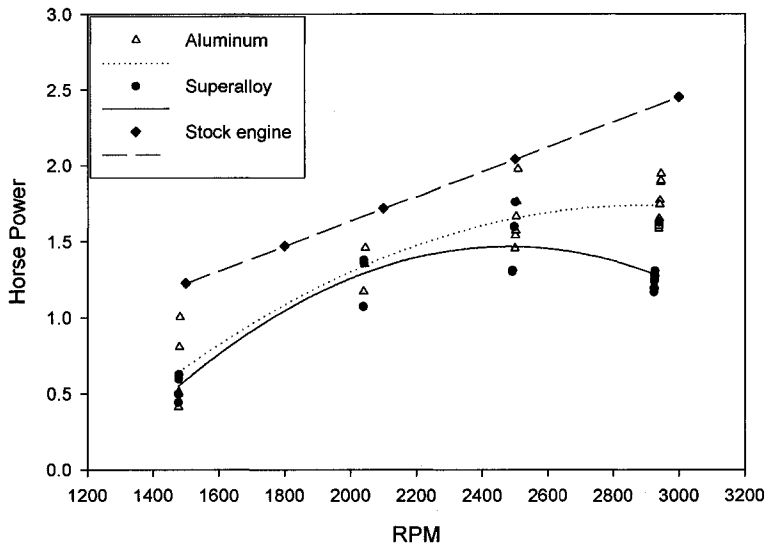

Figure 4.10 -- Power vs. RPM
Superalloy torque corrected by difference in motored torque

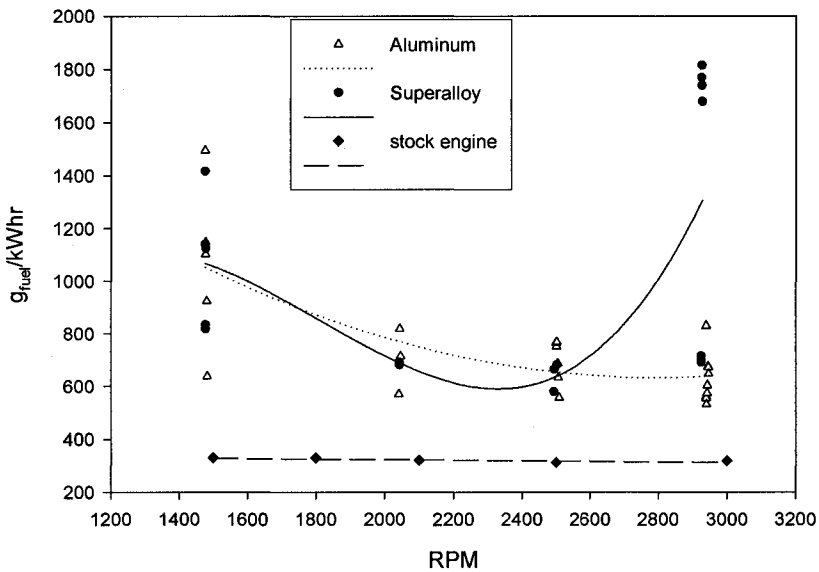

Figure 4.11 -- grams of fuel per kW hour
Superalloy torque corrected by difference in motored torque

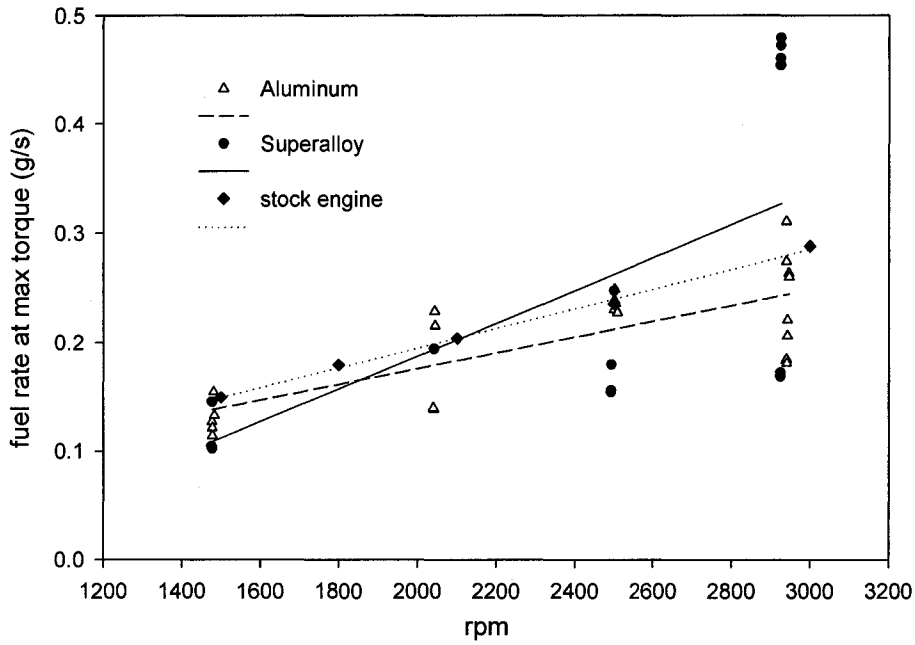

Figure 4.12 -- Overall fuel consumption at max load

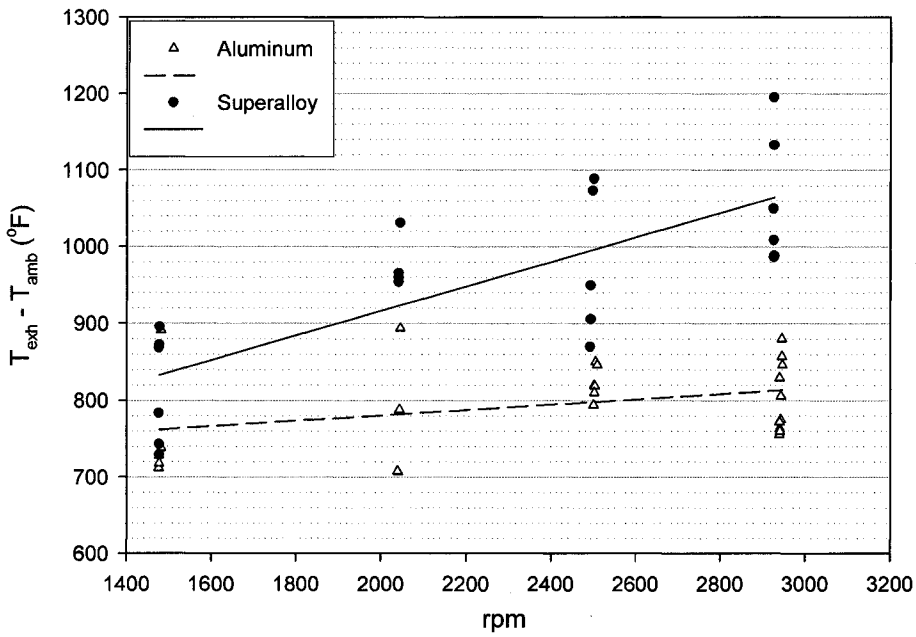

Figure 4.13 -- Exhaust Temperature

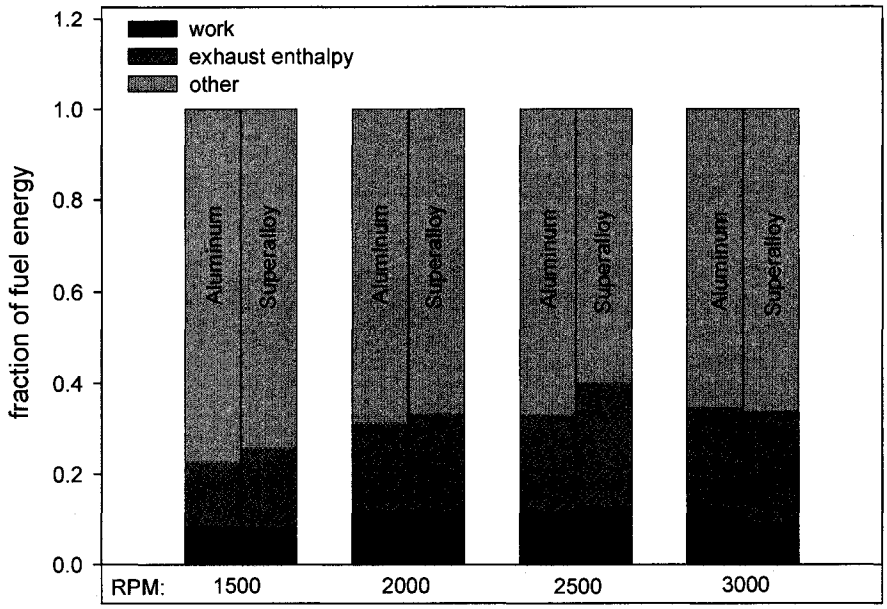

Figure 4.14 -- Fuel Conversion
with superalloy friction correction

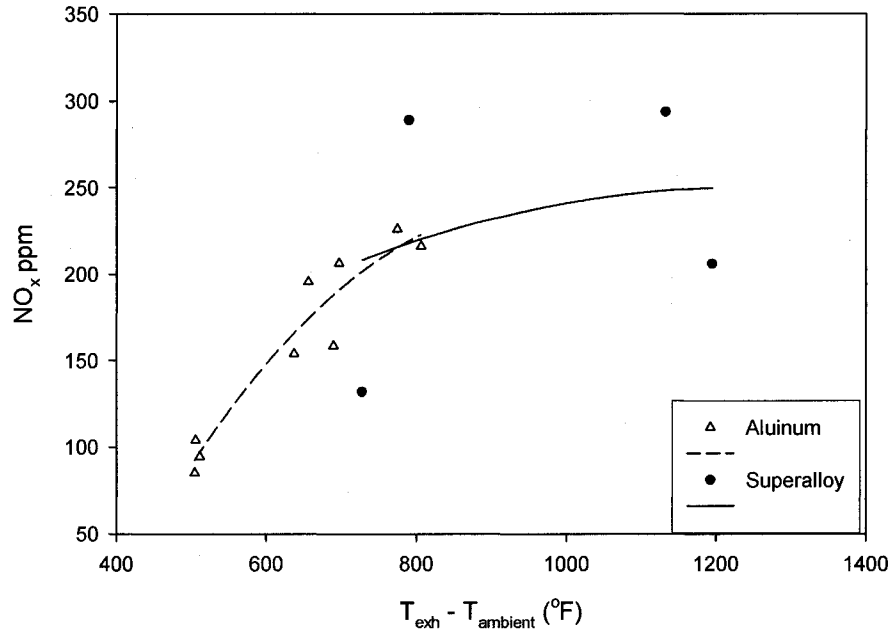

Figure 4.15 -- NO_x vs Exhaust Temperature

CHAPTER 5

MODEL CALIBRATION

5.1 Computational Models

There are two reasons for modeling the Lister-Petter AA1 diesel engine computationally. First, modeling elucidates operating characteristics of the engine as tested that can not be gleaned from the instrumentation alone. Second, modeling allows extrapolation of performance metrics from engine modifications not attempted experimentally. Three programs were used synergistically to model the test engine: Wave for engine simulation, Kiva Lite for reactive flow simulation, and JLAnalyzer for structural thermal analysis.

Wave, available from Ricardo PLC, is a one-dimensional computational fluid dynamics (CFD) code that models the unsteady, compressible flow through an engine from the inlet to the exhaust. While Ricardo offers a full complement of engine simulation software, the limited version of Wave available for this work required augmentation with a standalone reactive flow program. The reactive flow program used is Kiva Lite. Its primary relationship to Wave was to provide the combustion heat release profile used as input for Wave.

Kiva Lite, obtained from the University of Madison Wisconsin, is the scaled down version of Kiva. It uses the full Kiva solver, but there are restrictions on geometry and

operating conditions such as: only diesel fuel is modeled, no offset or asymmetrical piston bowls are allowed, and only one fuel injector is allowed. None of these restrictions has relevance to modeling the Lister-Petter AA1 engine. The inputs to Kiva, besides the fixed parameters such as engine speed and fuel rate, are the engine and manifold conditions from Wave and the surface temperatures from JLAnalyzer. The outputs are the heat release rate used as an input in Wave, the indicated mean effective pressure (IMEP), used to verify Wave, and the working fluid temperature history used as input in the finite element method (FEM) model to determine engine temperatures.

JLAnalyzer is the FEM code used to resolve the temperature profile of engine components. As a starting point, the aluminum piston model of Sanders and Schramm was reconstructed with the boundary conditions set forth in their paper [Sanders and Schramm, 1948]. Next, the superalloy piston tested at fast idle by Elshindidy was considered. The peak piston temperature at 3000 rpm was known to be 760 °C. For this case, the cylinder wall temperatures were determined, as described in report one, to be 160 °C[3]. With the oil temperature known, the cylinder gas temperature that satisfied the boundary value problem was determined.

5.2 Cylinder Wall temperatures

The purpose of taking temperature measurements at various locations on the engine's exterior is to determine the mean surface temperatures in the combustion

[3] The inner cylinder surface temperatures vary across the head and along the cylinder liner. The value of 160 °C for the cylinder temperature represents the average weighted by area.

chamber. These temperatures are then used as inputs for a compressible flow engine simulation program (WAVE) and a reactive flow combustion simulation program (KIVA). To solve for the inner surface temperatures, an FEA (finite element analysis) model is run with the predicted exterior surface temperatures as BC's (boundary conditions). The predicted exterior surface temperature BC's are simply the thermocouple readings at the locations measured, corrected by the error associated with those readings.

5.2.1 Surface Mounted Thermocouples

Exterior surface temperature readings are gathered by using thermocouple junctions attached to the engine at various locations with epoxy. The error introduced by using the temperature of a thermocouple junction encased in epoxy to represent the temperature of an adjacent surface has two components: the increase in the surface temperature due to the insulating effect of the epoxy, and the thermocouple junction temperature being below the adjacent surface temperature also due to the insulating effect of the epoxy film between junction and surface. These two effects work in opposite directions, moderating the error to some extent.

5.2.2 Thermocouple Junction Effect on Surface Temperature

To determine the distortion in the temperature field due to the presence of a thermocouple junction, a comparison of a modeled cylinder cooling fin with and without an affixed thermocouple junction was performed. The geometry is known, and temperature measurements have been taken at both the base and the tip of several cooling

fins. With these data, an FEA model was used to find the boundary conditions necessary for the modeled temperatures to match those observed. While holding these boundary conditions fixed, the model was run with and without a glob of epoxy of the appropriate dimensions in the appropriate places. The change in temperature due to the presence of a thermocouple junction is less than a half a degree Celsius at the fin tip and two degrees Celsius at the base.

The fin tip is the leading edge with respect to the flow of cooling air over the engine cylinder. Because the local convective heat transfer coefficient at a leading edge is considerably greater than the average convection coefficient, the comparison with and without epoxy was repeated using a convection coefficient an order of magnitude greater than indicated. Running the model with a higher convection coefficient yields lower temperatures overall, but the temperature difference between a bare fin tip and a fin tip covered with epoxy remains less than one degree Celsius. Thus, while the fin tip temperature is strongly dependent on the magnitude of the convection coefficient, the change in fin tip surface temperature due to the presence of an insulating patch of epoxy is not.

5.2.3 Using a Thermocouple to Predict Adjacent Surface Temperature

To determine how closely the temperature of a thermocouple junction compares to the adjacent engine surface, more FEA is used. Having the thermocouple junction in direct contact with the surface, as if welded or brazed on, whether or not the junction is covered with epoxy, gives temperatures within a quarter of a degree Celsius between the

engine surface and the junction temperature. However, in this case, the thermocouple junctions were attached to the engine by dipping the junction in freshly mixed epoxy and then holding it against the surface until cured. Therefore, it is reasonable to expect a relatively non-conductive film of epoxy betwixt surface and junction.

Rather than select an epoxy based on thermal conductivity, JB Weld was chosen for its ability to withstand the assaults of oil, fuel, and vibrations in a thermally cyclic environment. JB Weld brand epoxy has a thermal conductivity of about 0.2 W/mK. Thus, the thicker the film of epoxy between the thermocouple junction and the surface, the lower the junction temperature. For reasonable thicknesses of the epoxy film (0.05 to 0.4 mm), and typical surface temperatures (94 C above ambient at the fin tip, 128 C above ambient at the base), the junction temperature in relation to the adjacent surface temperature is -12 ±6 C at the fin tip and - 4 ±2 C at the fin base. The temperature profile of a fin tip thermocouple junction encased in epoxy is shown in the figure below in figure 5.1.

The thermocouple was modeled as solid nickel, since Chromel, the positive thermoelement of the type k thermocouple, is 90% nickel (with ~9% chromium) and Alumel, the negative thermoelement, is 95% nickel (with the balance mostly a mixture of aluminum, silicon, and manganese) [Burns, *et al.*]. In order to ascertain the model's sensitivity to the conductivity of the thermocouple, some cases were repeated with copper as the junction material. Changing the conductivity of the junction material from 43 W/mK (nickel) to 390 W/mK (copper) results in an average junction temperature ¼ C higher for the typical surface temperatures listed above. Almost an order of magnitude

increase in conductivity affects the temperature by a quarter of a degree Celsius. While the conductivity of Chromel and Alumel is not identical to pure nickel, it is certainly

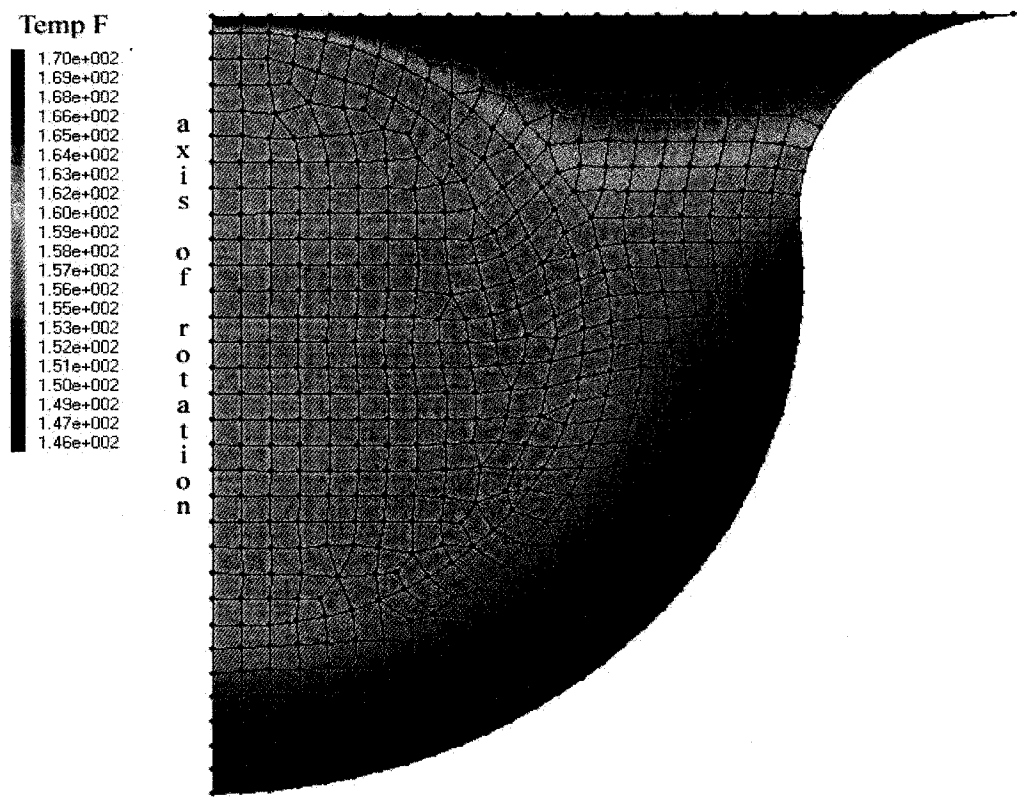

Figure 5.1 – Temperature Profile of Epoxy encased Thermocouple Junction.

much closer to nickel than to pure copper. Since a gross discrepancy in conductivity results in only a ¼ °C difference in temperature, the error associated with modeling type k thermocouples as pure nickel is deemed negligible.

5.2.4 Error Compensation

For the typical case cited previously, the combined error in the fin tip temperature is 13% of the measured value. Measurements with errors of this magnitude require some

compensation in order to have confidence in values derived from them. The goal is to find an acceptable correlation between collected data and the magnitude of the discrepancy between the measured thermocouple temperatures and the actual adjacent surface temperature. Such a correlation allows the surface temperatures to be corrected without having to run an FEA for every single set of measurements collected. The typical cooling fin temperatures cited above (94 C at the fin tip, 128 C at the base) represent a fin temperature profile in the middle of the collected data. The observed extremes are a tip and base temperature of 111 C and 155 C, respectively, above ambient for the hottest and 63 C at the tip, 94 C at the base of the coolest. Just as an analysis of the temperature error was done for the case in the middle of the temperature range, the temperature errors for the two extreme fin temperature cases were also examined. It was found that temperature error is not merely proportional to the temperature. Because data were collected over a range of engine speeds and the engine is air cooled, there is a corresponding range in the values of the convection heat transfer coefficient. Since the thermocouple junctions are epoxied onto the exterior engine surface, variations in the convection coefficient significantly affect the junction temperatures.

Determining the convection heat transfer coefficient and its functional dependency requires some basic parameters. Specifically, the length scale, the velocity, the viscosity, and the conductivity of air are required. The fin length of 19.8 mm is taken as the characteristic length. In the vicinity of the cooling fins, the air velocity is on the order of 1 m/s. These values, along with the properties of air at 50 C, yield Reynolds and Prandtl numbers of $\mathrm{Re} \cong 10^4$ and $\mathrm{Pr} = 0.7$.

From these values, the compilation of empirical correlations suggest laminar flow with a convection coefficient given by

$$\bar{h}_L = \frac{k}{L}\overline{Nu}_L = \frac{k}{L}\bullet 0.664\,\mathrm{Re}_L^{1/2}\,\mathrm{Pr}^{1/3}$$

[Incropera & DeWitt, p.366]. Because $\mathrm{Re}_L \equiv vL/\nu$, and the physical geometry is fixed, $\bar{h}_L \propto \sqrt{rpm}$. Formulating an expression for the temperature error in terms of the measured temperature and the square root of the engine speed gives:

$$\varepsilon_{ft} = -3.677903\times10^{-3} T_{ft}\sqrt{rpm},$$
$$\textit{and}$$
$$\varepsilon_{fb} = -9.510151\times10^{-4} T_{fb}\sqrt{rpm},$$

where ε_{ft} and ε_{fb} are the errors in the fin tip temperature (T_{ft}) and fin base temperature (T_{fb}). These expressions yield error values within about 4% of the values determined with finite element analysis. To more accurately determine the temperature profile of the engine cylinder, the surface temperatures used as boundary conditions in a conduction analysis are corrected by subtracting the predicted error thusly: $T_{corrected} = T_{measued} - \varepsilon_{predicted}$.

5.2.5 Uncertainty in Cylinder Wall Temperature

The uncertainty in the exterior surface temperatures is due to the uncertainty in the thickness of the epoxy between the engine surface and the thermocouple junctions. The range in thickness of 0.05 to 0.4 mm is based on direct inspection. This range gives variations in junction temperatures equal to about half of the predicted error. The predicted fin tip error averages 14.5% of the measured value (σ = 2%), giving

uncertainties of about 7%. A 13% error was reported for a case above, but that case is better behaved than most because of a low engine speed and, therefore, a lower convection coefficient.

The uncertainty traditionally associated with thermocouple readings is $\pm 0.5°C$. For the thermocouple in the oil sump and the thermocouples in the intake and exhaust streams, this is the value used. However, for the surface mounted thermocouples, this value is dwarfed by the uncertainty contributed by the epoxy thickness. To wit: $\sqrt{6^2 + 0.5^2} = 6.021$. Therefore, the uncertainty due to the epoxy thickness is by far the most significant component of the uncertainty in the surface temperature measurements.

The question of interest, now that the errors and uncertainties associated with surface temperature measurements have been identified, is, "With what certainty are the inner cylinder surface temperatures known?" In general, if a value, y, depends on values $x_1, x_2, \ldots, x_n$, then the uncertainty in y, ω_y, is related by the uncertainties $\omega_{x1}, \omega_{x2}, \ldots, \omega_{xn}$, by

$$\varpi_y = \sqrt{(\varpi_{x1}\frac{\partial y}{\partial x1})^2 + (\varpi_{x2}\frac{\partial y}{\partial x2})^2 + \ldots + (\varpi_{xn}\frac{\partial y}{\partial xn})^2}\ .$$

But rather than find the functional relationships necessary to apply this equation, a more expedient approach is to continue with FEA modeling to estimate the magnitude of the uncertainty.

Varying the surface temperatures of the cylinder cooling fin tips by 8% and the fin bases by 2%, in accordance with the surface temperature uncertainty, effects a change in

the inner cylinder wall temperature of less than 1.5% of T_{cw} (the inner cylinder wall temperature). T_{cw} was solved for in the case of the coolest fin temperature profile and found to be $107 \pm 1.4\ C$. The hottest T_{cw} was found to be 173 ± 1.1 C. The small response in T_{cw} to large perturbations of T_{ft} is due to geometry. The strong influence of convection on temperatures as they become increasingly more remote from the heat source is evident in the errors and uncertainties established for T_{ft} compared to T_{fb}. There is simply a lot of exposed surface between T_{ft} and either T_{fb} or T_{cw}. Consequently, in solving the conduction/convection problem, significant changes in T_{ft} require the value of the convection coefficient boundary condition to be altered much more (~20%) than the inner cylinder wall temperature boundary condition. The bad news that emerges from this analysis of the temperature measurements is that there are some alarmingly large errors and uncertainties. The good news is that, despite some large errors and uncertainties, the temperature of interest, T_{cw}, can still be known with reasonable surety.

5.2.6 Thermocouples in a Blind Hole

The cylinder extension has a thermocouple inserted into a blind hole with the junction placed 2½ mm (0.1") from the inner cylinder wall. Attia, Cameron, and Kops conducted a study of the distortion of the thermal field due to the presence of a thermocouple junction in materials with an imposed temperature gradient. The correlations they presented determine the error in the measured temperature based on the temperature gradient, material conductivities, and hole diameter. Using Attia *et al.*'s methodology, the temperature measurement error would 0.02 °C. Unfortunately, Attia *et*

al.'s work was done with the heat flux perpendicular to the thermocouple hole. In the cylinder extension, the thermocouple is inserted so that the direction of heat flux is mostly parallel to the thermocouple hole.

To establish an upper bound for the cylinder wall temperature, the FEA model was used with thermocouple temperatures that exceeded the maximum recorded values by 10%. Specifically, the maximum cylinder extension temperature recorded with superalloy components was 176 C (316 °F) above ambient while 194 C (350 °F) was used in the FEA model for error estimation. At 194 C above ambient, thermocouple junctions in the aluminum and superalloy cylinder extension are 1.0 C and 1.2 C, respectively, below the temperatures found in the absence of thermocouple junctions. Rather than compensate for the error, these values are taken as the uncertainty in the cylinder extension temperature measurements.

5.2.6 The Cylinder Temperature Profile

The inner cylinder wall temperature, T_{cw}, was calculated with FEA for every data set that included a fin tip and base temperature measurement (T_{ft} and T_{fb}). The problem in constructing a cylinder temperature profile is that the majority of temperature measurements along the cylinder are fin base measurements only. What is needed is a way to predict T_{cw} based on engine speed and T_{fb}, but not T_{ft}. The functional form of an equation relating T_{cw} to T_{fb} and rpm is derived from fundamental principals of heat and energy transfer. Conservation of energy means that all the heat conducted and convected

into T_{fb} equals the heat conducted and convected out. Using conservation of energy in concert with Fourier's law of conduction and Newton's law of cooling gives

$$q'' = h \cdot T_{fb} \propto k(T_{cw} - T_{fb})$$

from which T_{cw} may be isolated

$$T_{cw} \propto T_{fb} + \frac{h}{k} \cdot T_{fb}.$$

The proportionality symbol is used instead of an equal sign because no attempt is made to quantify all of the heat transfer paths about the fin base. Rather, since conduction and convection across the engine cylinder is a complex problem, the solution will be fit to empirical data. To that end, h is put in terms of engine speed, $h \propto \sqrt{rpm}$, and two constants are inserted so that the "$\propto$" may be replaced with an "=". The explicit equations that best fit the data set are, respectively,

$$T_{cw} = y_0 + a \cdot T_{fb} + b \cdot T_{fb} \cdot \sqrt{rpm}$$

and

$$T_{cw} = -0.6218 + 1.002 \cdot T_{fb} + 0.001397 \cdot T_{fb} \cdot \sqrt{rpm}.$$

The results of this equation compared against the values of T_{cw} calculated directly from FEA are within 1 °C. But, to quote Miguel de Cervantes' Don Quixote, "The proof of the pudding is in the eating.[4]" The cylinder wall temperatures from the above equation are used as boundary conditions for an FEA model to establish the cylinder temperature profile. The fin base temperatures from this profile are also within 1 °C of the actual values. An example of a cylinder temperature profile is given in the figure 5.2 below.

[4] Miguel de Cervantes is often cited as the source of this familiar proverb. It certainly appears in his work, Don Quixote, published in 1615, but other sources date the phrase to as early as the 14th century.

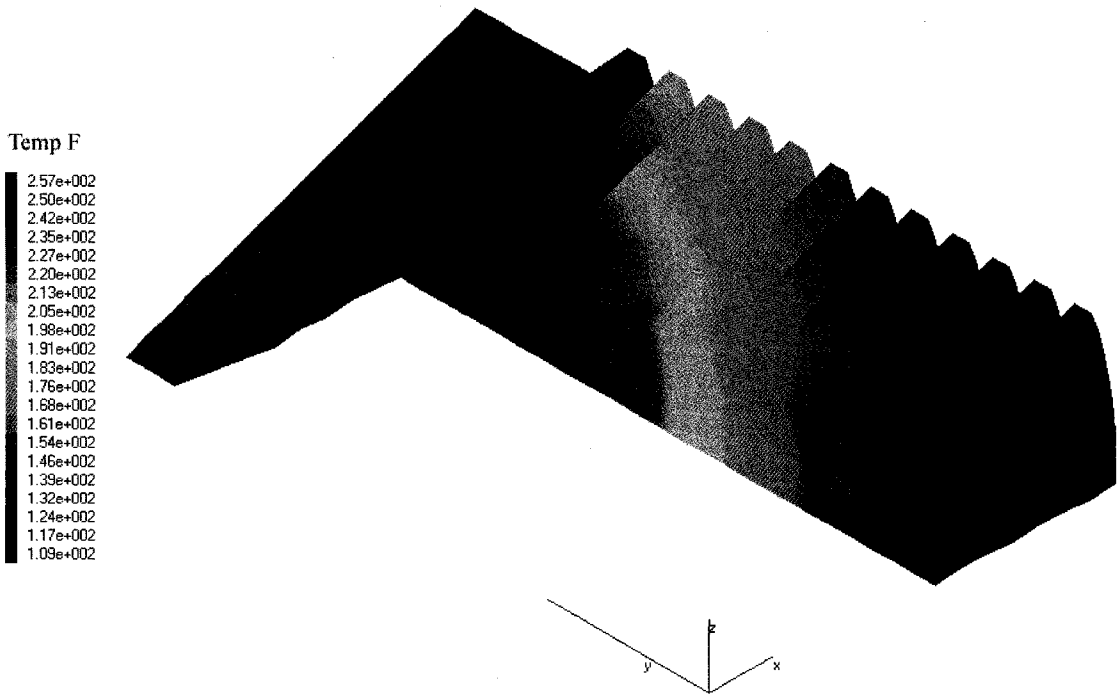

Figure 5.2 – Cylinder Temperature Profile

Incidentally, an equation was found for the convection coefficient as a function of engine speed. $h = -8.55 + 1.045 \cdot \sqrt{rpm}$ is a curve fit to the range of convection coefficients solved for, across the range of engine speeds. It is plotted in figure 5.3.

5.3 Coordinating the Models

The convection coefficient was fine tuned using Kiva. The temperatures determined from the FEM code were used as inputs for Kiva (along with fuel rate, etc.) and the resulting time varying gas temperature examined. The convection coefficient was adjusted until Kiva and JLAnalyzer were in agreement. For cases other than idle at 3000 rpm where the piston peak temperature is not known, a similar iterative approach was

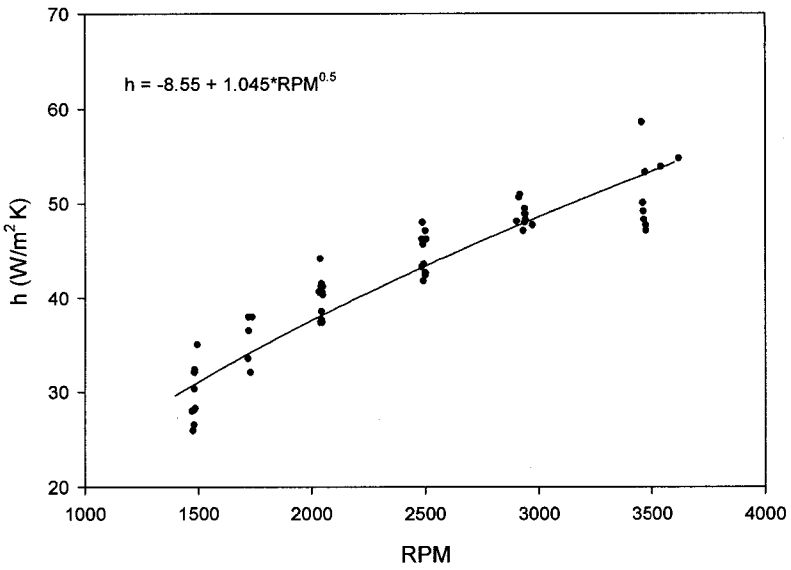

Figure 5.3 -- Convection Coefficient vs Engine Speed

used, but the piston temperature was shifted while the convection correlation remained fixed. Also, the injector spray was adjusted so that the emissions predicted by Kiva were similar to the data taken while also keeping exhaust temperatures equal to the experimental data. The interdependence of the three models is shown in table 5.1.

Table 5.1 – Parameter usage schedule.

variable	**FEM**	**KIVA**	**WAVE**
T_{gas}	input from Kiva	OUTPUT	output
$T_{surface}$	OUTPUT	input from FEM	input from FEM
fuel rate	--	fixed input	fixed input
heat release	--	OUTPUT	input from Kiva
speed	fixed input	fixed input	fixed input
$P_{manifold}$	--	input from Wave	OUTPUT
$T_{manifold}$	--	input from Wave	OUTPUT
MEP	--	output	OUTPUT
Pressure	--	output	OUTPUT
Torque	--	output	OUTPUT

Figure 5.4 shows the steady state surface temperature at the center of the superalloy piston at 3000 rpm idle. Similar plots were used for other loads and speeds to determine the corresponding piston temperatures.

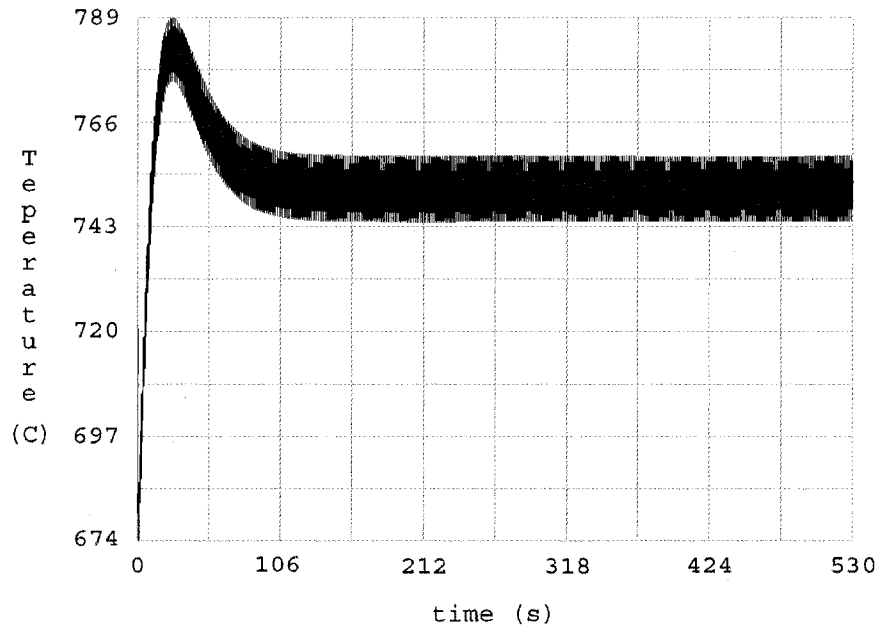

Figure 5.4 – Superalloy Piston Center Surface Temperature at 3000 RPM Idle

Figure 5.5 shows the heat release profile predicted by Kiva for the superalloy piston at 3000 rpm at full load. The heat release profiles are typified by an initial spike followed by a ramp that tails off for thirty to fifty degrees of crank angle. For the range of speeds modeled, the start of heat release varies from 6.5 degrees BTDC for the superalloy at 1500 rpm to TDC for the Aluminum at 3000 rpm. The profile used in Wave is superimposed over the heat release profile predicted by KIVA. The Wave profile is defined by seven points that are scaled to approximate the KIVA-predicted profile for each case.

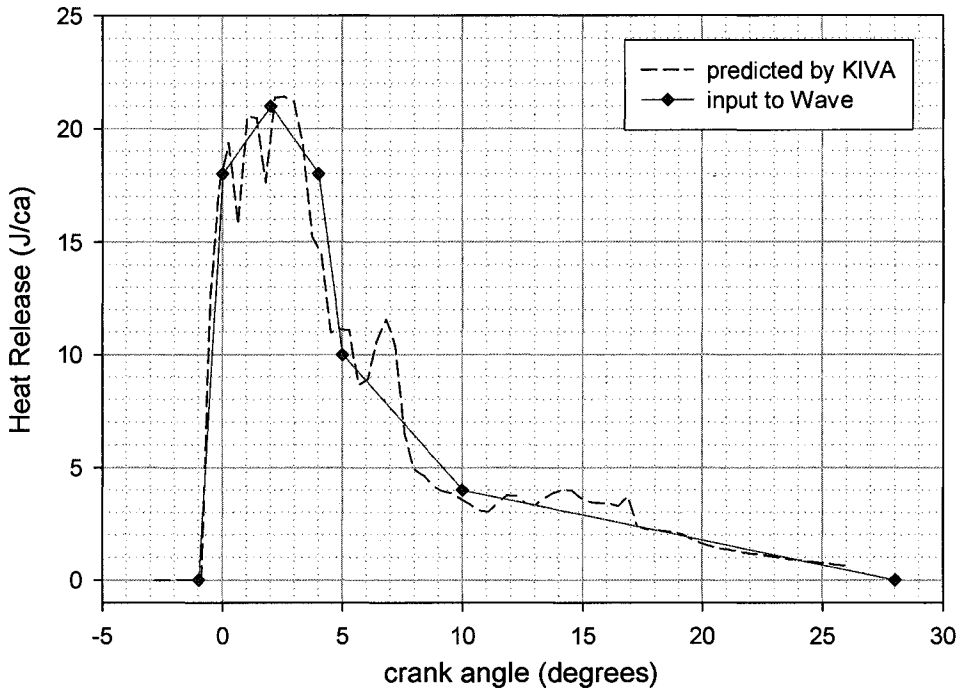

Figure 5.5 -- Heat release profile in superalloy engine at 3000 rpm

CHAPTER 6

MODEL RESULTS

As shown in section 4.2, figure 4.4, the torque developed in the aluminum and superalloy engines is similar up through 2500 rpm before diverging. At 3000 rpm, the superalloy engine's torque has fallen to 75% of the aluminum engine's. Therefore, to facilitate meaningful comparisons, analysis of the potential for exhaust energy scavenging is restricted to 2500 rpm – the highest rpm for which a given fuel rate produces a similar torque response in the aluminum and superalloy engines.

6.1 Exhaust Energy Recovery

Simply fitting a turbine on the exhaust reduces the net torque. Without an intake compressor, the air mass flow rate ($\dot{m}_{air}$) falls as turbine output and subsequent exhaust backpressure is increased. Since work depends on mass flow, net engine torque monotonically decreases as turbine torque increases. Boosting the intake pressure with a compressor sized to maintain mass flow at naturally aspirated levels allows examination of the exhaust stream's work potential. There are three reasons for limiting the compressor size so that the naturally aspirated mass flow rate is maintained:

1 Comparisons between the model and the experiment are more meaningful when the operating conditions are the same.

2 Maintaining not only $\dot{m}_{air}$, but the fuel/air equivalence ratio (ϕ), and the heat release (q) reduces the extent of extrapolation asked of the model, which has been calibrated to simulate the test engine.

3 Fixing $\dot{m}_{air}$, along with other parameters, helps restrict the focus to the effects of implementing an LHRE strategy rather than, say, optimizing the degree of hybridization of a Diesel-Brayton cycle.

To elaborate on point three, unconstrained optimization would yield a large compressor and turbine with the test engine serving as a pulsating combustor in a Brayton cycle turbine engine. This is because the fuel conversion efficiency of the test engine is less than the product of the turbine and compressor efficiencies.

In the model the turbine and compressor efficiencies were both set to 0.72 with a mechanical efficiency of 0.9 for a net efficiency of 0.65. While these efficiencies are impractical for the single cylinder 219 cm^3 displacement test engine, they are within the typical target design range for turbine and compressor equipped engines. Figure 6.1 shows the net torque response as turbine size is increased with constant $\dot{m}_{air}$ for the Wave-modeled engine in both aluminum and superalloy configurations. The increased exhaust enthalpy of the superalloy insulated engine translates into a 4% increase in work.

This potential increase in brake torque is not apparent in the experimental results presented in chapter four because no attempt was made to produce work from the exhaust

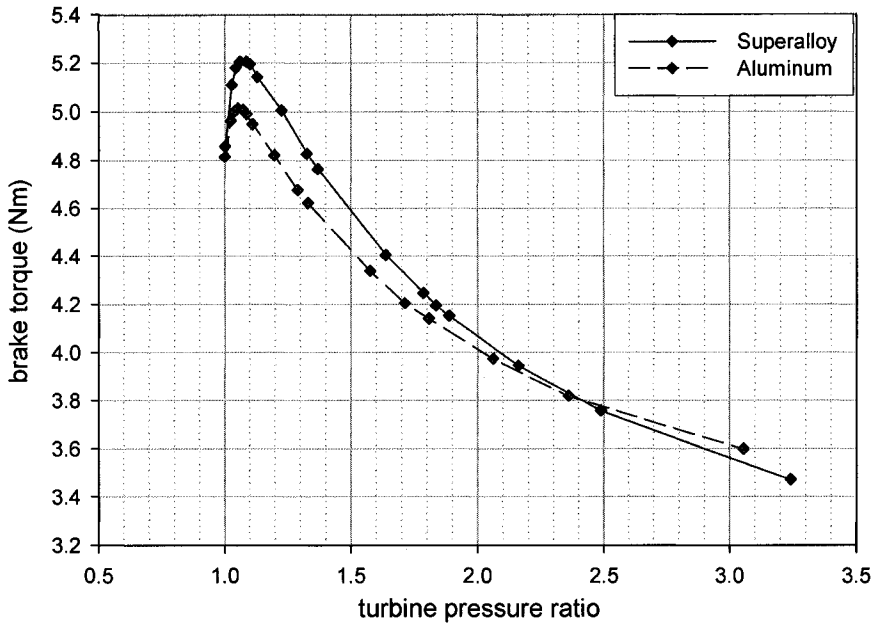

Figure 6.1 -- Brake Torque vs Turbine Pressure Ratio, 2500 rpm
compressor sized so air mass flow = constant

enthalpy. Also, in the experiment, the decrease in volumetric efficiency due to intake charge heating makes it unclear whether the commensurate drop in torque might be offset by exploiting the increase in exhaust enthalpy. Figure 6.1 reveals that scavenging work from the elevated exhaust enthalpy of the low heat rejection engine can more than compensate for intake charge heating. Further, figure 6.4, presented in section 6.3, and the associated discussion of intake charge heating point to gains greater than the 4% torque increase of figure 6.1 above. However, figure 4.4 from section 4.2 cautions that insulating the engine is not without pitfalls and complications.

In the naturally aspirated engines at 2500 rpm, the pumping work in the superalloy and aluminum engines is 9.0 and 8.1 percent of the indicated work, respectively. When fitted with the turbine that produces the maximum net torque while the compressor

maintains the naturally aspirated $\dot{m}_{air}$, the compressors on the aluminum and superalloy engines require, respectively, 2.02 and 1.40 times the work that the turbine produces. However, the pumping work done by the piston is reduced. The result is a net increase in flow work (piston plus compressor) of 2.4% and 4.6% of the indicated work for the aluminum and superalloy engines, respectively. This increase in flow work is offset by turbine contributions amounting to 3.4% and 6.0% of the indicated torque for the aluminum and superalloy engines, respectively.

6.2 Optimizing the Degree of Insulation

As the degree of cylinder insulation is increased, the energy required to overcome intake charge preheating eventually exceeds the energy that can be produced from the exhaust enthalpy by a turbine. Figure 6.2 reflects this.

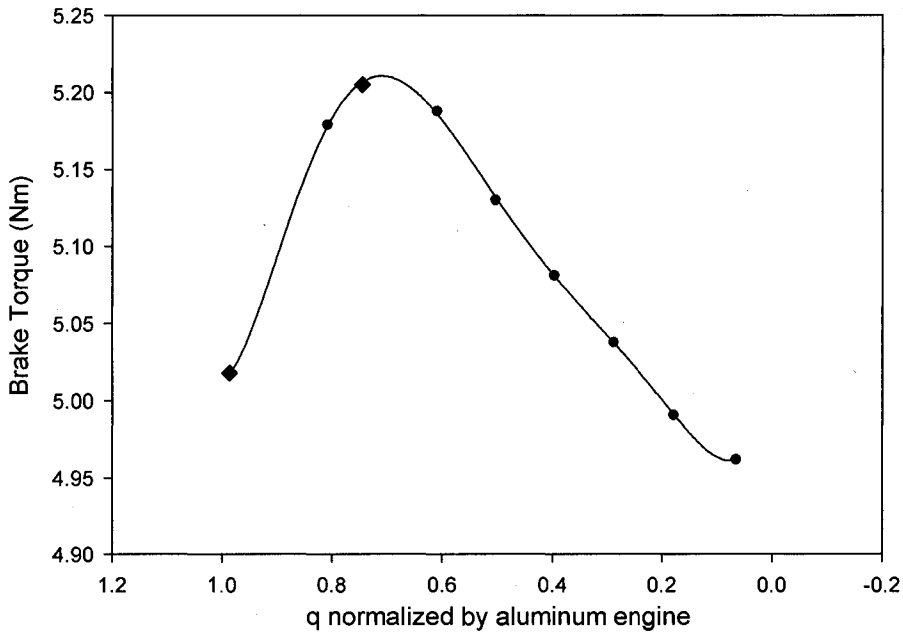

Figure 6.2 -- brake torque with optimal turbine & compressor vs. in-cylinder heat loss

The two larger diamond shaped points in figure 6.2 represent the Wave model of the two configurations tested in the experiment, but fitted with turbines and compressors. These two data points are the maxima of the curves in figure 6.1. They are modeled with different temperatures of the cylinder surfaces (that is, $T_{piston} \neq T_{head}$). The other data points of figure 6.2 are with the inner cylinder surfaces held at a uniform temperature. An increase from 5.0 to 5.2 Nm of torque represents approximately a 1% increase in thermal efficiency. Investigating the in-cylinder heat transfer as the average surface temperature increases yields figure 6.3:

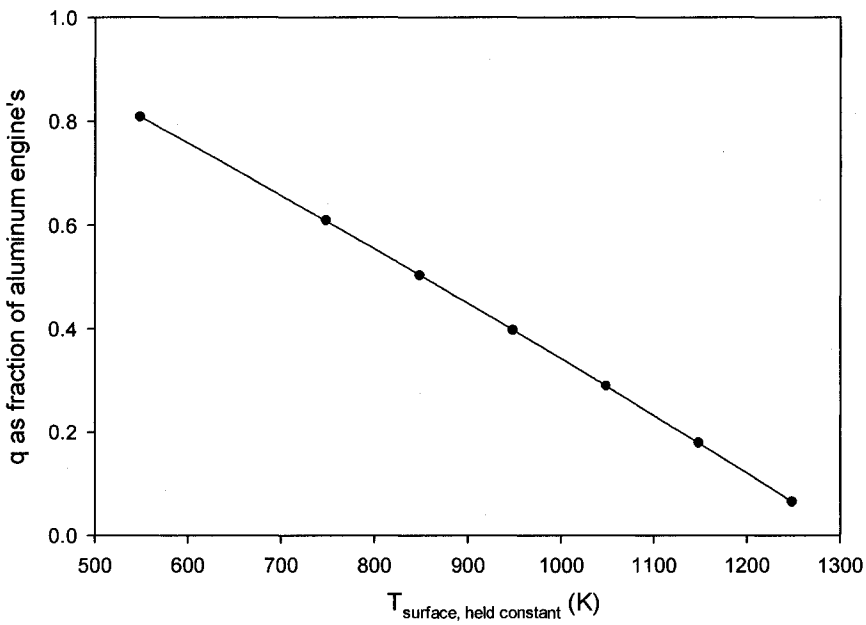

Figure 6.3 -- In-cylinder heat transfer vs. cylinder temperature

The curve of figure 6.3 is nearly linear because $\dot{m}_{air}$ is maintained at 14.23 kg/hr and the intake ducting temperature is also held at the levels of the superalloy fitted test

engine. From the time history of the superalloy piston surface, shown in figure 5.4 section 5.3, the temperature varies by less than 20 C during the cycle. This shows that temporal, if not spatial, constancy in component temperature is an acceptable approximation. It should be noted that there are spatial variations in cylinder surface temperatures. The average uniform temperature on the abscissa of figure 6.3 does not imply a specific or maximum working temperature.

6.3 Intake Charge Preheating

While calibrating the Wave model, it was noticed that the volumetric efficiency (η_v) is more sensitive to variations in manifold wall temperatures than to variations in cylinder surface temperatures. This is not surprising since the intake port volume is comparable to the displacement volume while the intake stroke is only one quarter of the cycle. Thus, combustion air exposure to the intake manifold and port surfaces is some three times greater than its exposure to the cylinder surfaces as it sojourns from ambient to trapped charge. To illustrate the relative sensitivity to surface temperature, the model was run with all surface temperatures held at 298 Kelvin (the model's ambient) except for either the valve ports or the piston surface, which were varied from ambient to 1400 K in 100 K increments. The resulting volumetric efficiencies are plotted in figure 6.4.

The upper temperature of 1400 K in figure 6.4 represents the approximate maximum continuous working temperature of HAYNES 230 superalloy (HAYNES suggests a maximum of 1423 K). Bear in mind that the valve ports will have temperatures below the cylinder temperatures. Thus, the high end of the temperature

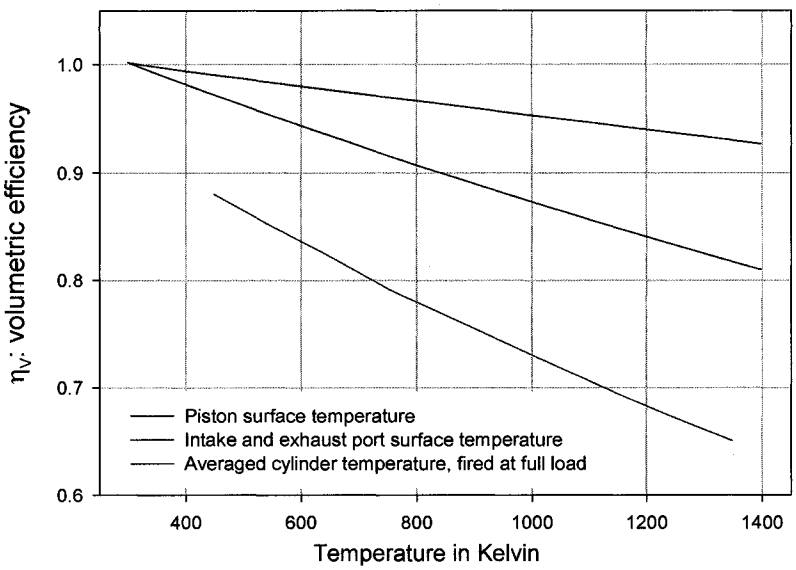

Figure 6.4 -- Naturally aspirated volumetric efficiency vs. surface temperature

range is presented not to indicate a practical range, but rather to elucidate the nature of the temperature-η_v relationship. In any event, the Lister-Petter test engine to which the curve applies has an aluminum head with $T_{melt} < 900K$. HAYNES 230 superalloy has $T_{melt} \cong 1570K$.

Because the aluminum head of the Lister-Petter AA-1 engine has intake and exhaust ports in close proximity, preheating of the intake charge is not insignificant. Figure 4.7 from section 4.3 attests to this. This, along with the temperature sensitivity illustrated in figure 6.4, suggests that insulating the intake port from the exhaust port and cylinder may be as effective as insulating the cylinder when the goal is to increase the usable exhaust enthalpy as part of a scheme to maximize net work. Or, more simply stated, the hotter an engine runs, the more care is required to mitigate intake charge preheating.

Figure 6.5 shows the cumulative heat transfer from the inner cylinder surface to the working fluid for the naturally aspirated aluminum and superalloy Wave model. The heat transfer curve for the compressor and turbine fitted engines is similar with $q_{superalloy}$ = 386 kilojoules per kilogram of working fluid and $q_{aluminum}$ = 511 kJ/kg.

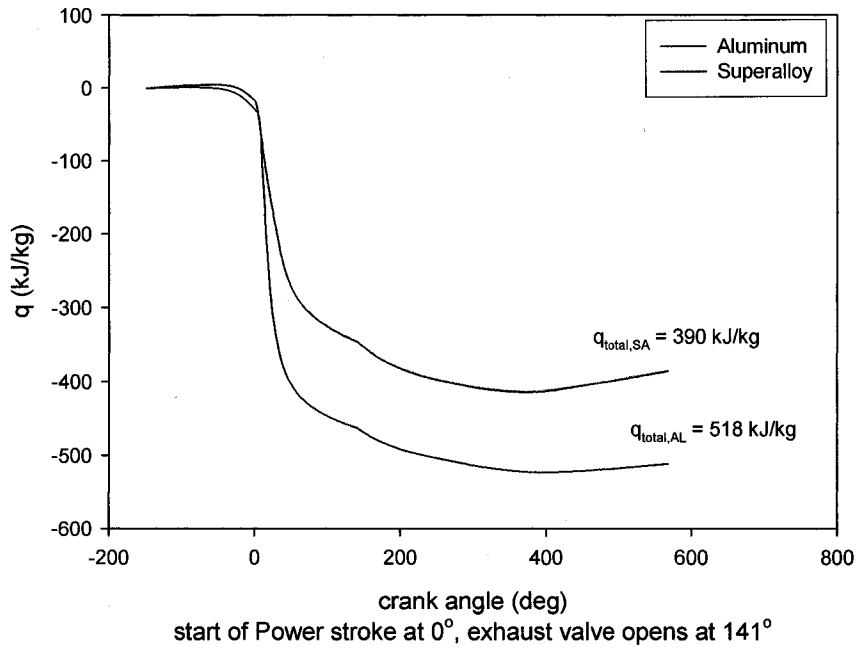

Figure 6.5 -- cylinder heat transfer to the working fluid

The adiabaticity of the idealized cycle represents the unachievable limit of zero heat transfer. Even the most exotic low conductivity materials can not reduce the gap between the ideal and the achievable to a negligible size. There will always be some heat transfer from the cylinder walls to the cool intake charge, which increases the Pdv work required during the compression stroke. Also, the enthalpy of the working fluid will always suffer as some heat is transferred from the hot combustion gasses to the cooler cylinder walls. This reduces the Pdv work done during the power stroke.

6.4 Comparison with Idealized Cycle

To investigate the upper limit of benefit that might possibly accrue from insulating the combustion chamber, an adiabatic idealized cycle was examined. Rather than apply the heat release profile obtained from KIVA for the test engine to the idealized cycle, the results of the idealized cycle with both constant pressure and constant volume combustion are presented. The gas state at effective exhaust valve opening (EVO)[5] of the idealized test engine with the KIVA heat release profile would yield something between the two. The idealized cycle starts with air at ambient test conditions ($P_{ambient}$ = 0.83 bars, $T_{ambient}$ = 298 K). The intake charge is then compressed to $1/17^{th}$ of the ambient volume. Fuel at $T_{ambient}$ is injected and burned to completion at both constant pressure and constant volume. Lastly, the products are allowed to expand isentropically to the volume at effective exhaust valve opening. Ideal gas behavior with varying specific heats is used. Pressure and temperature at EVO, along with the thermal efficiency of the cycle, are presented in table 6.1 below.

Table 6.1 – gas state at EVO for various engine configurations

Engine Configuration	**P at EVO (bars)**	**T at EVO (K)**	$\eta_{TH,\ indicated}$
Aluminum, naturally aspirated	2.49	915	0.311
Superalloy, naturally aspirated	2.93	1084	0.308
Idealized, Diesel combustion	3.90	1463	0.384
Idealized, Otto combustion	3.47	1301	0.421

To be sure, in-cylinder pressure prior to blowdown is not the same as exhaust pressure available at the turbine inlet. However, the relative exhaust states in the various

[5] Effective exhaust valve opening is where $\dot{m}_{exhaust} = 0.05 \cdot \dot{m}_{exhaust,\max}$

engine configurations prior to blowdown are indicative of the relative pressures at the turbine inlet. For example, installing the superalloy components increases in-cylinder gauge pressure at EVO by 27% $\left((2.93-P_{amb})/(2.49-P_{amb})=1.265\right)$. When the aluminum and superalloy engines are modeled with the turbine/compressor combination that results in maximum brake torque, gauge pressure at the turbine inlet increases by a similar 30% $\left((1.108-P_{amb})/(1.044-P_{amb})=1.299\right)$.

The available pressure, relative to ambient, is of more interest than the temperature alone because most exhaust energy scavenging strategies involve turbines rather than, for example, sterling cycle heat engines.

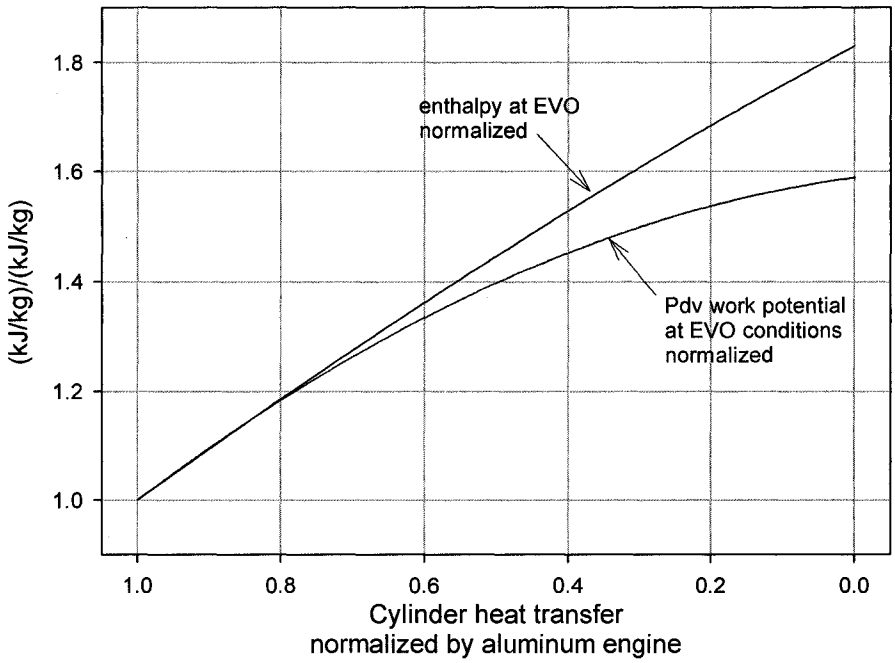

Figure 6.6 -- Enthalpy and Pdv work potential at Exhaust Valve Opening normalized by the values of the uninsulated aluminum engine

There has been some success in using thermoelectric generators on the exhaust for electric power generation. As an example of a practical application, Hi-Z Technology

Inc. offers a 1 kW thermoelectric generator for commercial diesel trucks[6]. However, in an LHRE, a thermoelectric generator (TEG) should augment an exhaust energy scavenging scheme rather comprise the whole of it. This is because the exhaust temperature of the LHRE exceeds the upper temperature limit for state of the art TEG's while turbine outlet temperatures are better suited for them. The TEG available from Hi-Z has a maximum continuous high temperature limit of 523 K with allowable excursions up to 673 K [Bass, Kushch, and Elsner 2001; Bass, Elsner, and Leavitt 1994].

[6] Hi-Z Technology, Inc., 7606 Miramar Road, San Diego CA 92126-4210
Tel: 858/695-6660, e-mail: info@hi-z.com, website: http://www.hi-z.com/

CHAPTER 7

EXACT SOLUTION TO SIMPLIFIED ENGINE HEAT TRANSFER

7.1 The Governing Equation and its Solution

To further elucidate the effect of different materials and insulation levels on engine heat transfer and its impact on the diesel cycle, an exact solution to the cylinder wall heat transfer problem is examined. Figure 7.1 illustrates the problem. To make the problem tractable, some simplifications are implemented. These are:

1) Conduction is one-dimensional.
2) The convection coefficient, $\overline{h}$, is constant[7]. The over-bar denotes an average value.
3) The cylinder gas temperature, T_∞, varies sinusoidally between ambient and a maximum temperature (T_{amb} and T_{max} respectively).
4) The coolant side convection boundary condition is replaced with a constant temperature boundary condition.

[7] In this chapter *convection coefficient* is meant to include the heat transfer due to radiation. A linearized radiation coefficient can be assumed implicit in the coefficient $\overline{h}$. The linearized radiation coefficient is $h_R = \varepsilon\sigma\left(\overline{T}_S^3 + \overline{T}_S\overline{T}_\infty^2 + \overline{T}_S^2\overline{T}_\infty + \overline{T}_\infty^3\right)$ so that $q = h_R\left(T_S - T_\infty\right)$ where ε is emissivity, σ is the Stefan-Boltzmann constant, and over-bars indicate mean values [Beard 1994].

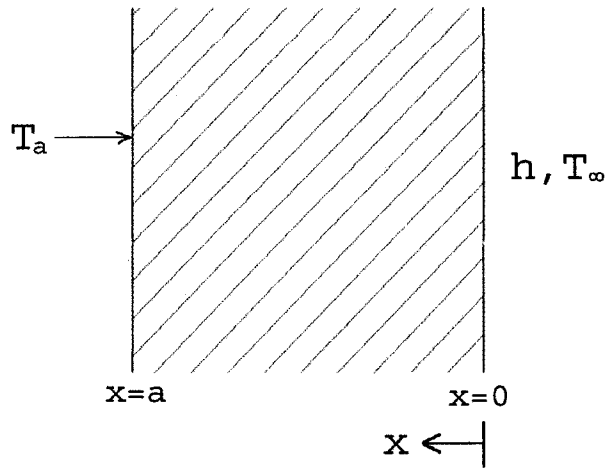

Figure 7.1 – wall section

The governing equation is:

$$\frac{1}{\alpha}\frac{\partial T}{\partial t} = \frac{\partial^2 T}{\partial x^2}$$

with boundary conditions

$$\text{at } x = 0, \quad k\frac{\partial T}{\partial x} = \bar{h}\left(T_{surface} - T_{\infty}\right)$$
$$\text{at } x = a, \quad T(a,t) = T_a$$

where both $T_{surface}$ and T_{∞} vary with time. No initial condition is given because only the fully developed temperature distribution is of interest. This is to say that the work at hand is not concerned with engine warm-up, but rather with steady-state operation. The solution is

$$T(x,t) = \left[\frac{\frac{T_{max} - T_a}{2}}{\frac{k}{\bar{h}\cdot a} + 1}\right]\left(1 - \frac{x}{a}\right) + T_a + T_0 e^{-x\sqrt{\omega/2\alpha}} \sin\left(\omega t - x\sqrt{\omega/2\alpha}\right)$$

where

$$T_0 = \frac{\bar{h}\frac{T_{max}}{2}\sin(\phi)}{k\sqrt{\frac{\omega}{2\alpha}}}, \qquad \phi = \cot^{-1}\left[1+\frac{\bar{h}}{k}\sqrt{\frac{2\alpha}{\omega}}\right],$$

ω, k, and α are the cycle frequency of the engine, the thermal conductivity of the wall material, and thermal diffusivity of the wall material, respectively. The interested reader is referred to appendix C for a detailed presentation of the solution. The solution yields not just the temperature distribution, but also the heat flux and amount of energy transferred. The heat flux is

$$q''_{total} = \frac{-k}{a}\left[\frac{\frac{T_{max}}{2}-T_a}{\frac{k}{\bar{h}\cdot a}+1}\right]+T_0\cdot k\sqrt{\frac{\omega}{\alpha}}\cdot\sin(\tau)$$

where $\tau = \omega t + \pi/4$. Integrating over one complete cycle and separating the result into a steady-state and a time-varying portion, q_{ss} and q_t, respectively, gives the quantity of heat energy transferred:

$$q_{ss} = 2\left(\frac{\pi}{\omega}\right)\frac{k}{a}\left[\frac{\frac{T_{max}}{2}-T_a}{\frac{k}{\bar{h}\cdot a}+1}\right], \qquad q_t = \pm\frac{2k}{\omega}T_0\sqrt{\frac{\omega}{\alpha}}.$$

The steady-state portion, q_{ss}, is the overall or mean heat transfer from the cylinder over a complete cycle. The time varying portion, q_t, sums to zero over a complete cycle,

yet is important as it quantifies the magnitude of energy transfer from the hot, post-combustion gases to the cooler, pre-combustion gases. Thus, the energy available during the power stroke is diminished by both the time dependent heat transfer and a portion of the steady-state heat transfer. The intake and compression stroke must overcome the burden of the addition of the time dependant heat transfer offset by a portion of the steady-state heat transfer. This is illustrated graphically in figure 7.2, below, which shows the steady-state and time varying components of the heat flux ($W/m^2/K$). The overall heat flux curve (not shown) can be arrived at by sliding the transient heat flux curve down to where its start point (at $\kappa = 0$) coincides with the steady-state curve. Any portion of the overall heat flux curve greater than zero would indicate net instantaneous heat flux to the working fluid while portions below zero would indicate instantaneous heat flux from the working fluid to the cylinder walls.

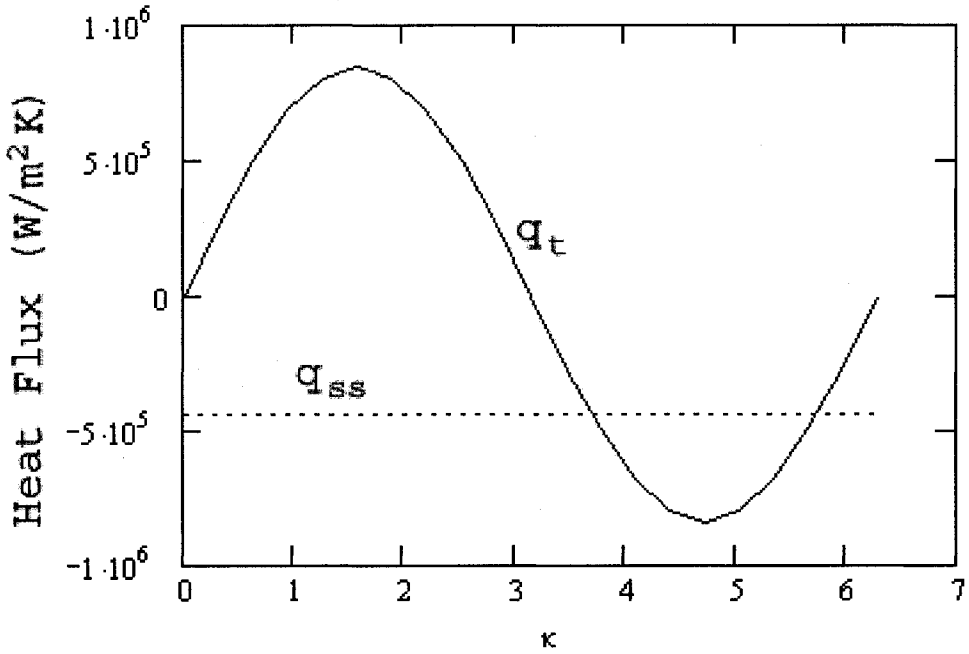

Figure 7.2 – Heat flux throughout the cycle

7.1.1 Simplifications 1 and 2

One-dimensional conduction (simplification 1) and a constant convection coefficient (simplification 2) make for a poor engine model. This is why neither of these simplifications are used in the computational models of chapter 5. However, in this chapter, complex geometries and flow patterns are not considered. Instead, the goal is a generic approach that excludes as many variables as possible. Thus, a flat slab section is taken to represent a small portion of inner cylinder surface. As for the convection coefficient, $\bar{h}$ is set to 625 W/m^2/K. This value was selected so that an aluminum-walled 200cc cylinder at 2500 rpm would have a nominal thermal efficiency of 30%. Figure 7.3 shows the resulting thermal efficiencies of this cylinder as the convection coefficient is varied from 250 to 1250 W/m^2/K.

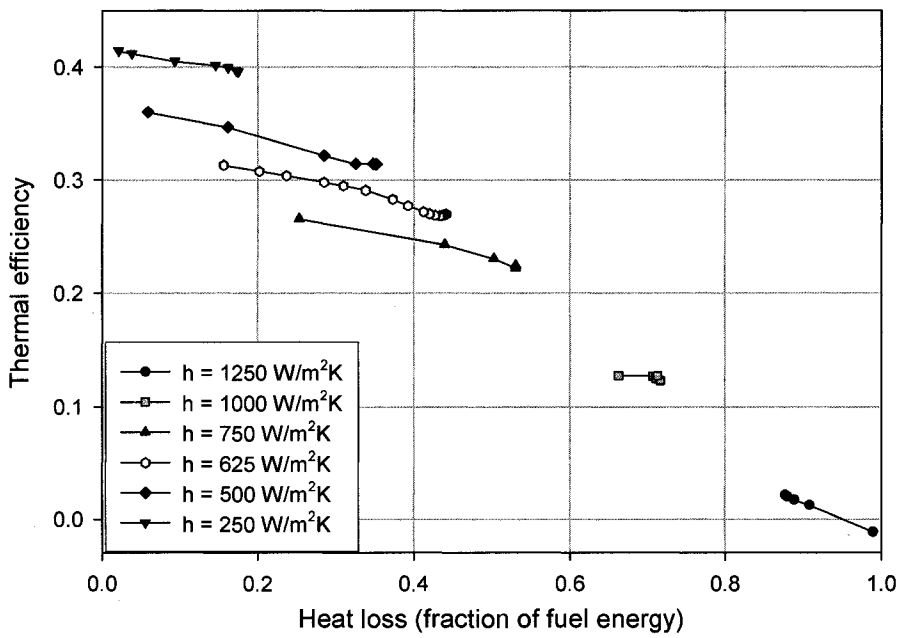

Figure 7.3 -- Thermal efficiency vs. heat loss for a 200 cc cylinder at 2500 rpm with different internal average convection coefficient values

7.1.2 Simplification 3

A sine wave is a rather crude representation of the cylinder gas temperature history. The mean gas temperature history through the 720 degree cycle of a four-stroke engine is typified by a temperature spike coinciding with combustion heat release. The combustion temperature spike is bracketed by ramps preceding and following the spike caused by compression and expansion, respectively. The cylinder gas temperature is then relatively constant (when compared to the power stroke) during the exhaust stroke, after a short blow-down, and relatively constant during the intake stroke. While this profile is mathematically straightforward to write, it is problematic to implement. For example, the heat release profile presented in chapter 5 (figure 5.5) has the Fourier series representation

$$f(x) \sim a_0 + \sum_{n=1}^{\infty} a_n \cos\left(\frac{n\pi x}{L}\right) + \sum_{n=1}^{\infty} b_n \sin\left(\frac{n\pi x}{L}\right)$$

with

$$a_0 = \frac{1}{2L}\left[\frac{m}{2}\xi_2^2 - \frac{m}{2}\xi_1^2 + b\xi_2 - b\xi_1\right],$$

$$a_n = \frac{m}{n\pi}\left[\xi_2 \sin\left(n\pi\xi_2/L\right) - \xi_1 \sin\left(n\pi\xi_1/L\right) + \frac{L}{n\pi}\cos\left(n\pi\xi_2/L\right) - \frac{L}{n\pi}\cos\left(n\pi\xi_1/L\right)\right]$$

$$+ \frac{b}{n\pi}\left[\sin\left(n\pi\xi_2/L\right) - \sin\left(n\pi\xi_1/L\right)\right], \quad \text{and}$$

$$b_n = \frac{mL}{n^2\pi^2}\left[\sin\left(n\pi\xi_2/L\right) - \sin\left(n\pi\xi_1/L\right) - \frac{n\pi\xi_2}{L}\cos\left(n\pi\xi_2/L\right) + \frac{n\pi\xi_1}{L}\cos\left(n\pi\xi_1/L\right)\right]$$

$$- \frac{b}{n\pi}\left[\cos\left(n\pi\xi_2/L\right) - \cos\left(n\pi\xi_1/L\right)\right]$$

where a pulse or ramp section has duration $\xi_2 - \xi_1$ and magnitude ζ_1 at $x = \xi_1$, and ζ_2 at $x = \xi_2$, contained somewhere within the interval (–L, L), and m is the slope of the ramp section (see appendix D).

The number of terms required for fidelity in the Fourier series is commensurate with the resolution required to clearly describe the function. In other words, if the ratio of pulse width to interval is 1/720 then a Fourier series will require on the order of 720 terms. In the example at hand, six ramp sections are needed to represent the heat release curve. Each of the six ramps requires about 500 terms to give the curve good definition. A total of 3,240 terms used in the curve presented in appendix D.

A 3,240 term Fourier series is fair enough when computer generated and used in a computational model, but for an exact solution boundary condition, found the old-school way with paper and pencil, it is decidedly far and away lost in the realm of the unwieldy and absurd. Since, in this case, three or ten terms contribute little more to curve definition than does a single term, a single term is used. Therefore the sinusoidal gas temperature history is more than a crude representation of a real temperature profile; it is the first term of a quite excellent representation of the temperature profile. But putting all smarminess aside, a sinusoidal temperature history suffices to drive the heat transfer mechanism so that the nature of its interdependency with the thermodynamic diesel cycle is observable, if not exact.

7.1.3 Simplification 4

In the simplified heat transfer model, the coolant side wall temperature is fixed (simplification number 4). Examining the depth to which the time-varying part of the

solution penetrates the cylinder wall confirms that this is a suitable simplification. Figure 7.4 shows the depth, in millimeters, at which the magnitude of temperature variations are attenuated to 5% of their surface values. This measure is independent of the gas temperature and mean surface temperature, but is dependent on engine speed. The 5% attenuation depth in aluminum occurs at 4 mm at 1100 rpm and falls to less than 2 mm at 5000 rpm. At the other extreme, zirconium oxide's 5% attenuation depth is 0.45 mm and 0.21 mm at 1100 and 5000 rpm, respectively. Thus, a constant coolant-side temperature is valid for all but the slowest engines with cylinder wall thicknesses less than a few millimeters. More simply put, the simplification poses no problems for the modeling of practical engines.

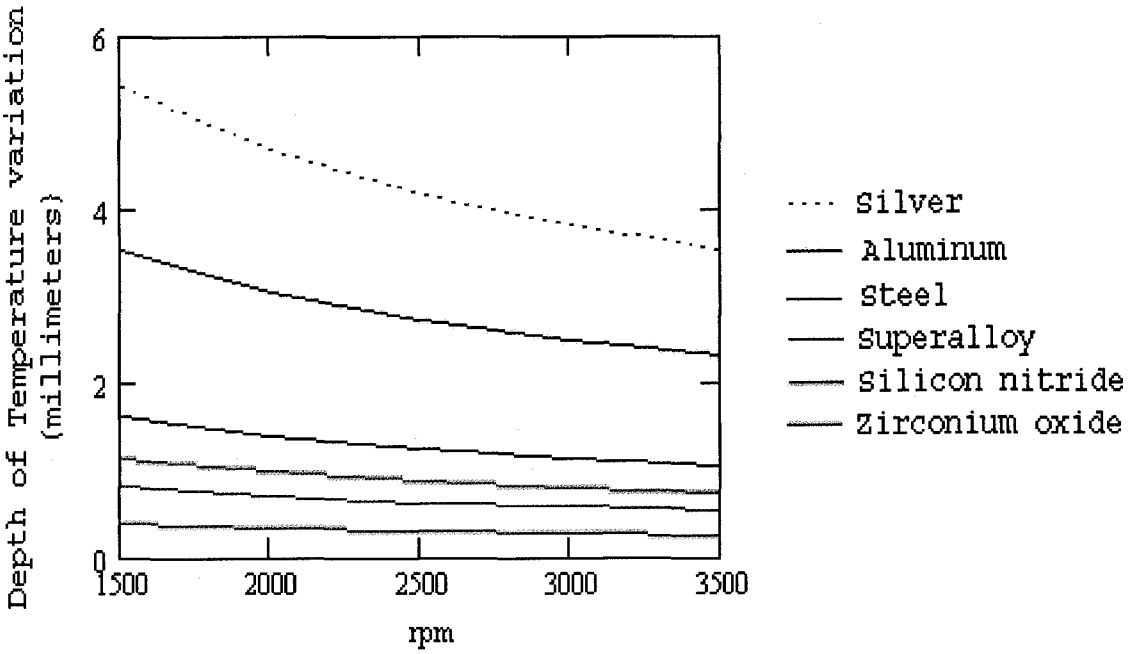

Figure 7.4 – Depth of Temporal Temperature Fluctuations

7.2 Coupling the Heat Transfer Solution to the Diesel Cycle

Four distinct paths comprise the idealized diesel cycle that was coupled to the heat transfer solution: an intake stroke; a compression stroke; a constant pressure combustion process early in the expansion stroke; and the balance of the expansion stroke. The exhaust stroke is neglected. The mean heat loss, q_{ss}, is subtracted from the internal energy of the gas uniformly over the engine cycle. Thus, $\frac{1}{4} q_{ss}$ is subtracted from the intake stroke, $\frac{1}{4} q_{ss}$ is subtracted from the compression stroke, $\frac{1}{4} q_{ss}$ is subtracted from the combined combustion and subsequent expansion stroke, and $\frac{1}{4} q_{ss}$ is neglected with the exhaust stroke. The intra-cycle heat transfer energy, q_t, is added to the internal energy of the gas during the intake stroke and subtracted from the heat of combustion used in that portion of the cycle.

The gas temperature for the heat transfer model is set by adjusting the amplitude of the imposed sinusoidal temperature curve until the maximum temperature coincides with the maximum gas temperature in the diesel cycle to which it is coupled. Changing the amplitude of T_∞ alters q_{ss} and q_t which, in turn, changes the maximum gas temperature achieved in the diesel cycle. Matching T_∞ to the maximum gas temperature in the diesel cycle is an iterative process.

No intake compressor is modeled. Instead, the volumetric efficiency is taken as unity and the heat transfer energy of the intake stroke, $q_t - 0.25 \cdot q_{ss}$, is simply added to the trapped charge to arrive at state 1'. This increases the net cycle work (and thermal

efficiency) compared to more realistic engine models, *e.g.* Wave, as the work required to fill a hot cylinder with the theoretical mass of intake air is neglected.

Expansion and compression in the idealized diesel cycle are polytropic processes due to heat transfer (see Appendix E: Polytropic compression/expansion – a thermodynamics review). Specific heats for air (states 1, 1', and 2) and the products of combustion (states 3 and 4) are allowed to vary so that end states must be found iteratively. This level of finesse is, however, obscured by the overestimation of combustion energy released in the complete, stoichiometric combustion model used.

Using a primitive combustion mechanism leads to unrealistically high gas temperatures, as shown below in figure 7.5 – Peak gas temperature vs. mean surface temperature. However, the goal is not to develop an accurate engine model. Whereas a good engine model is found in Wave, used for the work at hand, and presented in chapter 6; the goal of this chapter is to focus on the effect of heat transfer, especially as it pertains to cycle thermal efficiency as insulation levels are increased, and how material selection does or does not contribute. The effects of phenomena overlooked in the simplifications of this chapter, such as dissociation, flame quenching, and the entropy generation of real compressors, are not overlooked in the Wave simulations. The combined effect of these and other considerations is to limit the efficiency gains from running the engine hotter. In the case of the Lister-Petter test engine, the maximum efficiency point is slightly beyond the level of insulation afforded by the ceramic insulated superalloy components used in the experimental portion of this research (see Chapter 4).

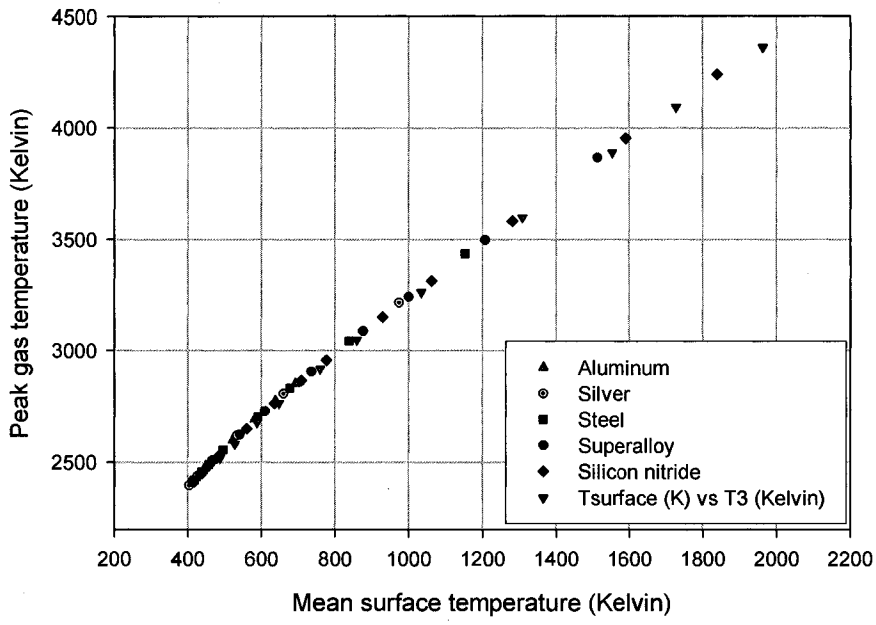

Figure 7.5 -- Peak gas temperature vs. cylinder mean surface temperature (complete stoichiometric combustion without dissociation, 200cc cylinder, 2500 rpm)

7.3 Heat Transfer and Engine Insulation

A result that was suspected from the thermal FEM analysis of the Lister-Petter test engine, and here verified with the exact mathematical solution, is that the magnitude of the intra-cycle heat transfer is fairly independent of material choice. In fact, neither the intra-cycle heat transfer nor the overall heat loss is much affected by material selection. The overall heat loss does depend on the total thermal resistance of the cylinder wall, but it makes little difference if the cylinder wall is a thick slab of aluminum or a thin slab of zirconium oxide – if the total thermal resistance is the same then so will be the surface temperature and heat transfer. Figure 7.6 shows both the intra-cycle heat transfer and the overall cylinder heat loss as a function of surface temperature.

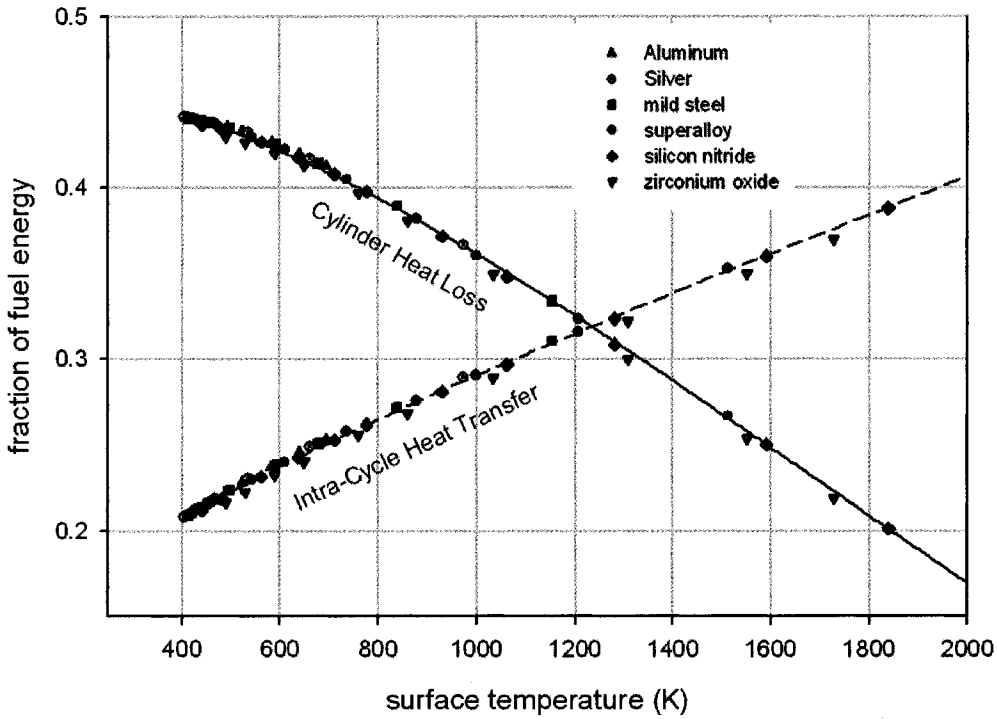

Figure 7.6 -- cylinder heat transfer *versus* surface temperature
200cc cylinder w/internal h = 625 W/m^2/K, 2500 rpm

When using FEA to find the surface temperatures of the test pistons it was noticed that the fully developed surface temperatures varied by only a few degrees throughout the cycle. This was true for both the solid aluminum piston, where $T_{max} - T_{min} = 4K$, and the ceramic insulated superalloy piston, where $T_{max} - T_{min} = 9K$. The exact solution to the heat transfer problem allows for examination of the surface temperature fluctuations. The results of this examination are plotted below in figure 7.7. All the metals, including superalloy, have temperature variations less than 20 Kelvin until the mean surface temperature exceeds 800 Kelvin. The two ceramics shown, silicon nitride and zirconium

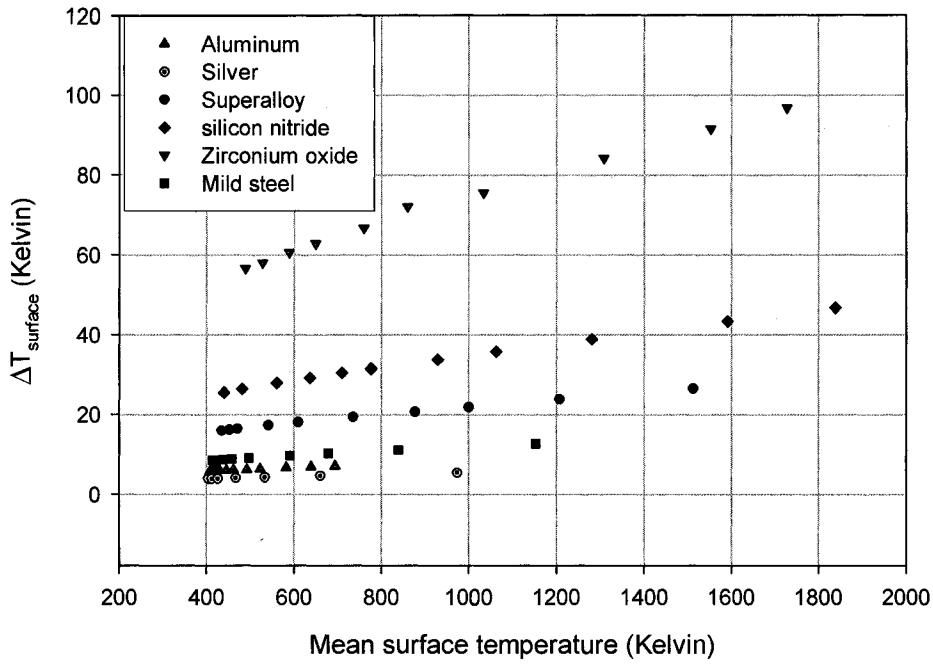

Figure 7.7 -- variation of surface temperature during a cycle versus mean surface temperature.

oxide, have temperature fluctuations of 32 K and 75 K, respectively, at mean surface temperatures of 800 K. While a 75 or even a 32 Kelvin temperature swing at first sounds non-trivial, it should be kept in mind that, for an 800 K surface temperature, the gas temperature swings from the intake temperature of 300 K to a peak temperature of 3000 K (refer back to figure 7.5). Thus, at a mean surface temperature of 800 K the surface temperature variation is 75/2700 as great (a little less than 3%) as the gas temperature variation during the cycle. Also, though the surface temperatures used in the calculations and graphs of this chapter extend up to and sometimes beyond the represented material's working limits, it should be noted that a mean surface temperature of 800 K is something of an extreme. For example, while the center of the ceramic insulated superalloy test piston at full load and 3000 rpm achieved a temperature of 1110 K, the top edge of the

piston was significantly cooler at 730 K, and the steel cylinder walls and aluminum cylinder head were cooler still with temperatures that ranged from 400 to 500 K for an average cylinder surface temperature in the neighborhood of 600 K.

The thermal efficiency of the idealized diesel cycle versus the heat loss is plotted in figure 7.8. The initial drop in thermal efficiency as the overall heat loss decreases in the figure is due to the greater incremental increase in the intra-cycle heat transfer relative to the overall heat loss. This can also be seen as the steep initial slope of the intra-cycle heat transfer versus the overall heat loss plotted in figure 7.9. In the simplified model at high heat loss, the compression work saved by cooling the trapped gas during intake and compression more than compensates for the heat loss deducted from the heat release in the power stroke. At the other end of the heat loss spectrum of figure 7.8, the efficiency continues to increase commensurate with insulation levels. But here the simplified model neglects some of the higher temperature effects and assumes some implausible gas temperatures (recall figure 7.5). Also, it is worth mentioning again that the simplified model of this chapter exacts no penalty for maintaining volumetric efficiency at unity no matter what the insulation levels or surface temperatures. Whether or not the simplified model's prediction of an increase in thermal efficiency when strenuous cooling measures are implemented (high heat loss in figure 7.8), and of an increase in thermal efficiency as heat loss diminishes toward adiabaticity (low heat loss in figure 7.8) are erroneous can be determined either by experimentation or by using a more refined model. Both the experimental portion and the Wave modeling portion of this work show that the simplified model is indeed a poor predictor of engine performance. However, it does

afford the opportunity to examine the heat transfer relationships at the temperature extremes.

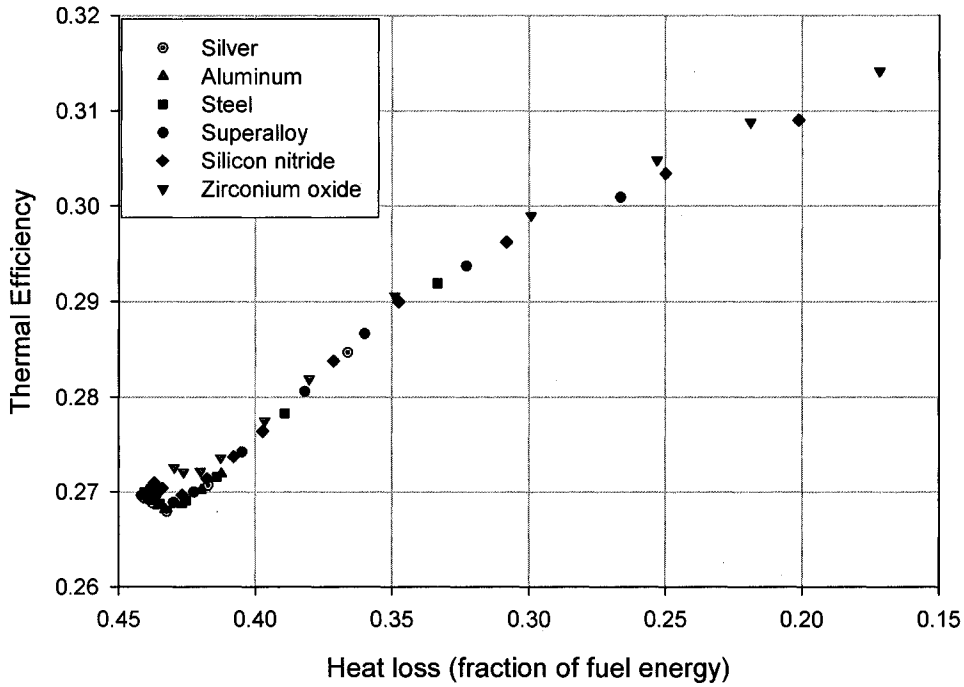

Figure 7.8 -- thermal efficiency vs. overall heat loss
200cc cylinder, internal h = 625 W/m^2/K, 2500 rpm

Figure 7.9 shows the magnitude of the intra-cycle heat transfer as the cylinder's thermal resistance increases. Only minor differences are apparent in the heat transfer response of the different materials. There are two salient reasons for the nearly identical thermal responses of materials with such widely different thermal properties. First, the gas heat transfer is coupled to the cylinder wall heat transfer by the wall's surface temperature, $T_{surface}$. It makes no difference whether a particular surface temperature is achieved by a thin, conductive wall backed by hot cooling fluid or if it is achieved through a thick, insulative material backed by cold cooling fluid. Second, the influence

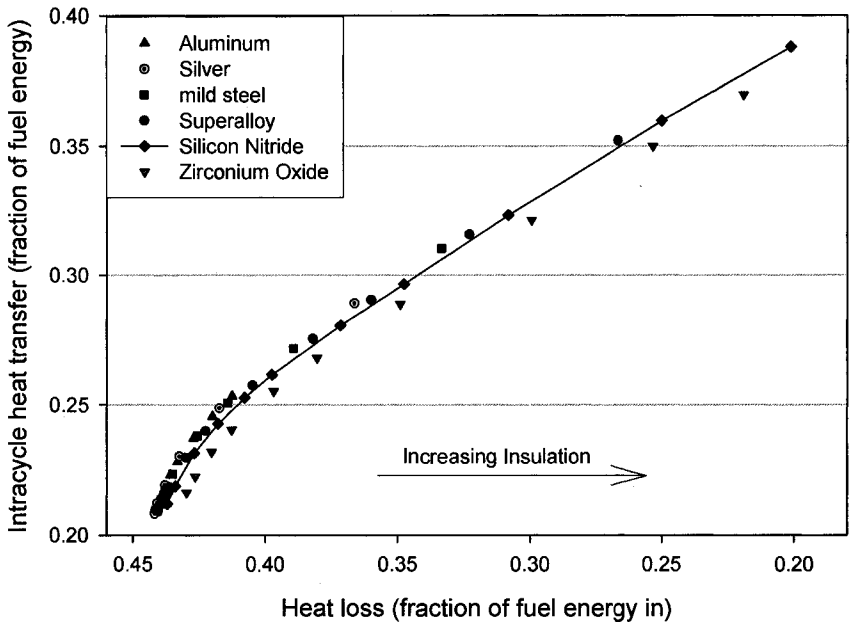

Figure 7.9 -- Intracycle heat transfer vs heat loss
200cc cylinder w/internal h = 625 W/m^2/K, 2500 rpm

of different thermal diffusivities are not afforded sufficient time to manifest. There are two orders of magnitude difference in the cycle time of a reciprocating engine and the thermal time constants of the materials. Even zirconium oxide, the material with the lowest conductivity and diffusivity, achieves an order of magnitude in difference between its thermal time constant and the engines cycle time by 1,000 rpm. Figures 7.10.a and 7.10b illustrate this.

Figures 7.10a and 7.10b both plot the ratio of material time constant to engine cycle time. Figure 7.10a shows all five materials considered in the exact solution from zero to 10,000 rpm. Figure 7.10b is a close-up of the low speed (up to 1000 rpm) section of figure 7.10a. The thermal time constant for the cylinder material is taken to be $\tau_{th} = \rho Cl / \bar{h}$, where ρ, C, l, and $\bar{h}$ are density, specific heat, depth into material

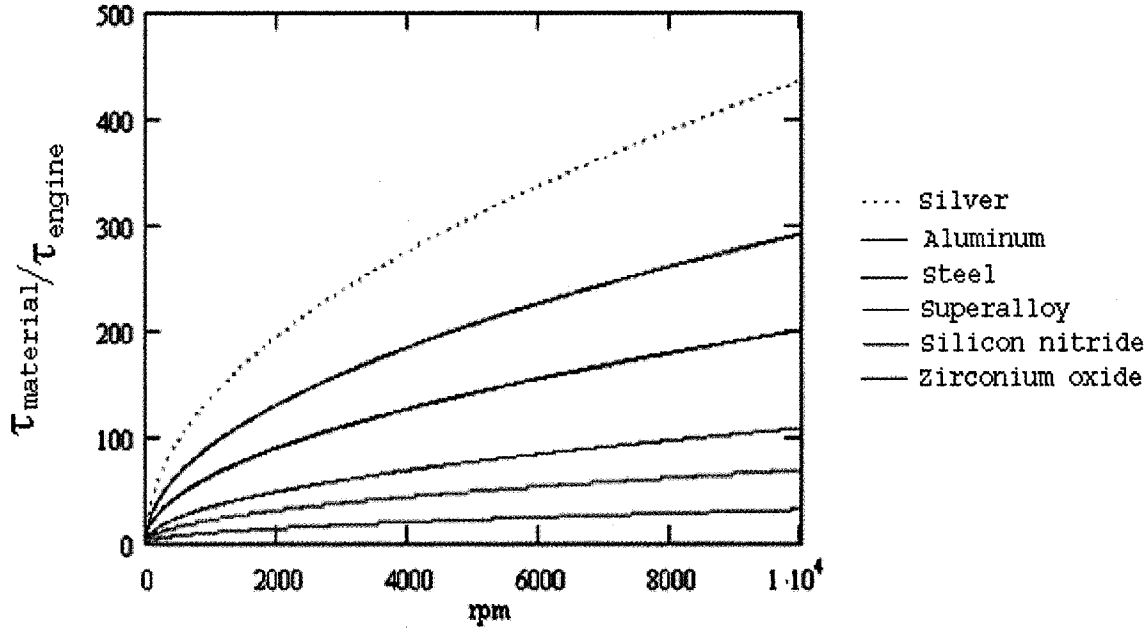

Figure 7.10a – Ratio of Material to Engine Time Constant *vs* Engine Speed to 10,000 rpm

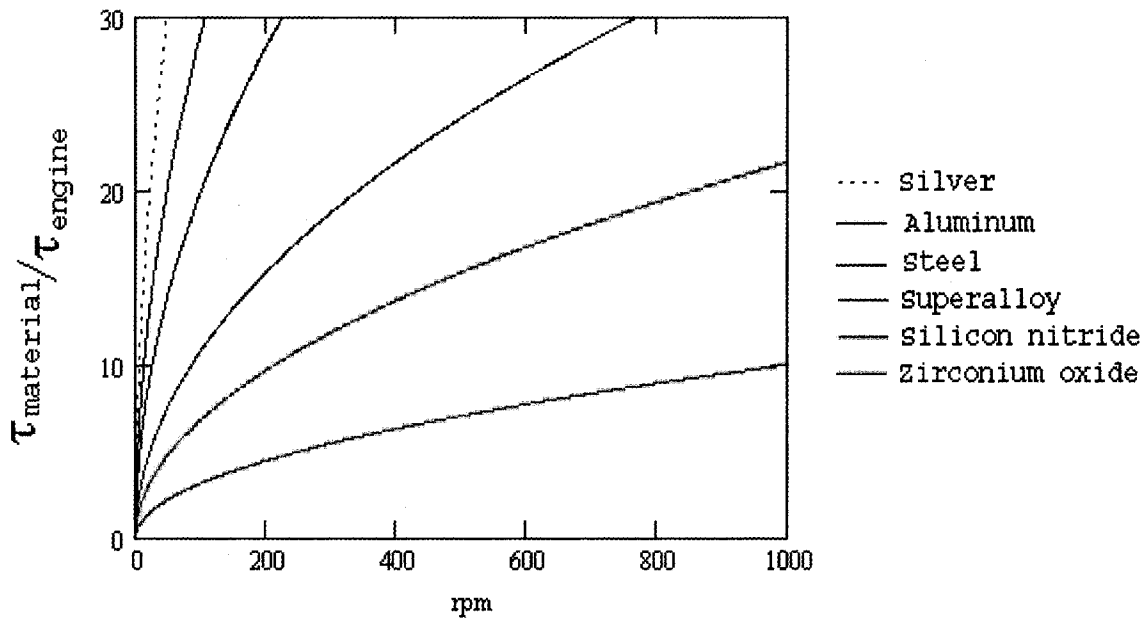

Figure 7.10b – Ratio of Material to Engine Time Constant *vs* Engine Speed to 1,000 rpm

where the magnitude of temporal temperature variation is attenuated to 5% of the surface value, and the convection coefficient, respectively. The engine cycle time, τ_{engine}, is simply $120/rpm$ because

$$\tau_{engine} = \frac{1}{\frac{revolution}{minute} * \frac{1\ minute}{60\ seconds} * \frac{1\ cycle}{2\ revolutions}} = \frac{120}{rpm}\left(\frac{seconds}{cycle}\right).$$

Of course, one could run an engine very slowly so that τ_{engine} is comparable to τ_{th}, say, a ZrO_2 engine at 10 rpm, or a superalloy engine at ⅞ of an rpm, or an aluminum engine at 8 revolutions per hour. But if one sticks to design conventions, then slow engines are big engines, and the bigger an engine is, the less important wall effects (such as heat transfer) become. Given that mean maximum piston speeds are typically 8 to 15 m/s [Heywood, 1988, p.45], with larger engines at the lower end of the range, an engine designed to run at 1000 rpm would have eleven litres of displacement, assuming bore equals stroke. An engine designed for a maximum speed of 100 rpm would have a displacement on the order of 11 m^3. This puts the 10 rpm engine far and away beyond the size where wall effects, including those due to material thermal properties, exert much influence. Figure 7.11 illustrates this, though to be fair the results are from a constant engine speed of 2000 rpm and not the 1000 rpm of the example just given. In figure 7.11 $\bar{h}$ is held at 625 $W/m^2/K$. Three thermal resistances of the cylinder wall are plotted, all corresponding to a nominal 2 cm thickness of aluminum, superalloy, and zirconium oxide with resistances of 10^{-4}, 10^{-3}, and 10^{-2} m^2K/W, respectively.

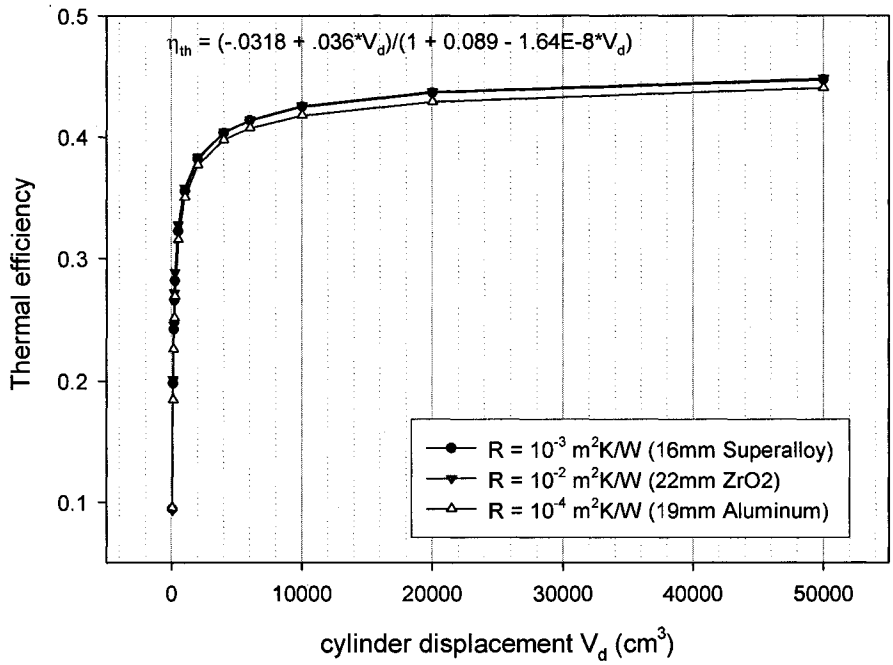

Figure 7.11 -- Thermal efficiency vs. cylinder volume
Convection coefficient and other parameters held constant as described in text

CHAPTER 8

CONCLUSIONS AND FURTHER WORK

Three themes emerged in the course of this work. The first, that thermodynamically the choice of material doesn't matter, was not evident *a priori*. The second theme is that the increase in temperature accompanying increased insulation levels causes an increase in intra-cycle heat transfer which, at high levels of insulation, cannot be satisfactorily mitigated. This is more apparent than the first theme, falling out upon reflection and verified with more rigorous analytic methods in chapter 7. In fact, the intra-cycle heat transfer, which has a magnitude and effect on engine performance commensurate with an engine's operating temperature, is a phenomenon that manifests and is identified in all segments of this work – the experimental, the computational, and the exact solution to heat transfer. The third, that the implementation of a low heat rejection strategy can yield benefit, was more than a preformed assumption; it was one of the motivating ideas for this work, though it was not anticipated that the gains would be so modest. These themes are more fully summarized in the balance of this chapter.

8.1 Material Choice is Immaterial

At least in the thermodynamic sense, and providing that a material's working temperature limit is not exceeded, the choice of materials matters not. This is not to say

that an engine can be made of mashed potatoes. Structural and durability concerns are important primary considerations in engine material selection. So too are material mass, cost, machinability, availability, and a host of other considerations. And in the thermodynamic sense a material's thermal properties matter quite significantly so that one material cannot be capriciously or arbitrarily substituted for another. But at a given level of engine heat loss there is an associated surface temperature that is nearly invariant with respect to material properties. And a given level of engine heat loss depends on the net thermal conductivity, not the specific conductivity[8].

8.1.1 Thermal Response Time

Engine cycle times are simply too short for differences in the thermal response times of materials as disparate as silver and zirconium oxide to have much effect. Though the argument that supports this conclusion is presented in section 7.3, another example is given here *gratia*. At 500 and 5,000 rpm, an engine's cycle time is 0.24 and 0.024 seconds, respectively. With a convection coefficient of 1000 $W/m^2/K$ the thermal time constant of silver is 23 and 7 seconds at 500 and 5,000 rpm, respectively. The thermal time constant of zirconium oxide is 2 seconds at 500 rpm and ½ seconds at 5,000 rpm. For quick reference the reader is reminded that, for a material in thermal equilibrium, a sudden and sustained change in surface temperature will require a span of time equal to the thermal time constant for the material to reach 63% (or $1-e^{-1}$) of its new equilibrium.

[8]Heat transfer also depends on the coolant-side conditions and internal flow conditions, but these are not material properties.

The physical manifestation of the ratio of engine cycle time to material response time is the surface temperature variation throughout the cycle. Because of the imbalance between engine and material time frames, the temperature variation is small. Silver, with a thermal conductivity of 412 W/m/K at 600 Kelvin and HAYNES 230 superalloy with a conductivity of 20 W/m/K at 600 Kelvin represent the extremes in conductivities for metals. Yet, at a mean surface temperature of 600 K (and a T_∞ that varies from 300 to 2650 K with $\bar{h}$ =625 W/m^2/K at an engine speed of 2500 rpm), the magnitude of the temperature variation is but 4.5 K for elemental silver and 18 K for HAYNES 230 superalloy. The two ceramics considered in this work have low conductivities, $k = 11$ for Si_3N_4 and $k = 2$ for ZrO_2 at 600 K, and, under the conditions given, have temperature variations of 29 K and 60 K (see figure 7.7).

8.1.2 Engine Heat Loss is a Function of Aggregate Thermal Resistance

While the temporal variation in surface temperature varies by an order of magnitude from the most thermally diffusive metal to the least thermally diffusive ceramic, the mean surface temperature varies essentially not at all[9]. And while different heat capacitances of different materials will certainly affect transiency times from load or speed changes, or on start-up, the mean temperature at equilibrium will not change from material to material for a given local heat flux. Once thermal equilibrium has been established the mean surface temperature depends on the aggregate thermal resistive

[9] A small difference in cyclic surface temperature variation betwixt materials affects a small difference in intra-cycle heat transfer which slightly alters the peak gas temperature in the simplified model and, in turn, results in a small change in the mean surface temperature.

value of the cylinder wall and its boundary conditions, not on the cylinder material or its thermal properties *per se*. It can not be otherwise.

8.2 The Wages of Insulation is Intra-Cycle Heat Transfer

There is no way to satisfactorily limit the effects of the intra-cycle heat transfer at higher insulation levels. Not even with clever selection of materials can this bullet be dodged. Like a regenerator in a Stirling engine, in the diesel engine the cylinder material absorbs energy from the hot side of the cycle and dumps it into the cool side. In the adiabatic ideal of a Carnot engine there is no unwanted heat transfer to or from the cylinder – the cylinder walls magically mirror the adjacent gas temperature sans energy exchange. In any real engine, the inner cylinder surface temperature remains fairly constant and depends on the cyclic gas temperature, the heat transfer coefficient, and the thermal resistance of the cylinder material (and/or the coolant side surface temperature). The following expressions are synonymous in that they achieve the same result: increasing the mean surface temperature, increasing the coolant temperature, increasing the cylinder insulation, and decreasing the overall heat loss. Raising the surface temperature (decreasing overall heat loss) will reduce the energy lost from the hot side of the cycle, but will add a like amount of energy to the cool side.

In the naturally aspirated test engine, the intra-cycle heat transfer is responsible for a decrease in the maximum achieved volumetric efficiency from 0.95 in the aluminum engine to 0.87 in the superalloy engine (figures 4.6 and 4.7, section 4.3). For the compressor and turbine fitted and optimized engines modeled in chapter 6, the point of

diminishing returns occurs when overall heat loss is decreased below 70% of the conventionally cooled engine's (figure 6.2, section 6.2). In the model of chapter 7, the volumetric efficiency was simply set by fiat at unity. In the more realistic model of chapters 5 and 6 and in real engines, maintaining mass flow in the face of increasing engine temperatures requires equipment that adds its own energy load to the system.

8.3 There is a Benefit to Implementing a Low Heat Rejection Strategy

Insulating the combustion chamber can afford gains in thermal efficiency. However, both insulating a naturally aspirated engine and fitting a turbine on the exhaust without a compressor on the intake decreases net work. Therefore, to realize gains, judicious levels of insulation must be accompanied by both exhaust energy scavenging and intake pressure boost. Even then, the gains may be marginal. For the Lister-Petter engine modeled, the maximum gain was a 4% increase in net work, which translates to a 1% increase in thermal efficiency. There were some complications that undoubtedly diminished the performance of the test engine (and thereby the model that was calibrated to the experiment). The complications encountered in this work include intake charge heating, high piston mass and elevated temperatures causing sub-optimal operation and eventual failure of the fuel injector and exhaust valve.

8.4 Suggestions for Further Work

Today's superalloys with ceramic backing are capable of supporting cylinder/combustion surface temperatures over 1100 °C. In the experiment the peak

piston surface temperature exceeded 1100 K (827 °C). However, this level of insulation may be unnecessary and even undesirable. The test engine in the LHRE configuration has a ceramic insulated superalloy piston and a superalloy segment of cylinder wall. The balance of the cylinder is the stock components (i.e. aluminum head and steel cylinder walls with cooling fins). This level of insulation yielded a reduction in heat loss close to the optimal level (~30%) predicted by the Wave the model (section 6.2). While the level of insulation was near optimal, the insulation distribution was not. While the insulated piston supported an average surface temperature of ~900 K, the stock cylinder walls and head were between 400 and 500 K (see section 7.3). Decreasing the piston's thermal resistance and increasing the thermal resistance of the cylinder head and wall so that the inner cylinder surface is more uniform near 600 K should provide the same reduction in overall heat loss while attenuating the contribution to intra-cycle heat transfer that comes from a very hot piston surface. This would also allow a simpler piston assembly thereby addressing the piston mass problem encountered in this work.

A prototype LHRE is the next step. While the test engine used in the experimental portion of this work is adequate for retrofitting a component or two for concept validation, component testing, and to project the outcome of further modifications, a viable LHRE prototype requires more extensive modification than is practical with a 1968 Lister-Petter AA1 engine.

In the test engine, at slower engine speeds and lower peak temperatures, the friction-compensated torque of the superalloy fitted engine is comparable to the aluminum engine. At higher speeds and temperatures, the superalloy engine suffers a

decrease in brake torque relative to the aluminum engine. There are a number of explanations for this: the fuel injector in the test engine was found to be sticking; the exhaust valve stuck in its guide on several occasions and had to be freed, cleaned, and lapped into the seat; the injector and combustion chamber of the test engine were not designed for elevated temperatures. Some of the underdevelopment of torque in the superalloy engine is due to poor combustion (timing, rate, and degree of completion) and some is due to intake charge heating reducing η_v. Seven items have been identified that need to be addressed in the design of a prototype LHRE. They are, in order of importance:

1) The fuel injector must be protected from excessive heat gain or designed to function at the elevated temperatures encountered.

2) The exhaust valve guide and valve stem must either be isolated from excessive temperatures, or cooled to the working temperature of the lubricant.

3) The exhaust valve should be of superalloy material in order to extend its working temperature range.

4) The intake port should be insulated or separated from the exhaust port to reduce heat gain from the exhaust port and cylinder head.

5) The piston should be redesigned to reduce mass. As in the experimental piston, the design should incorporate a superalloy flame surface with ceramic backing and

an aluminum base. The design should also maintain the ring set-back strategy introduced in previous work by Mohamed Elshindidy [Elshindidy 1996].

6) The fuel injector and combustion chamber contours should be brought up to date and designed to accommodate elevated gas temperatures.

7) The combustion chamber should also accommodate a pressure transducer to facilitate further research.

Last is this note on the endurance of the superalloy specimen. The ceramic-insulated superalloy piston top used in the experimental portion of this work was developed at Colorado State University by Mohamed Elshindidy [Elshindidy, 1996]. After several initial failures, Elshindidy put forth the present design which survived his endurance test of 1001 hours engine time at 3000 rpm with a working temperature of 1033 K (1400 °F). Though a strict time log was not kept in this work, it is estimated that the superalloy piston has endured an additional 300 hours of engine time at speeds ranging from 1500 to 3000 rpm and temperatures up to 1110 K (1538 °F).

BIBLIOGRAPHY

Amman, Charles A. (1990). The automotive engine: future technology. *Automotive Engineering, 98, n.1*, 35-40.

Arunachalam, M., Gopalakrishnan, K. V., Rao, P.S. (1989, November). Performance of a diesel engine with thermally insulated combustion chamber. *IE Journal, 70*, 52-55.

Attia, M. H., Cameron, A., Kops, L. (2002, February). Distortion in thermal field around inserted thermocouples in experimental interfacial studies, part 4: End Effect. *Journal of Manufacturing Science and Engineering, 124*, 135.

Badgley, P., *et al.* (1990). *NATO durability test of an adiabatic truck engine*. SAE Paper 900621 presented at the International Congress and Expo, Detroit, MI.

Bartz, W. J. (1994). Engine oils and automotive lubrication. *Mechanical Engineering Handbook of Turbomachinery, 93*, 80.

Bass, John C., Elsner, Norbert B., & Leavitt, F.A. (1994, 30 Aug. - 1 Sep.). *Performance of the 1 kW thermoelectric generator for diesel engines*. Presented at the 13th International Conference on Thermoelectrics, 1994, Kansas City, MO.

Bass, John C., Kushch, Aleksandr S., & Elsner, Norbert B. (2001, February). *Thermoelectric generator (TEG) for heavy diesel trucks*. Presented at the Space Technology & Applications International Forum, Albuquerque, NM.

Beard, Joseph G. (1994). *Technical and economic performance of site built solar air heaters*. Master's thesis, University of Nevada Reno, Reno, NV.

Bishop, J. N. (1964). *Effects of design variables on friction and economy*. SAE paper 812A.

Bryzik, W., Kamo, R.(1983). *TACOM/Cumins adiabatic engine program*. SAE paper 830314.

Buckley, I. M. (1986, March 6). *An overview of ceramic applications in engines*. Motorship 8th International Marinew Propulsion Conference, London.

Burns, G. W. *et al.* (1993, April). *Temperature-electromotive force reference functions and tables for the letter-designated thermocouple types based on the ITS-90.* National Institute of Standards and Technology Monograph 175. Washington, DC: U.S. Government Printing Office.

Çengel, Yunus A., & Boles, Michael A. (1989). *Thermodynamics: an engineering approach.* McGraw-Hill Inc New York, NY.

Department of Energy. (2000, May 5). *Cooperative research and development for natural gas reciprocating engines.* Solicitation for Financial Assistance Applications #DE-SC02-00CH11029.

Dhinagar, S. Jabez, *et al.* (1993). *Spark assisted diesel operation in a low compression ratio low heat rejection engine.* SAE paper 920545.

Dhinagar, S. Jabez, *et al.* (1993). *Experimental investigations on the combustion of ethanol in an LHRE using different methods.* SAE paper 930931.

Elshindidy, Mohamed (1996). *Life limiting properties of a superalloy in a low heat rejection engine.* Doctoral dissertation, Colorado State University, Fort Collins, CO.

Fourier, Jean Baptiste Joseph (1830). *Analyse des équations déterminées.* Library of Congress control number 46440903.

Freese, V. C. E., Hinkle, S. J., Avery, T. A. (1993). Development of the Detroit diesel 440 bhp 8V-71T LHRE for the FAASV and M109 Paladin vehicles. *SAE Transactions, 102, n. 3,* 1576.

GE Transportation Systems. (1994, January). *Coal-fueled diesel: technology development.* Author.

Gerpen, Jon Van (1988, August). *Documentation of the Benson diesel engine simulation program.* NASA Technical Memorandum 100940.

Haberman, Richard (1987), *Elementary applied partial differential equations, 2nd edition.* Prentice-Hall, Englewood Cliffs, New Jersey.

Hanamura, Katsunori & Nishio, Satoshi (2003, November). A feasibility study of reciprocating-flow super-adiabatic combustion engine. *Japan Society of Mechanical Engineers International Journal, Series B: Fluids and Thermal Engineering, 46, n 4,* 579-585.

Heinrich, H., Langer, M., Walzer, Peter (1986, April). Ceramic components in passenger car diesel engines. *SAMPE Quarterly, 17, no. 3*, 32-39.

Herivel, John (1972). *Joseph Fourier: the man and the physicist*. Clarendon Press, Oxford.

Heywood, John B. (1988). *Internal combustion engine fundamentals*. McGraw-Hill, New York, NY.

Hou, Shuhn-Shyurng (2004, November). Heat transfer effects on the performance of an air standard Dual cycle. *Energy Conversion and Management, 45, n 18-19*, 3003-3015.

Incropera, Frank P., & DeWitt, David P. (1990). *Introduction to heat transfer, 2ed.* John Wiley and Sons, Inc., New York, NY.

Kamo, R., & Bryzik, W. (1982). *Cummins/TARADCOM adiabatic turbocompound engine program*. SAE paper 810070.

Kamo, R., & Bryzik, W. (1985). *Cummins/TACOM advanced adiabatic engine*. SAE paper 840428.

Kawamura, Hideo & Akama, Mitsuru (2003). Development of an adiabatic engine-installed energy recover turbines and converters of CNG fuel. *S.A.E. transactions.*
112, Part 4, 2007-2014.

Kawamura, H. *et al.*(1996). Combustion and combustion chamber for a low heat rejection engine. *SAE Transactions, 105, n. 3*, 606-614.

Klova, Robert J., & Subaru, Constantin S. (1993). *Upgrading a power turbine stator for greater creep life, incorporating a material change to HAYNES 230*. ASME paper 93-GT-271.

Kobori, Shigeharu, *et. al.* (1992). Combustion in low heat rejection diesel engines. *Japanese Society of Mech. Eng. International Journal Series 2, 35, no.1*, 1-9.

Krishnamoorthy, R. (1980, March). Reducing the friction losses of an adiabatic engine with three types of pistons. *Indian Journal of Technology, 27*, 140-144.

Kvernes, Ingard, (1986). *In-service performance of ceramic and metallic coatings in diesel engines*. SAE paper 86088.

Nakatani, S., Yoshizu, K., Mitsunaga, T., Inoshita, Akira (1987) *Development of an all ceramic swirl chamber for diesel particulate control.* SAE paper 861406.

Nazar, J., *et al.* (1997, February). *Naturally aspirated LHR single cylinder extended expansion CI engine.* SAE International Congress, Detroit MI.

Parker, Alec (1990, January). Ceramic applications in reciprocating engines. *Metals and Materials, 6, n.1,* 14-20.

Parlak, Adnan (2005, January). The effect of heat transfer on performance of the diesel cycle and exergy of the exhaust gas stream in a LHR diesel engine at the optimum injection timing. *Energy Conversion and Management, 46, n.2,* 167-179

Pool, Robert (1989, October). Synthesizing oils is a slippery job. *Science, 246,* 444.

Potter, R., Hutcherson, G., Willson, Bryan (1997). *Comparative testing of ignition sources for large-bore natural gas engines.* PCRC Gas Machinery Conference.

Prasad, R., Samria, N. K. (1989). Investigation of heat transfer in an oil cooled piston with and w/out ceramic insulation on crown face. *International J. Mechanical Science., 31, n. 10,* 765-777.

Puzinauskas, Paulis V., Willson, Bryan D., Evans, Kirk H. (2000). *Optimization of natural gas combustion in spark-ignited engines through manipulation of intake-flow configuration.* SAE paper 2000-01-1948, Fuels & Lubrication conference, Paris.

Rakopoulos, C. D., Giakoumis, E.G. (2005, August). The influence of cylinder wall temperature profile on the second-law diesel engine transient response. *Applied Thermal Engineering, v 25, n 11-12,* 1779-1795.

Rakopoulos, C. D., & Mavropoulos, G. C. (1998, May). Components heat transfer studies in a LHR DI diesel engine using a hybrid thermostructural finite element Model. *Applied Thermal Engineering, 18, n. 5,* 301.

Sanders, J. C., & Schramm, W.B., (1948, January 15). *Analysis of variation of piston temperature with piston dimensions and undercrown cooling.* Flight Propulsion Research Laboratory, National Advisory Committee for Aeronautics, report No. 895, Cleveland, Ohio.

Shimauchi, Tomoki, *et al.* (1984, March). *Tribology at high temperature for uncooled heat insulated engine.* SAE Paper 840429, International Congress & Exposition, Detroit MI.

Sliney, Harold E., & Grisaaffe, Salvatore J. (1987, May). Heat's on to develop high temperature materials: solid lubricants for hot engines. *Aerospace America, 25*, 16.

Stamper, Eugene, & Richard Koral (1979). *Handbook of air conditioning, heating, and ventilation.* Industrial Press Inc., 200 Madison Ave, New York, NY 10016.

Stearns, Carl A. (1987, May). Heats on to develop high temperature materials: thermal barrier coatings. *Aerospace America, 25*, 27.

Stephens, Joseph R. (1987, May). Heats on to develop high temperature materials: advanced metallic for power and propulsion systems. *Aerospace America, 25*, 31.

Sun, X., *et al.*, (1993). Experimental analysis and performance improvement of a single cylinder direct injection turbocharged LHRE. *SAE Transactions, 102, n. 3*, 1503.

Tamilporai, P., Baluswamy, N., Jawahar, P. M., Subramaniyam, S., Chandrasekaran, S., Vijayan, K., Jaichandar, S., Rani, J. J., Arunachalam, K. (2003). Simulation and Analysis of Combustion and Heat Transfer in Low-Heat-Rejection Diesel Engine Using Two-Zone Combustion Model and Different Heat Transfer Models. *S.A.E. transactions. 112, Part 6*, 1185-1203.

Taymaz, Imdat (2006, February). An experimental study of energy balance in low heat rejection diesel engine. *Energy, 31, n.2*, 364-371.

Thring, R. H., (1987). *Low Heat Rejection Engines.* SAE paper 860314.

Whitehouse, N.D., & Way, R. J. B. (1971, January). *Simple method for the calculation of heat release rates in diesel engines based on the fuel injection rate.* SAE Paper 710134.

Willson, Bryan D., Hutcherson, G., Hawley, S., Willet, K. (1998). *Relative performance of high-pressure fuel gas delivery on large-bore, two-stroke natural gas engines.* Private collection of Bryan Willson.

Winkler, Matthew F., & Parker, Daniel W. (1992). Greener, meaner diesels sport thermal barrier coatings. *Advanced Materials & Processes, 5.*

Woods, M., Bryzik, W., Schwarz, E. (1992). *Heat rejection from high output adiabatic diesel engines.* SAE paper 920541.

Zhou, Shichao (1995). *Studies of a low heat rejection engine designed with conventional lubrication.* Dissertation, Colorado State University, Fort Collins, CO..

Zucchetto, J., Myers, P., Johnson, J., Miller, D. (1988, May). An assessment of the performance and requirements for adiabatic engines. *Material Science, 240, n.27*, 1157-1162.

APPENDIX A
THERMAL EFFICIENCY OF THE DIESEL CYCLE

Thermal Efficiency of the Ideal Diesel Cycle

The figure below depicts a pressure-volume curve for the ideal Diesel cycle. To enhance readability, the compression ratio has been set to 12 and no attempt has been made to match to q_{in} with practical levels of heat addition.

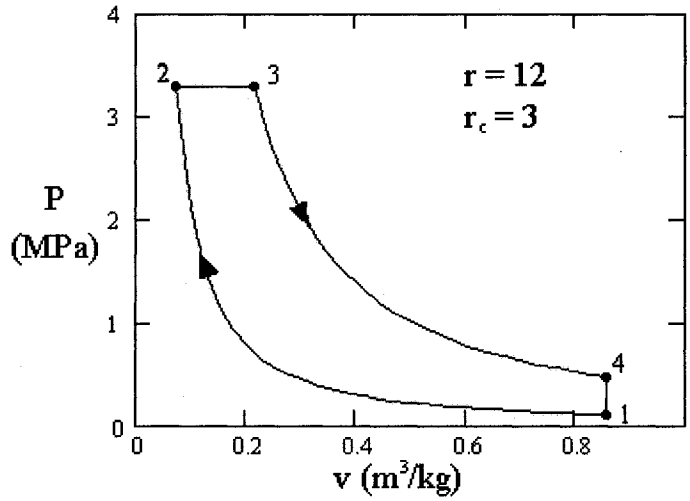

Figure A.1 – Ideal Diesel Cycle P-v Diagram

The net work, expressed in terms of heat transfer, is the difference between heat input and heat output. That is, $w_{out} = q_{in} - q_{out}$. The thermal efficiency can then be written

$$\eta_{TH} = \frac{w_{out}}{q_{in}} = \frac{q_{in} - q_{out}}{q_{in}} = 1 - \frac{q_{out}}{q_{in}}.$$

Heat addition from state 2 to state 3, taking place at constant pressure, is described by $q_{in} = C_p(T_3 - T_2)$. Heat rejection from state 4 to state 1, taking place at constant volume, is described by $q_{out} = C_v(T_4 - T_1)$. Substituting the expressions for q_{in} and q_{out} into the definition of thermal efficiency gives

$$\eta_{TH,Diesel} = 1 - \frac{C_v(T_4 - T_1)}{C_p(T_3 - T_2)}.$$

And since $\gamma \equiv C_p / C_v$

$$\eta_{TH,Diesel} = 1 - \frac{1}{\gamma}\cdot\frac{(T_4 - T_1)}{(T_3 - T_2)} = 1 - \frac{1}{\gamma}\cdot\left(\frac{T_1}{T_2}\right)\cdot\frac{\frac{T_4}{T_1} - 1}{\frac{T_3}{T_2} - 1}$$

The compression from state 1 to state 2 and the expansion from state 3 to state 4 is isentropic so that the relation

$$\frac{T_1}{T_2} = \left(\frac{v_2}{v_1}\right)^{\gamma-1} = \left(\frac{v_3}{v_4}\right)^{\gamma-1} = \frac{T_4}{T_3}$$

is applicable. Also, $v_2 / v_1 = r$ so that $\eta_{TH,Diesel}$ can be rewritten thusly:

$$\eta_{TH,Diesel} = 1 - \frac{1}{\gamma}\cdot\left(\frac{v_2}{v_1}\right)^{\gamma-1}\cdot\frac{\frac{T_4}{T_1} - 1}{\frac{T_3}{T_2} - 1} = 1 - \frac{1}{\gamma}\cdot\left(\frac{1}{r}\right)^{\gamma-1}\cdot\frac{\frac{T_4}{T_1} - 1}{\frac{T_3}{T_2} - 1}$$

A relation that will come in useful is the temperature-volume relationship from state 2 to state 3 derived from the ideal gas law P = RT/v. Because the heat addition takes place at constant pressure, $P_3 = P_2$ and

$$P_2 = R\frac{T_2}{v_2} = R\frac{T_3}{v_3} = P_3.$$

This rearranges to give

$$\frac{T_3}{T_2} = \frac{v_3}{v_2} \equiv r_c$$

where r_c is defined as the cut off ratio and establishes the extent of heat addition.

Examining the portion of the expression for thermal efficiency that contains the fraction of temperatures, and substituting in the value r_c where applicable gives

$$\frac{\frac{T_4}{T_1} - 1}{\frac{T_3}{T_2} - 1} = \frac{\frac{T_4}{T_1} - 1}{r_c - 1}$$

Next the term T_4/T_1 is examined:

$$\frac{T_4}{T_1} = \left(\frac{T_4}{T_3}\cdot T_3\right)\cdot\left(\frac{T_2}{T_1}\div T_2\right) = \frac{T_4}{T_3}\cdot\frac{T_2}{T_1}\cdot\frac{T_3}{T_2}$$

But

$$\frac{T_4}{T_3}=\left(\frac{v_3}{v_4}\right)^{\gamma-1}, \quad \frac{T_2}{T_1}=\left(\frac{v_1}{v_2}\right)^{\gamma-1}, \text{ and } \quad \frac{T_3}{T_2}=\frac{v_3}{v_2}$$

so that

$$\frac{T_4}{T_1}=\left(\frac{v_3}{v_4}\cdot\frac{v_1}{v_2}\right)^{\gamma-1}\cdot\frac{v_3}{v_2}$$

The volumes at state 1 and 4 are equal so that v_1 and v_4 cancel out. Also, the cut off ratio is substituted for v_3/v_2 to give

$$\frac{T_4}{T_1}=(r_c)^{\gamma-1}\cdot r_c=r_c^{\gamma}.$$

Updating the expression for $\eta_{TH,Diesel}$ gives

$$\eta_{TH,Diesel}=1-\left(\frac{1}{r}\right)^{\gamma-1}\left[\frac{r_c^{\gamma}-1}{\gamma(r_c-1)}\right].$$

Comparison of the Ideal Otto and Diesel Cycles with the Carnot Cycle

Inspection of the expressions for $\eta_{TH,Otto}$ and $\eta_{TH,Diesel}$ reveal that both increase with increasing compression ratio. They both are plotted against the compression ratio in the figure below.

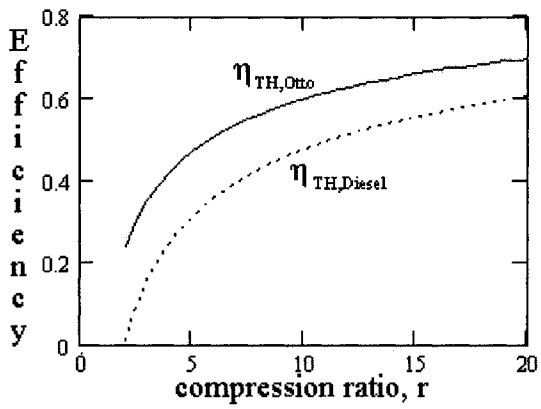

Figure A.2 – Otto and Diesel cycle efficiencies *vs* compression ratio

The Diesel cycle is always less efficient than the Otto cycle for a given compression ratio because the term $\left(r_c^{\gamma}-1\right)/\gamma\left(r_c-1\right)$ is always greater than one. Both the ideal Otto cycle and the ideal Diesel cycle are less efficient than the Carnot cycle.

For the heat addition or rejection segment of the ideal Otto cycle, constant volume heat transfer means $\Delta u = q = \bar{C}_v\left(T_{end}-T_{start}\right)$ where Δu is the change in internal energy, the bar over C_v indicates the average specific heat meaning this equation is valid even for varying specific heats, and T_{start} and T_{end} are the temperatures at the start and end of heat transfer, respectively. If T_{start} is some reference temperature, T_{ref}, then $u_2 = \bar{C}_{v,2}\left(T_2-T_{ref}\right)$

and $u_3 = \bar{C}_{v,3}\left(T_3 - T_{ref}\right)$. Further, if T_{ref} is sufficiently far from both T_3 and T_2 then $\bar{C}_{v,2} \cong \bar{C}_{v,3}$. Further still, if zero is selected as the reference temperature then ϕ can be defined as

$$\frac{u_3}{u_2} \cong \frac{\bar{C}_v\left(T_3 - 0\right)}{\bar{C}_v\left(T_2 - 0\right)} = \frac{T_3}{T_2} \equiv \phi$$

Analogously, for the ideal Diesel cycle's constant pressure heat addition

$$\frac{h_3}{h_2} \cong \frac{\bar{C}_p\left(T_3 - 0\right)}{\bar{C}_p\left(T_2 - 0\right)} = \frac{T_3}{T_2} \equiv \phi$$

ϕ represents the energy added during the heat addition segment of the cycle with $\phi = 1$ indicative of no heat addition and $\phi > 1$ for positive values of q_{in}. To facilitate the comparison of the ideal Otto and Diesel cycles, the compression ratio in the derived expressions for $\eta_{TH,Otto}$ and $\eta_{TH,Diesel}$ are converted back to temperatures. That is

$$\eta_{TH,Otto} = 1 - r^{1-\gamma} = 1 - \left(\frac{v_2}{v_1}\right)^{\gamma-1} = 1 - \left(\frac{T_1}{T_2}\right)$$

and

$$\eta_{TH,Diesel} = 1 - \left(\frac{1}{r}\right)^{\gamma-1}\left[\frac{r_c^{\gamma} - 1}{\gamma\left(r_c - 1\right)}\right] = 1 - \left(\frac{T_1}{T_2}\right)\left[\frac{r_c^{\gamma} - 1}{\gamma\left(r_c - 1\right)}\right].$$

Next, ϕ is factored out of the fraction T_1/T_2

$$\frac{T_1}{T_2} = \frac{T_1}{T_3}\cdot\frac{T_3}{T_2} = \frac{T_1}{T_3}\cdot\phi$$

so that

$$\eta_{TH,Otto} = 1 - \frac{T_1}{T_2}\cdot\phi$$

and

$$\eta_{TH,Diesel} = 1 - \frac{T_1}{T_3}\cdot\phi\cdot\left[\frac{r_c^{\gamma} - 1}{\gamma\left(r_c - 1\right)}\right]$$

Notice that T_1 is the lowest and T_3 the highest temperature in both the Otto and the Diesel cycles. Also, the derivation of $\eta_{TH,Diesel}$ revealed that $r_c = T_3/T_2$ so that $r_c = \phi$. Replacing T_1 with T_L and T_3 with T_H, as well as making the substitution of ϕ for r_c, gives

$$\eta_{TH,Otto} = 1 - \frac{T_L}{T_H} \cdot \phi$$

and

$$\eta_{TH,Diesel} = 1 - \frac{T_L}{T_H} \cdot \phi \cdot \left[\frac{\phi^{\gamma} - 1}{\gamma(\phi - 1)} \right].$$

The maximum possible thermal efficiency for any heat engine is the Carnot efficiency:

$$\eta_{TH,rev} = 1 - \frac{T_L}{T_H}.$$

Because ϕ is always greater than or equal to one, $\eta_{TH,Otto} \leq \eta_{Carnot}$ and $\eta_{TH,Diesel} \leq \eta_{Carnot}$. In fact, as the heat addition and useful work output goes to zero, the efficiencies of the ideal Otto and Diesel cycles approach the Carnot efficiency

$$\lim_{\phi \to 1} \eta_{TH,Otto} = \lim_{\phi \to 1} \eta_{TH,Diesel} = \eta_{Carnot}.$$

While it is easy to see from the expression for $\eta_{TH,Otto}$, it may not be readily apparent that, for $\eta_{TH,Diesel}$, the expression in brackets drops out as ϕ approaches unity. L'Hopital's rule is employed to evaluate the limit as $\phi \to 1$ of the quantity in brackets.

$$\lim_{\phi \to 1} \left[\frac{\phi^{\gamma} - 1}{\gamma(\phi - 1)} \right] = \lim_{\phi \to 1} \left[\frac{\frac{d}{d\phi}(\phi^{\gamma} - 1)}{\frac{d}{d\phi}(\gamma(\phi - 1))} \right] = \lim_{\phi \to 1} \left[\frac{\gamma \phi^{\gamma - 1}}{\gamma} \right] = 1$$

APPENDIX B
AMBIENT AIR DENSITY

Determining volumetric efficiency (designated η_v) requires an actual mass-flow measurement, which was provided by the Ford mass flow meter. This is divided by a theoretical mass-flow rate, which is determined by the rate that the piston sweeps a given volume multiplied by the density of ambient air. That is, $\eta_v = \dot{m}_{actual} / \dot{m}_{ideal}$. A direct measurement of the ambient air density was not available. However, the weather station at Christman Field, located 0.9 miles east of the test engine, provides data in five-minute intervals that includes temperature, pressure, and relative humidity. This information was recorded and used for each datum point.

With the relative humidity and temperature known, the humidity ratio, W, (mass of water vapor per unit mass of dry air) is determined from ASHRAE Psychrometric Chart No. 4 (1965), which gives data at 5000 feet (24.89" Hg). Fort Collins is at 4999 feet. The mean pressure for all the tests was 24.878" Hg with a standard deviation of 0.1515" Hg. Standard atmospheric pressure at sea level is 29.92" Hg at 32 °F. The ideal gas equation of state for a mixture of gases is:

$$Pv_{mix} = R_{mix}T ,$$

where R_{mix} is the sum of the constituent's mole fraction times the universal gas constant divided by the constituent's molecular weight. However, rather than calculate a mole fraction of the constituent gases for each data point, R_{mix} is found using the universal gas constant, R_u, the molecular weights of dry air and water vapor, MW_a and MW_v, and the mass of dry air and water vapor, m_a and m_v:

$$R_{mix} = \left(m_a \frac{R_u}{MW_a} + m_v \frac{R_u}{MW_v} \right) \frac{1}{m_a + m_v} .$$

The variables m_a and m_v need to be eliminated. Since, per unit mass of dry air, $m_a + m_v = 1 + W$, this substitution is made. In addition, the dry air gas constant ($R_a = R_u / MW_a$) can be factored out so that the equation of state takes the form

$$Pv_{mix} = T \cdot R_a \left(1 + \frac{MW_a}{MW_v} W \right) \frac{1}{1+W} .$$

The molecular weight of air divided by the molecular weight of water vapor is a constant equal to 1.6078. Substituting with this numerical value and dividing through by the pressure gives the specific volume of the air water vapor mixture. This is then inverted to yield the final equation for the density of moist air in terms of available data:

$$\rho_{mix} = \frac{1}{v_{mix}} = \frac{P(1+W)}{T \cdot R_a (1+1.6078W)}.$$

This equation is consistent with equations 6.9 and 6.26 in ASHRAE's 1993 Handbook of Fundamentals.

APPENDIX C
EXACT SOLUTION TO SIMPLIFIED CYLINDER HEAT TRANSFER

The problem posed and solved

In this appendix the temperature field across the combustion chamber wall is determined by finding the exact solution to the governing conduction equation with some simplifications. The simplifications are:

5) Conduction is one-dimensional.
6) The convection coefficient, h, is constant.
7) The cylinder gas temperature, T_∞, varies sinusoidally between ambient and a maximum temperature (T_{amb} and T_{max} respectively).
8) The coolant side convection boundary condition is replaced with a constant temperature boundary condition.

A small section of the combustion chamber of thickness a is considered. If the combustion-side is at $x = 0$ then the coolant-side is at $x = a$. Fixing the coolant-side temperature is equivalent to specifying a degree of cylinder insulation or fixing the net heat flux. For simplicity the gas temperature in the cylinder is set to vary sinusoidally in time between the ambient temperature and 2000 K (a typical maximum average value). Additionally, temperatures are adjusted by the ambient temperature, which is set at 300 K.

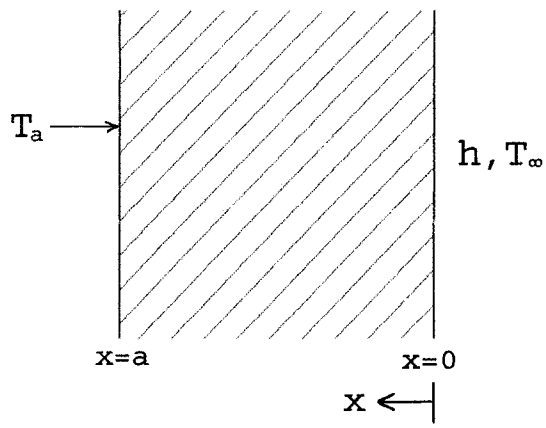

Figure A.3 – wall section.

Thus,

$$T_{max} = 2000K - 300K = 1700K$$

and

$$T_\infty = \frac{T_{max}}{2}\sin(\omega t) + \frac{T_{max}}{2}$$

The governing equation is a linear and homogeneous second order partial differential equation with non-homogeneous time variable boundary conditions:

$$\frac{1}{\alpha}\frac{\partial T}{\partial t} = \frac{\partial^2 T}{\partial x^2}$$

with boundary conditions

$$\text{at } x = 0,\ k\frac{\partial T}{\partial x} = h\left(T_{surface} - T_{\infty}\right)$$

$$\text{at } x = a,\ T(a,t) = T_a$$

where

$$T_{surface} = T_0 \sin(\omega t)$$

$$T_{\infty} = \frac{T_{max}}{2}\sin(\omega t + \phi) + \frac{T_{max}}{2}$$

The phase angle, ϕ, has been added to the cylinder gas time function because, while the cylinder surface temperature will track the adjacent cylinder gas temperature, there is no guarantee that the two will be in phase. A complete solution also requires an initial condition. However, the initial transient temperature profile is not of interest. Rather, the fully developed temperature field is sought. Since the Method of Complex Temperatures will be used to find the solution, and does not require an initial condition, none is given.

The problem is decomposed into two parts, the solutions of which are added together. The two parts are: first, the conduction equation with constant (non-time-varying) boundary conditions, and second, the conduction equation with homogeneous boundary conditions except for the time varying condition.

The first part is the steady state solution to the governing equation with boundary conditions:

$$\text{at } x = 0,\ k\frac{\partial T}{\partial x} = h\left(T_{surface} - \frac{T_{max}}{2}\right)$$

$$\text{at } x = a,\ T(a,t) = T_a$$

The variable transformation $\Theta = T - T_a$ facilitates finding the solution which is, transformed back into T,

$$T(x) = \left[\frac{\frac{T_{max}}{2} - T_a}{\frac{k}{h \cdot a} + 1}\right]\left(1 - \frac{x}{a}\right) + T_a$$

The second part has boundary conditions

$$\text{at } x = 0,\ k\frac{\partial T(0,t)}{\partial x} = h\left(T_0 \sin(\omega t) - \frac{T_{max}}{2}\sin(\omega t + \phi)\right)$$
$$\text{at } x = a,\ T(a,t) = 0$$

This problem is further decomposed by decoupling the convection condition from the surface temperature. The problem is then solved with an unknown time varying surface temperature which is later found by satisfying the convection equation at the surface.

The mathematical purist may raise objections that the above boundary conditions do not exactly describe the physical problem. To wit, the penetration of temporal variations extend, albeit in very small and exponentially decaying magnitude, beyond even very large values of $x = a$. Holding T_a constant in the solution of the first (time invariant) part of the decomposed problem poses no contradictions as long as the time varying nature is addressed in the solution to the second part. Here in the second part the boundary condition at $x = a$ is now altered so that $T(a,t) = T_a + \delta(t)$, where $\delta(t)$ is a small temporal variation. It is claimed that $\lim_{a\to\infty} \delta(t) = 0$ so that the boundary conditions for the second part of the problem are

$$\text{at } x = 0,\ T(0,t) = T_0 \sin(\omega t)$$
$$\text{at } x, a \to \infty,\ T(\infty,t) = 0$$

along with

$$k\frac{\partial T(0,t)}{\partial x} = h\left(T_0 \sin(\omega t) - \frac{T_{max}}{2}\sin(\omega t + \phi)\right)$$

which will be used to determine T_0 (a constant) after finding $T(x,t)$.

The Method of Complex temperatures has five steps.

1) Construct the model of the problem with unknown solution $T_R(x,t)$.
2) Construct the model of an identical problem with the time varying boundary condition out of phase by $\pi/2$ radians with unknown solution $T_I(x,t)$.
3) Construct the model of the complex temperature problem with unknown solution $T(x,t) = T_R + iT_I$.
4) Assume $T(x,t) = X(x)e^{\pm i(\omega t+\phi)}$ and solve.
5) Render the solution into the form $T(x,t) = T_R + iT_I$ and take $T_R(x,t)$ as the solution.

Step 1:

$$\frac{1}{\alpha}\frac{\partial T_R}{\partial t} = \frac{\partial^2 T_R}{\partial x^2}$$
$$T_R(0,t) = T_0 \sin(\omega t)$$
$$T_R(\infty,t) = 0$$

Step 2:

$$\frac{1}{\alpha}\frac{\partial T_I}{\partial t} = \frac{\partial^2 T_I}{\partial x^2}$$
$$T_I(0,t) = T_0 \cos(\omega t)$$
$$T_I(\infty,t) = 0$$

Step 3:

$$\frac{1}{\alpha}\frac{\partial (T_R + iT_I)}{\partial t} = \frac{\partial^2 (T_R + iT_I)}{\partial x^2}$$
$$T(\infty,t) = T_R(\infty,t) + iT_I(\infty,t) = 0$$
$$T(0,t) = T_R(0,t) + iT_I(0,t) = T_0\left[\sin(\omega t) + i\cos(\omega t)\right]$$
$$= T_0\left[-\cos(\omega t + \pi/2) + i\sin(\omega t + \pi/2)\right]$$
$$= -T_0\left[\cos(\omega t + \pi/2) - i\sin(\omega t + \pi/2)\right]$$
$$= -T_0 e^{-i(\omega t + \pi/2)}$$

But $T \equiv T_R + iT_I$ so

$$\frac{1}{\alpha}\frac{\partial T}{\partial t} = \frac{\partial^2 T}{\partial x^2}$$

With boundary conditions:

$$T(\infty,t) = 0$$
$$T(0,t) = T_0 e^{-i(\omega t + \phi)}$$

Substituting $X(x)e^{\pm i(\omega t + \phi)}$ for $T(x,t)$ and noting that $\frac{\partial T}{\partial t} = -i\omega e^{-i(\omega t + \pi/2)}X$ and $\frac{\partial^2 T}{\partial x^2} = \frac{d^2 X}{dx^2}e^{-i(\omega t + \pi/2)}$ gives

$$\frac{-i\omega}{\alpha}X = \frac{dX^2}{dx^2}$$

With boundary conditions:

$$X(0) = -T_0$$
$$X(\infty) = 0$$

Which has the solution

$$X(x) = Ae^{x\sqrt{-i\omega/\alpha}} + Be^{-x\sqrt{-i\omega/\alpha}}$$

Noting that $-i^{0.5} = 1/\sqrt{2} - i/\sqrt{2}$, $e^{-i\theta} = \cos(\theta) - i\sin(\theta)$, $e^{i\theta} = \cos(\theta) + i\sin(\theta)$, and defining $\xi(x) = x\sqrt{\omega/2\alpha}$:

$$X(x) = Ae^{\xi(x)}\left[\cos(\xi(x)) - i\sin(\xi(x))\right] + Be^{-\xi(x)}\left[\cos(\xi(x)) + i\sin(\xi(x))\right]$$

Applying $X(\infty) = 0$ shows that $A = 0$. Subsequent application of $X(0) = -T_0$ yields $B = -T_0$ so that

$$X(x) = -T_0 e^{-\xi(x)}\left[\cos(\xi(x)) + i\sin(\xi(x))\right]$$
$$X(x) = -T_0 e^{-\xi(x)} e^{i\xi(x)}$$

And since $T(x,t) = X(x)e^{\pm i(\omega t + \phi)}$

$$\begin{aligned} T(x,t) &= -T_0 e^{-\xi(x)} e^{i\xi(x)} e^{-i(\omega t + \pi/2)} \\ &= -T_0 e^{-\xi(x)} e^{-i(\omega t - \xi(x) + \pi/2)} \\ &= -T_0 e^{-\xi(x)}\left[\cos(\omega t - \xi(x) + \pi/2) - i\sin(\omega t - \xi(x) + \pi/2)\right] \\ &= T_0 e^{-\xi(x)}\left[\sin(\omega t - \xi(x)) - i\cos(\omega t - \xi(x))\right] \end{aligned}$$

which contains both a real and imaginary part. Recalling that $T \equiv T_R + iT_I$, that T_R is the solution of interest, and substituting $x\sqrt{\omega/2\alpha}$ back in for $\xi(x)$ gives

$$T_R(x,t) = T_0 e^{-x\sqrt{\omega/2\alpha}} \sin\left(\omega t - x\sqrt{\omega/2\alpha}\right)$$

and

$$T_R(x=0,t) = T_0 \sin(\omega t)$$

All that remains is to find T_0 by applying the convection boundary condition and add the solution of part two to that of part one.

Differentiating with respect to x gives

$$\frac{\partial T_R(x,t)}{\partial x} = -T_0 \cdot \sqrt{\frac{\omega}{2\alpha}} \cdot e^{-x\sqrt{\omega/2\alpha}}\left[\sin\left(\omega t - x\sqrt{\omega/2\alpha}\right) + \cos\left(\omega t - x\sqrt{\omega/2\alpha}\right)\right]$$

and

$$\frac{\partial T_R(x=0,t)}{\partial x} = -T_0 \cdot \sqrt{\frac{\omega}{2\alpha}} \cdot \left[\sin(\omega t) + \cos(\omega t)\right].$$

Applying the convection boundary condition,

$$k\frac{\partial T_R(x=0,t)}{\partial x} = h\left[T_R(x=0,t) - T_\infty(t)\right]$$

$$-T_0 \cdot k\sqrt{\frac{\omega}{2\alpha}} \cdot \left(\sin(\omega t) + \cos(\omega t)\right) = h\left(T_0 \sin(\omega t) - \frac{T_{max}}{2}\sin(\omega t + \phi)\right).$$

Particularly convenient times for evaluating the above equation are at $t = 0$ and at $t = \pi/2\omega$. These values of t lead to two expressions for T_0:

$$T_0 = \frac{h\frac{T_{max}}{2}\cos(\phi)}{k\sqrt{\frac{\omega}{2\alpha}} + h}$$

and

$$T_0 = \frac{h\frac{T_{max}}{2}\sin(\phi)}{k\sqrt{\frac{\omega}{2\alpha}}}.$$

This allows ϕ to be determined:

$$\phi = \cot^{-1}\left[1 + \frac{h}{k}\sqrt{\frac{2\alpha}{\omega}}\right]$$

or

$$\phi = \arctan\left[1\Big/\left(1 + \frac{h}{k}\sqrt{\frac{2\alpha}{\omega}}\right)\right].$$

Though ϕ was found with two discrete values of t, it satisfies the convection boundary condition equation

$$-T_0 \cdot k\sqrt{\frac{\omega}{2\alpha}} \cdot \left(\sin(\omega t) + \cos(\omega t)\right) = h\left(T_0 \sin(\omega t) - \frac{T_{max}}{2}\sin(\omega t + \phi)\right)$$

for all t . . . amazing, but true.

Lastly, adding the solutions from the first part and the second part gives the time varying temperature at any depth x in the section of combustion chamber wall:

$$T(x,t)=\left[\frac{\frac{T_{max}}{2}-T_a}{\frac{k}{h\cdot a}+1}\right]\left(1-\frac{x}{a}\right)+T_a+T_0e^{-x\sqrt{\omega/2\alpha}}\sin\left(\omega t-x\sqrt{\omega/2\alpha}\right)$$

Where ϕ and T_0 are found using the expressions just derived.

The Intra-cycle heat transfer

The surface heat flux is the sum of the steady state solution and the time varying solution:

$$q''_{total}=-k\frac{\partial T(x=0,t)}{\partial x}=\frac{-k}{a}\left[\frac{\frac{T_{max}}{2}-T_a}{\frac{k}{h\cdot a}+1}\right]+T_0\cdot k\sqrt{\frac{\omega}{2\alpha}}\cdot\left(\sin(\omega t)+\cos(\omega t)\right)$$

To simplify a step further the identity $\cos(\omega t)+\sin(\omega t)=\sqrt{2}\sin(\omega t+\pi/4)$ is employed (proof follows). This gives

$$q''_{total}=\frac{-k}{a}\left[\frac{\frac{T_{max}}{2}-T_a}{\frac{k}{h\cdot a}+1}\right]+T_0\cdot k\sqrt{\frac{\omega}{\alpha}}\cdot\sin\left(\omega t+\frac{\pi}{4}\right).$$

Lastly, let $\tau=\omega t+\pi/4$ so that

$$q''_{total}=\frac{-k}{a}\left[\frac{\frac{T_{max}}{2}-T_a}{\frac{k}{h\cdot a}+1}\right]+T_0\cdot k\sqrt{\frac{\omega}{\alpha}}\cdot\sin(\tau).$$

Of interest is the quantity of heat transferred from the gas during the high temperature portion of the cycle and the quantity of heat transferred back to the gas during the low temperature portion of the cycle. What is sought is the value τ_1 for which

$$\int_{\tau=0}^{\tau_1}T_0\cdot k\sqrt{\frac{\omega}{\alpha}}\cdot\sin(\tau)\frac{d\tau}{\omega}=-\int_{\tau=\tau_1}^{2\pi}T_0\cdot k\sqrt{\frac{\omega}{\alpha}}\cdot\sin(\tau)\frac{d\tau}{\omega}$$

so that

$$q_1=\int_0^{\tau_1}\left[\frac{-k}{a}\left[\frac{\frac{T_{max}}{2}-T_a}{\frac{k}{h\cdot a}+1}\right]+T_0\cdot k\sqrt{\frac{\omega}{\alpha}}\cdot\sin(\tau)\right]\frac{d\tau}{\omega}$$

$$q_2 = \int_{\tau_1}^{2\pi} \left[\frac{-k}{a} \left[\frac{\frac{T_{max} - T_a}{2}}{\frac{k}{h \cdot a} + 1} \right] + T_0 \cdot k \sqrt{\frac{\omega}{\alpha}} \cdot \sin(\tau) \right] \frac{d\tau}{\omega}$$

may be evaluated (note that $dt = d\tau/\omega$). Clearly $\tau_1 = \pi$. Evaluating the integrals gives:

$$q_1 = \left(\frac{2}{\omega}\right) T_0 \cdot k \sqrt{\frac{\omega}{\alpha}} - \left(\frac{\pi}{\omega}\right) \frac{k}{a} \left[\frac{\frac{T_{max} - T_a}{2}}{\frac{k}{h \cdot a} + 1} \right]$$

and

$$q_2 = -\left(\frac{2}{\omega}\right) T_0 \cdot k \sqrt{\frac{\omega}{\alpha}} - \left(\frac{\pi}{\omega}\right) \frac{k}{a} \left[\frac{\frac{T_{max} - T_a}{2}}{\frac{k}{h \cdot a} + 1} \right].$$

where q_1 represents the heat transfer to the cool, precombustion gases and q_2 represents the heat transfer to the hot, postcombustion gases. Note that in the above solution the entire positive portion of the time variable part of heat transfer is ascribed to heating the intake charge while the negative portion is ascribed to cooling the postcombustion gases.

Proof of a trigonometric identity

To show that

$$\cos(\theta) + \sin(\theta) = \sqrt{2} \cos\left(\theta - \frac{\pi}{4}\right)$$
$$= \sqrt{2} \sin\left(\theta + \frac{\pi}{4}\right)$$

the Euler identity, $e^{ix} = \cos(x) + i\sin(x)$, is chosen as the starting point. Let $x = \alpha + \beta$ so that

$$\cos(\alpha+\beta) + i\sin(\alpha+\beta) = e^{i(\alpha+\beta)}$$
$$\cos(\alpha+\beta) + i\sin(\alpha+\beta) = e^{i\alpha} e^{i\beta}$$
$$\cos(\alpha+\beta) + i\sin(\alpha+\beta) = [\cos(\alpha) + i\sin(\alpha)] \cdot [\cos(\beta) + i\sin(\beta)]$$
$$\cos(\alpha+\beta) + i\sin(\alpha+\beta) = [\cos(\alpha)\sin(\beta) - \sin(\alpha)\sin(\beta)] + i[\sin(\alpha)\cos(\beta) - \cos(\alpha)\sin(\beta)]$$

Equating the real and imaginary parts gives, respectively,

$$\cos(\alpha+\beta)=\cos(\alpha)\cos(\beta)-\sin(\alpha)\sin(\beta)$$

and

$$\sin(\alpha+\beta)=\cos(\alpha)\sin(\beta)+\sin(\alpha)\cos(\beta)$$

For the real part, making the substitutions $\theta=\alpha$, $-\pi/4=\beta$, and recognizing that $\cos\left(\frac{-\pi}{4}\right)=-\sin\left(\frac{-\pi}{4}\right)=\frac{1}{\sqrt{2}}$ gives:

$$\cos\left(\theta-\frac{\pi}{4}\right)=\frac{1}{\sqrt{2}}\cos(\theta)+\frac{1}{\sqrt{2}}\sin(\theta)$$

$$\sqrt{2}\cos\left(\theta-\frac{\pi}{4}\right)=\cos(\theta)+\sin(\theta)$$

Similarly, for the imaginary part with the substitutions $\theta=\alpha$, $\pi/4=\beta$, and $\cos\left(\frac{\pi}{4}\right)=\sin\left(\frac{\pi}{4}\right)=\frac{1}{\sqrt{2}}$ gives

$$\sin\left(\theta+\frac{\pi}{4}\right)=\frac{1}{\sqrt{2}}\cos(\theta)+\frac{1}{\sqrt{2}}\sin(\theta)$$

$$\sqrt{2}\sin\left(\theta+\frac{\pi}{4}\right)=\cos(\theta)+\sin(\theta)$$

which are the two identities sought.

Heat Loss

The heat loss has components from the steady state and the time varying parts of the solution: $q=q_t+q_{ss}$. The half cycle components are

$$q_{ss}=\left(\frac{\pi}{\omega}\right)\frac{k}{a}\left[\frac{\frac{T_{max}}{2}-T_a}{\frac{k}{h\cdot a}+1}\right]$$

and

$$q_t=\pm\frac{2k}{\omega}T_0\sqrt{\frac{\omega}{\alpha}}$$

T_0 was found:

$$T_0 = \frac{h\frac{T_{max}}{2}\sin(\phi)}{k\sqrt{\frac{\omega}{2\alpha}}}$$

so the heat transferred according to the time varying part is

$$q_t = \sqrt{2}\frac{h}{\omega}T_{\max}\sin(\phi)$$

where

$$\phi = \arctan\left[1\Big/\left(1+\frac{h}{k}\sqrt{\frac{2\alpha}{\omega}}\right)\right].$$

APPENDIX D
FOURIER SERIES REPRESENTATION OF HEAT RELEASE PROFILE

The representation of some arbitrary but periodic function is facilitated by the trigonometric series first presented in Joseph Fourier's 1807 memoir, *On the propagation of heat in solid bodies* [John Herivel, 1972]. Most piecewise smooth functions, $f(x)$, can be represented on the interval –L to L by the Fourier series [Richard Haberman, 1987]:

$$f(x) \sim a_0 + \sum_{n=1}^{\infty} a_n \cos\left(\frac{n\pi x}{L}\right) + \sum_{n=1}^{\infty} b_n \sin\left(\frac{n\pi x}{L}\right)$$

where

$$a_0 = \frac{1}{2L}\int_{-L}^{L} f(x)dx$$

$$a_n = \frac{1}{L}\int_{-L}^{L} f(x)\cos\left(\frac{n\pi x}{L}\right)dx$$

$$b_n = \frac{1}{L}\int_{-L}^{L} f(x)\sin\left(\frac{n\pi x}{L}\right)dx$$

While $f(x)$ can be most anything, for the purpose of this work approximating heat release profiles or temperature profiles in a diesel engine is accomplished by fitting together sections of linear functions. What follows is the derivation of a generalized linear pulse of duration $\xi_2 - \xi_1$.

Consider the line shown below with ends ζ_1 at $x = \xi_1$, and ζ_2 at $x = \xi_2$ contained somewhere within the interval –L to L.

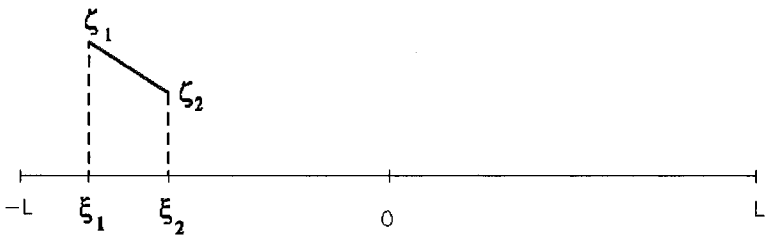

Figure A.4 – linear pulse on interval of periodicity

The line, $y = mx + b$, has slope

$$m = \frac{\zeta_2 - \zeta_1}{\xi_2 - \xi_1}$$

And y intercept

$$b = \zeta_2 - m\xi_2$$

which should not be confused with the Fourier coefficient b_n defined below.

Solving for the Fourier coefficients,

$$a_0 = \frac{1}{2L}\int_{\xi_1}^{\xi_2}(mx+b)\,dx = \frac{1}{2L}\left[\frac{m}{2}x^2 + bx\right]_{\xi_1}^{\xi_2}$$

which, when the limits of integration are applied, becomes

$$a_0 = \frac{1}{2L}\left[\frac{m}{2}\xi_2^2 - \frac{m}{2}\xi_1^2 + b\xi_2 - b\xi_1\right].$$

The coefficient a_n is

$$a_n = \frac{1}{L}\int_{\xi}^{\xi_2}(mx+b)\cos(n\pi x/L)dx = \frac{m}{L}\int_{\xi_1}^{\xi_2} x\cos(n\pi x/L)\,dx + \frac{b}{L}\int_{\xi_1}^{\xi_2}\cos(n\pi x/L)\,dx$$

$$a_n = \frac{m}{L}\left[\frac{L}{n\pi}x\sin(n\pi x/L) + \frac{L^2}{n^2\pi^2}\cos(n\pi x/L)\right]_{\xi_1}^{\xi_2} + \frac{b}{L}\left[\frac{L}{n\pi}\sin(n\pi x/L)\right]_{\xi_1}^{\xi_2}$$

which becomes

$$a_n = \frac{m}{n\pi}\left[\xi_2\sin(n\pi\xi_2/L) - \xi_1\sin(n\pi\xi_1/L) + \frac{L}{n\pi}\cos(n\pi\xi_2/L) - \frac{L}{n\pi}\cos(n\pi\xi_2/L)\right]$$
$$+\frac{b}{n\pi}\left[\sin(n\pi\xi_2/L) - \sin(n\pi\xi_1/L)\right]$$

Similarly,

$$b_n = \frac{mL}{n^2\pi^2}\left[\sin(n\pi\xi_2/L) - \sin(n\pi\xi_1/L) - \frac{n\pi\xi_2}{L}\cos(n\pi\xi_2/L) + \frac{n\pi\xi_1}{L}\cos(n\pi\xi_1/L)\right]$$
$$-\frac{b}{n\pi}\left[\cos(n\pi\xi_2/L) - \cos(n\pi\xi_1/L)\right]$$

Applying the above series to the heat release curve presented in chapter 5 requires six ramp pulses added together. The heat release curve predicted by Kiva and used for Wave input for the Lister-Petter engine with superalloy components at 3000 rpm (figure 5.5) is

reprinted below as figure A.5 for quick reference. Following the Kiva-predicted heat release profile are figures A.6 and A.7 showing the Fourier series representation of the heat release curve with 600 and 3240 terms, respectively.

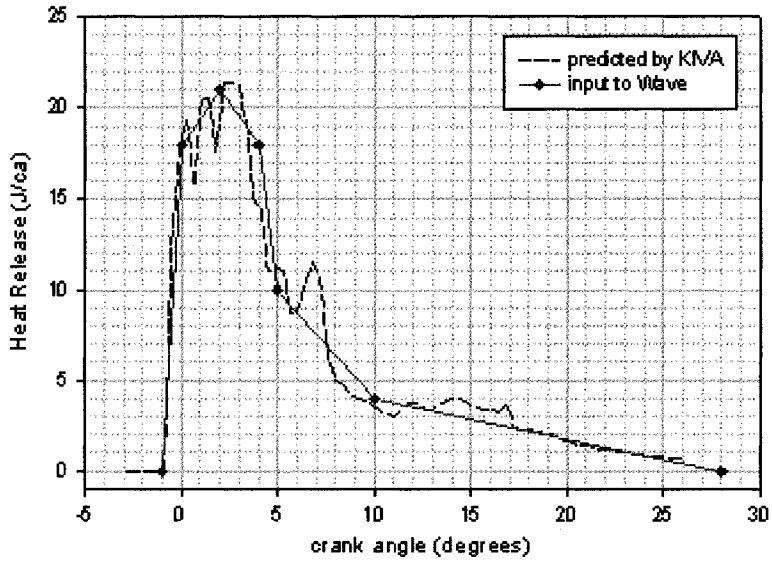

Figure A.5 – reprint of figure 5.5, heat release profile in superalloy engine at 3000 rpm.

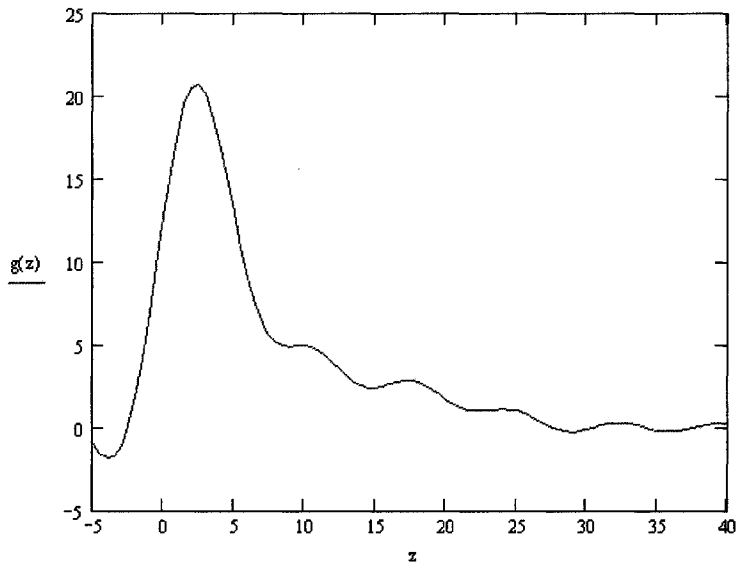

Figure A.6 – Fourier series representation of heat release profile with 6x100 terms

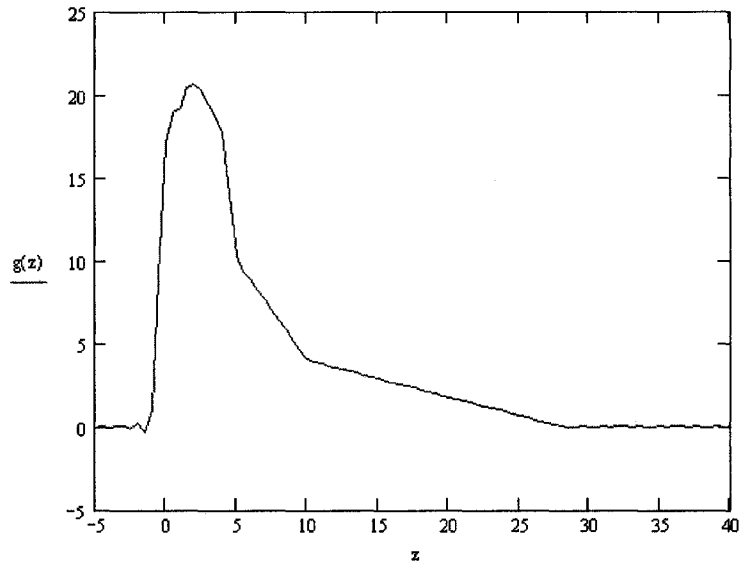

Figure A.7 – Fourier series representation of heat release profile with 6x540 terms.

In general, a Fourier series will produce a reasonable facsimile of a function with significantly fewer terms. However, in this particular application the interval of periodicity is 720 degrees of crank angle and some ramp sections have a pulse-width of only one or two crank angles. The number of terms required for fidelity in the Fourier series is commensurate with the resolution required to clearly describe the function. In other words, if the ratio of pulse width to interval is 1/720 then a Fourier series will require on the order of 720 terms. In the example at hand, 540 terms were used in each of the six ramp pulses comprising the heat release profile of figure A.7 for a total of 3,240 terms.

APPENDIX E
POLYTROPIC PROCESSES – A THERMODYNAMICS REVIEW

The conservation of energy equation for a closed system with negligible kinetic and potential energy is

$$q - w_{boundary} = \Delta u \tag{4}$$

where the work done by or to the piston is

$$w_{boundary} = \int P dv .$$

Allowing for heat transfer during the expansion or compression stroke means the process is polytropic ($Pv^n = C$ or $P = Cv^{-n}$) so

$$w_{boundary} = C\int_1^2 v^{-n} dv = \left[\frac{C}{1-n} v^{1-n}\right]_1^2 = \left[\frac{Pv}{1-n}\right]_1^2$$

and evaluating the limits

$$w_{boundary} = \frac{1}{n-1}\left(P_2 v_2 - P_1 v_1\right)$$

When the substitution $RT = Pv$ is made the resulting equation is

$$w_{boundary} = \frac{R}{1-n}\left(T_2 - T_1\right) \tag{5}$$

If $n = C_p/C_v$ the process is adiabatic, if $n = 1$ the process is isothermal. With the simplification of constant specific heats the change in internal energy is

$$\Delta u = C_v\left(T_2 - T_1\right) \tag{6}$$

The P-v diagram below shows the path for isentropic and polytropic compression from state 1 to state 2. Ideal gas behavior along with the constant specific heat simplification means that

$$\Delta u_{polytropic} + q = \Delta u_{isentropic} \tag{7}$$

Last, for an ideal gas

$$ds = C_v \frac{dT}{T} + R\frac{dv}{v}$$

so that, for an isentropic process and constant specific heat

$$\ln\left(\frac{T_2}{T_1}\right) = \frac{-R}{C_v}\ln\left(\frac{v_2}{v_1}\right)$$

which may be rewritten

$$\frac{T_{2,isentropic}}{T_1} = \left(\frac{v_1}{v_2}\right)^{\gamma-1} \tag{8}$$

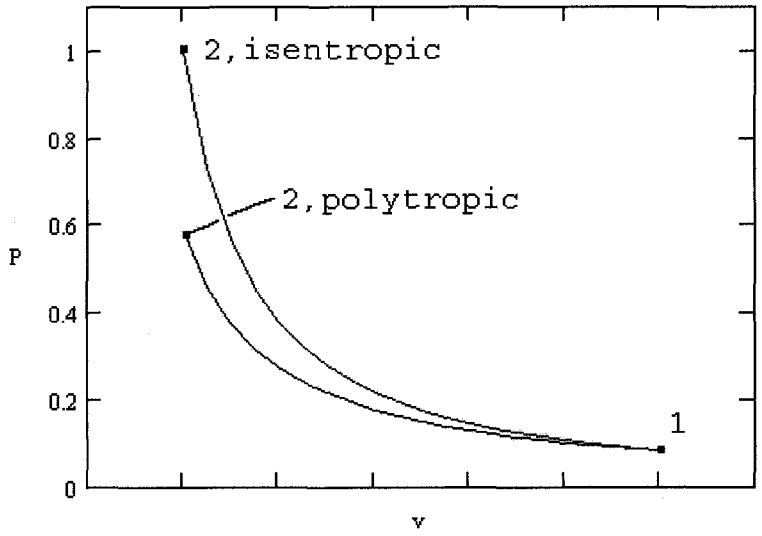

Figure A.8 Polytropic and Isentropic Compression

Equations 1 through 5 comprise the set necessary to write the polytropic boundary work in terms of v_1, v_2, T_1 and q. Rearranging equation 5 to isolate $T_{2,isentropic}$ yields

$$T_{2,isentropic} = T_1\left(\frac{v_1}{v_2}\right)^{\gamma-1}$$

substituting equation 3 into equation 4 and rearranging gives

$$T_{2,poly} = T_1\left(\frac{v_1}{v_2}\right)^{\gamma-1} - \frac{q}{C_v}$$

Inserting the expression for boundary work (eq. 2) and the change in internal energy (eq.3) into the conservation of energy equation (eq. 1) gives

$$q-\frac{R}{1-n}\left(T_{2,poly}-T_1\right)=C_v\left(T_{2,poly}-T_1\right)$$

which rearranges to

$$\frac{q}{\left(T_{2,poly}-T_1\right)}=C_v+\frac{R}{1-n}$$

and finally, to

$$n=1-\frac{R}{\frac{q}{\left(T_{2,poly}-T_1\right)}-C_v}$$

Substituting the expression for n into the expression for $w_{bndry,poly}$ (eq. 2) yields

$$w_{bndry,poly}=\left(\frac{q}{T_{2,poly}-T_1}-C_v\right)\cdot\left(T_{2,poly}-T_1\right)$$

and substituting in the expression for $T_{2,poly}$ gives

$$w_{bndry,poly}=\left(\frac{q}{T_1\left(\frac{v_1}{v_2}\right)^{\gamma-1}-\frac{q}{C_v}-T_1}-C_v\right)\cdot\left(T_1\left(\frac{v_1}{v_2}\right)^{\gamma-1}-\frac{q}{C_v}-T_1\right).$$